Nanostructure and ion dynamics of novel ionenes via scattering and simulation

by

Eric Matthew Schibli

M.Sc., Simon Fraser University, 2016
B.Sc., University of Northern British Columbia, 2013

Thesis Submitted in Partial Fulfillment of the
Requirements for the Degree of
Doctor of Philosophy

in the
Department of Physics
Faculty of Science

SIMON FRASER UNIVERSITY
Spring 2021

Declaration of Committee

Name:	**Eric Matthew Schibli**
Degree:	**Doctor of Philosophy**
Thesis title:	**Nanostructure and ion dynamics of novel ionenes via scattering and simulation**
Committee:	**Chair:** Malcolm Kennett Associate Professor, Physics

Barbara J. Frisken
Supervisor
Professor, Physics

Steven Holdcroft
Committee Member
Professor, Chemistry

Karen Kavanagh
Committee Member
Professor, Physics

David Sivak
Examiner
Associate Professor, Physics

Dvora Perahia
External Examiner
Professor, Chemistry
Clemson University

Abstract

The creation of advanced solid polymer electrolytes is of critical importance for the development of many technologies, especially fuel cells and hydrogen electrolyzers. While hydrogen fuel cells are a top candidate to replace the internal combustion engine in many applications, they are currently too expensive for mainstream adoption due to the use of perfluorinated sulfonic acid-based (PFSA) polymer electrolytes, which are expensive, and require expensive platinum catalysts and titanium cell components. Utilizing hydrocarbon alkaline membranes can dramatically reduce costs, but such membranes that achieve chemical stability and ion conductivity comparable to PFSAs have proven elusive.

It has been shown that polyatomic cations integrated into polymer backbones, when sterically protected, can provide high ion conductivity and excellent chemical stability. As these materials consist of cations directly integrated into rigid polymer backbones, the phase separation observed in high-performing polymers such as PFSA is not possible, and it is not clear how high conductivity is achieved. This thesis provides a comprehensive investigation into the nanostructure of such materials via a combination of X-ray scattering at controlled humidity and atomistic molecular dynamics simulations, which reveal a sponge-like nanostructure, near-complete percolation at low degrees of hydration, and no evidence of long-range phase separation. A preliminary analysis of the ion dynamics reveals an unexpectedly strong relationship between accessible volume and ion mobility, suggesting that ion mobility is almost completely defined by the accessible volume in these materials.

Keywords: Thesis; X-ray Scattering; Molecular Dynamics; Ionenes; Physical Chemistry

Dedication

This thesis is dedicated to everyone doing their best to keep us kind, calm, and safe during these difficult times.

Acknowledgements

The work described here was made possible by my advisors Dr. Barbara Frisken, Dr. Karen Kavanagh, and Dr. Steven Holdcroft, who offered brilliant feedback and displayed endless patience and understanding. I also must acknowledge and thank my excellent collaborators and coworkers in the Holdcroft Group, including Dr. Thomas Skalski, Dr. Simon Cassegrain, Dr. Philip Overton, Nicolas Peressin, and my collaborators in the Frisken Group, including Jake Stewart, Aidan Wright, Colton Lohn, and Matthew Garayt. I especially need to acknowledge Dr. Jiantao Fan, Dr. Andrew Wright, Wei Li, and Binyu Chen, who synthesized and prepared materials analyzed in this work. X-ray scattering experiments were supported by Dr. Philip Kubik and Dennis Hsaio at 4D Labs, and especially by Dr. Karsten Joensen at Xenocs, who went above and beyond to keep the instrument running smoothly. Computational work was supported by helpful feedback and advice provided by Dr. Michael Eikerling at SFU and Dr. Amalie Frischknecht at Sandia National Laboratories. Finally, and most importantly, this work was made possible by my parents, my siblings, and by Naomi Guo, who helped keep me sane along the way.

X-ray scattering in this work made use of the 4D LABS shared facilities supported by the Canada Foundation for Innovation, British Columbia Knowledge Development Fund, Western Economic Diversification Canada, and Simon Fraser University. Computational work was enabled in part by support provided by WestGrid and Compute Canada Calcul Canada.

Hofstadter's Law: It always takes longer than you expect, even when you take into account Hofstadter's Law.

– Douglas Hofstadter

Table of Contents

List of Tables

List of Figures

Chapter 1

Introduction

Solid polymer electrolytes are of high technological interest, with applications in water purification [1, 2], dialysis [3], and energy conversion [4, 5]. However, the creation of advanced polymer electrolytes is of particular importance to the development of fuel cells and hydrogen electrolyzers; while hydrogen fuel cells are a top candidate to replace the internal combustion engine in many applications where energy densities and specific energies are priorities [6, 7, 8], they are currently too expensive for mainstream use [9]. Much of the cost is attributable to the use of perfluorinated sulfonic acid-based (PFSA) polymer electrolytes such as Nafion®, Aquivion®, and GORE-SELECT®. These materials combine excellent chemical and mechanical stability with strong ion conductivity, but are expensive and very hostile to metal components due to their extreme acidity, which necessitates the use of platinum catalysts and titanium bipolar plates [10]. These components, combined with the membranes themselves, account for over 75% of the cost of a commercially-available PFSA-based fuel cell [9]. The use of perfluorinated membranes also presents significant human health and environmental issues due to the ability of perfluorinated compounds to bioaccumulate [11].

The fuel cell is an electrochemical energy converter conceptually similar to a non-rechargeable battery; fuel and oxygen are supplied to opposite electrodes, and ions in the electrolyte are consumed at one electrode and replenished at the other, causing ions to migrate between the electrodes and establish an electric potential difference that can be utilized for useful work. The hydrogen electrolyzer is a similar device that operates in reverse; an external electric potential is applied to force the migration of ions across the electrolyte and synthesize hydrogen and oxygen gas from water. Fuel cells have some significant advantages over batteries, primarily outstanding energy density, enabled by the use of extremely light hydrogen fuel and oxygen from ambient air, and decoupled energy storage and energy conversion systems, which allows the use of inexpensive external fuel tanks. This makes fuel cells particularly attractive for applications where great amounts of energy storage is necessary, such as long-range cargo transportation or grid energy storage.

The most common fuel cells use humidified solid polymer electrolytes operated at slightly elevated temperatures (60-80° C), and are referred to here as PEMFCs.[1] While other designs exist, they have specific operational requirements such as very high operating temperatures, highly pure oxygen supplies, and/or supplies of carbon dioxide, limiting their potential applications. A cation-exchange membrane fuel cell (CEMFC), in which the electrolyte is a solid, hydrated acidic polymer, and an anion-exchange membrane fuel cell (AEMFC), in which the electrolyte is a solid, hydrated alkaline polymer, are shown in Fig. 1.1.

The development of electrolyte membranes for PEMFCs is an area of very active research. The membrane must meet stringent requirements: it must maintain high ion conductivity while remaining impermeable to neutral gases at a wide range of humidities and temperatures, and it must be mechanically and chemically stable at elevated temperature and extreme pH conditions. Mechanical stability generally requires that the polymer not undergo dramatic dimensional swelling at high humidity or when exposed to liquid water, as large changes in membrane volume will cause the membrane to crack. In addition, for feasibility in commercial fuel cell stacks, membranes must be synthesizable at scale and processable – that is, soluble in low-boiling-point solvents. This is particularly challenging for AEMFCs and AEM electrolyzers, as they operate in very high pH environments, which are especially hostile to the organic material in general and organic cations in particular.

While nearly all hydrogen is currently produced via steam reformation of methane rather than electrolysis, the lifecycle carbon emissions of a fuel cell passenger vehicle (FCEV) are currently competitive with those of a battery vehicle (BEV) of similar size when utilizing the average US mix of electrical energy sources [13]. Where nearly all electricity is produced via renewable methods, such as in British Columbia, an FCEV vehicle utilizing hydrogen produced via electrolysis would have slightly lower lifetime emissions than a similar BEV due to the carbon intensity of battery production [13]. The incumbent form of hydrogen electrolyzer utilizes liquid alkaline electrolytes of concentrated KOH solution. These electrolyzers have limited current density due to the inability to utilize high pressures and the extreme sensitivity of the electrolyte to atmospheric carbon, which can dissolve into the electrolyte and "poison" the cathode with K_2CO_3 salt crystals [4]. The use of a solid polymer electrolyte allows much greater current densities, gas purity, and cathode pressures [4], but is uncommon due to the same cost issues facing fuel cells.

The use of anion-exchange membranes in fuel cells and hydrogen electrolyzers may offer significant cost savings by allowing the use of nonfluorinated hydrocarbon electrolytes, reduced- or zero-platinum catalysts, and non-titanium metal components.[2] However, hydroxide-exchange membranes matching the combination of performance and stabil-

[1]PEMFC often refers to "proton-exchange membrane fuel cell" specifically, but it is used more generally here as no other common acronym exists referring to both types of solid polymer electrolyte fuel cells.

[2]The use of nonfluorinated proton-exchange membranes may also offer some of these cost savings.

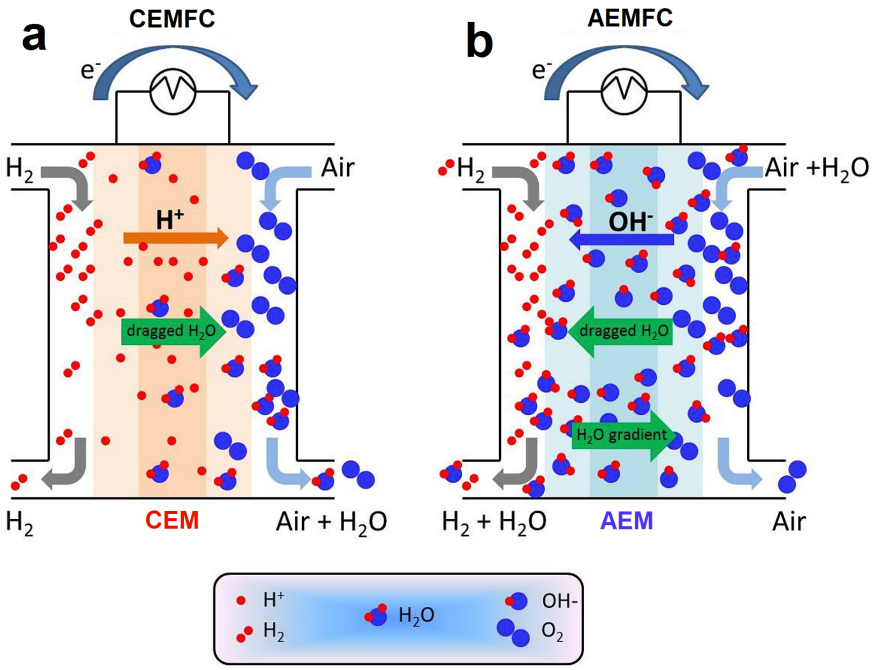

Figure 1.1: Schematics of (a) a cation-exchange membrane fuel cell (CEMFC), and (b) an anion-exchange membrane fuel cell (AEMFC). Reprinted from Reference [12] under the Creative Commons 4.0 license.

ity offered by the incumbent PFSA-based membranes have proved challenging to produce, primarily due to the instability of most cationic groups in strongly alkaline conditions and the lower mobility of hydroxide ions relative to protons in solution. Until recently, research interest may have been dampened by potentially exaggerated concern about the performance impact of dissolved hydroxide ions reacting with atmospheric carbon and forming bulky carbonate or bicarbonate ions.[3] While enormous progress has been made in the last five years, chemical stability remains the most significant challenge [12]. Nearly all reported AEMFC tests show stable performance for fewer than 300 hours [12].

Most established PEMs are *ionomers*: polymers with ionic functionalized[4] pendants – usually SO_3^- groups in CEMs and $N(CH_3)_3^+$ groups in AEMs. This pendant structure prevents the elimination of the functional groups from causing chain cleavage, which lowers the degree of polymerization and degrades the membrane's mechanical strength. Furthermore, grafting the acidic or basic units to the polymer backbones via flexible pendants

[3]While it is well-understood that membranes exposed to ambient air rapidly carbonize, it has been shown that membranes are effectively "self-purging" at high current densities, with low equilibrium concentrations of carbonate and bicarbonate ions when run at current densities above 1 A/cm^2 in air [14, 15].

[4]*Functionalization* refers to the modification of a molecule to add characteristic properties, in this context the addition of acidic or basic units to enable ion conductivity.

allows them to aggregate and promotes phase separation, which can be tuned by adjusting the length, number, and spacing of the pendants to optimize for desired properties such as ion conductivity [16, 17]. However, it has been shown that a class of polymers containing polyatomic cations either integrated directly into the backbone or on very short pendants can also achieve very strong ion conductivity; two such cations discussed in this thesis, benzimidazolium and imidazolium, are shown in Fig. 1.2. This class of materials is often referred to as polymerized ionic liquids (polyILs) in reference to ionic liquids: salts of polyatomic ions with ambient or near-ambient melting points.

PolyILs have been a topic of research interest since the 1980s, especially in the 2000s, when they were investigated for potential applications as supercapacitor dielectrics or battery electrolytes [18, 19]. Applications to fuel cells or hydrogen electrolyzers were rarely considered until the early 2010s due to the extreme hostility of the OH^- anion to the organic polycations. However, it has since been shown that they can be effectively stabilized via *steric hindrance*: the physical blocking of access to reactive sites with bulky, nonreactive molecular groups [20]. Space-filling models depicting sterically-protected versions of the cations studied in this thesis are shown in Fig. 1.3. It has further been shown that the integration of sterically-protected cations directly into polymer backbones enables a combination of outstanding chemical stability, excellent mechanical strength, and high ion-exchange capacity (IEC) and anion conductivity [21]. Such polymers with ionic backbones are called *ionenes*. However, it is not intuitively clear how these materials are able to achieve high ion conductivity.

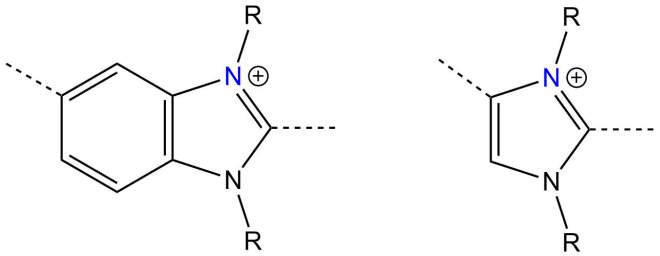

a) Benzimidazolium b) Imidazolium

Figure 1.2: The chemical structures of (a) benzimidazolium, and (b) imidazolium cations, as integrated into the polymer backbones. Despite the formal charge being located on a nitrogen, the charge is centered on the carbon between the two nitrogens in both cations, which is vulnerable to direct hydroxide attack.

PEMs generally absorb significant amounts of water and require this solvation to conduct ions effectively.[5] The nanostructure of PFSA-based PEMs has been researched intensively, and they are known to undergo large-scale phase separation when solvated, self-organizing

[5]High-temperature PEMs that operate at temperatures in excess of 100° C, such as the phosphoric-acid doped PBI common in high temperature PEMFCs, are an exception.

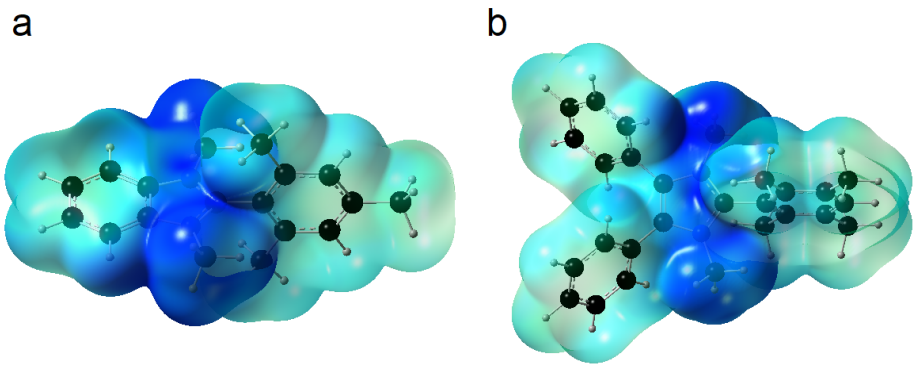

Figure 1.3: Optimized nuclear geometries and electron density isosurfaces of sterically-protected (a) benzimidazolium and (b) imidazolium cations. The vulnerable cation is protected by the four interlocking methyl groups in both systems, and additionally by the two phenyl rings in (b). The transparent isosurface corresponds to an electron density of 0.002 electrons/Å^3, with darker colour corresponding to higher electrostatic potential. These calculations were performed using density functional theory as described in Chapter 3.

into a polymer-rich phase of interconnected crystallites and a percolating water- and ion-rich phase which conducts ions [22]; a schematic diagram of this internal morphology is shown in Fig. 1.4. This complex reorganization is possible due to the location of the acidic functional groups on flexible pendants and the extreme hydrophobicity of the polymer backbones, and is believed to be the source of the material's desirable properties [23]. Similar, albeit simpler, morphologies have been proposed for other CEMs with shorter and less flexible pendants [24, 25, 26]. For example, Reference [24] describes a sulphonated poly(phenylene) CEM as aggregates of closely-packed cylindrical bundles of polymer backbones that are forced apart to accommodate water when solvated. It is not clear what would drive similar phase separation in a system of ionenes.

This thesis provides a comprehensive investigation into the nanostructure of sterically-hindered cationic ionenes sythesized at SFU by members of the Holdcroft group, utilizing a combination of X-ray scattering and computational methods, primarily atomistic molecular dynamics. Chapter 2 presents and discusses available material properties of fully-hydrocarbon ionenes utilizing benzamidazolium and imidazolium cations, focusing on those analyzed in this thesis. Chapter 3 describes the experimental and computational methods utilized in the remainder of the thesis. Chapter 4 provides a detailed analysis of the nanostructure of a potential benchmark hydrocarbon ionene, HMT-PMBI, collecting, synthesizing, and expanding on work from two articles [27, 28]. Chapter 5 compares and contrasts HMT−PMBI with two newer materials, and Chapter 6 presents a new preliminary computational investigation into the anion dynamics and conductivity of these systems.

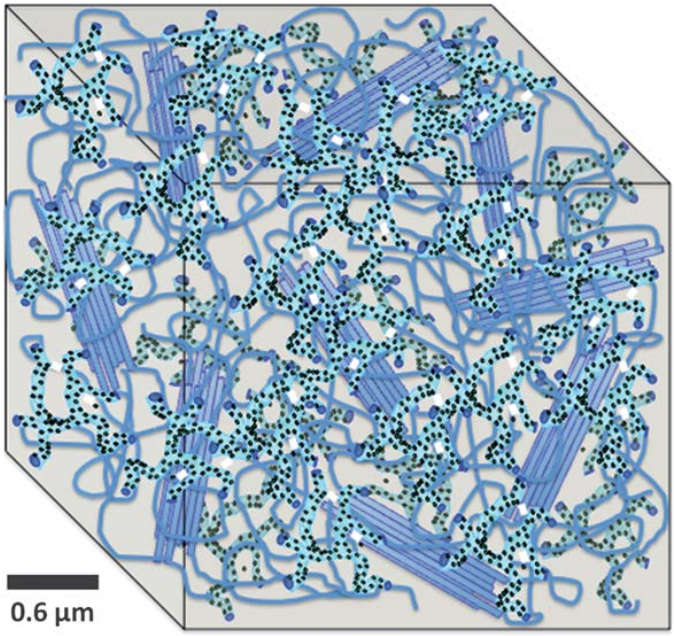

Figure 1.4: A schematic diagram of the internal morphology of hydrated Nafion PFSA, derived from a combination of small-angle neutron scattering, electron microscopy, and dissipative particle dynamics calculations. The black dots represent ion clusters, the blue-green, the water/cation phase, and the light blue, the hydrophobic polymer phase. Reprinted from Reference [22] with permission of the publisher.

Chapter 2

Materials

This chapter will provide an overview of benzimidazolium- and imidazolium-based ionenes from the literature, with emphasis on those studied in this thesis. It will emphasize a number of material properties that are of interest for considering membrane applications, including ion exchange capacity (IEC), water uptake (WU), volumetric expansion (VE), hydration number (λ), and ion conductivity (σ).

2.1 Introduction

The IEC is defined as the number of mobile ions per unit mass of (dry) polymer. Theoretical IEC values are determined from stoichiometry, while experimental values are conventionally determined by titration of counter-ions from solution. For AEM materials, experimental measurements of IEC are usually somewhat lower than theoretical values. This is typically attributed to ions being "trapped" or tightly bound to cations, and for that reason, the experimental IEC is sometimes referred to as the "accessible IEC" [29]. WU and VE are the percentage increase in mass and volume respectively between measurements of dry membranes and measurements after material has been soaked in water, usually for 24 hours, and gently padded dry to remove surface water. Hydration number λ is the number of water molecules per counter-ion, and is often reported as a maximum value, defined as

$$\lambda = \frac{WU}{M_{\text{water}} \times IEC} \ . \tag{2.1}$$

λ is reported as a natural number with no uncertainty by convention. Ion conductivities (σ) are experimentally determined from measurements of resistance using electrochemical impedance spectroscopy (EIS) under controlled humidity, after soaking, and/or while immersed in water. Values reported in this chapter are for "full hydration," after immersion in water, unless stated otherwise.

High IEC and high σ over a wide range of humidities are associated with strong device performance, while low VE is necessary to maintain membrane mechanical integrity in

devices. Unfortunately, these properties are highly correlated – materials with higher IEC generally absorb more water and have higher conductivities, and all materials have higher conductivities under wet conditions. It is common for σ to be reported for membranes submerged in water, and for WU and VE to be measured by comparing the measurements of mass performed in ambient conditions after vacuum-drying and after soaking in water. Unfortunately, these processes are both very prone to error and are not representative of conditions during device operation.

Furthermore, material property measurements of AEMs in hydroxide form—which is the relevant form for fuel cell and electrolyzer applications—are complicated by the reaction of OH^- ions with atmospheric carbon dioxide, which rapidly converts OH^- membranes into mixed $OH^-/HCO_3{}^-/CO_3{}^{2-}$ form. As a result, it is common for hydroxide ion conductivity to be reported in this unknown mixed hydroxide/carbonate form, often with the membrane submerged in degassed water to retard the rate of conversion. In 2018, Ziv and Dekel reported a method for purging membranes of carbonates by applying an external electric current, allowing the "true" hydroxide conductivity to be measured in a pure hydroxide form [30]. Unfortunately, at the time of writing, this technique has only been utilized by three research groups, though a number of promising materials have been measured, including two studied in this thesis [30, 31].

Some of the materials discussed in this thesis were produced to a specific *degree of functionalization* (df), representing the percentage of nitrogens that are functionalized – 50% df corresponds an ion exchange capacity of 0, as both nitrogens in a ring must be functionalized in order for the ring to carry a charge.[1] Literature sources may refer to df, the specific functional units (ie, degree of methylation dm, benzylation db, etc), or the percentage of charged units. Materials without an explicit degree of functionalizion in this chapter are nominally 100% functionalized.

2.2 Benzimidazolium-based polymers

In 2011, methylated poly(benzimidazolium)s (PMBI) were reported as solid polymer electrolytes [32, 33, 34]. These polymers consist of fully aromatic backbones with repeat units containing one phenylene and two benzimidazole or benzimidazolium fusions. They are based on an unfunctionalized analogue, poly(benzimidazole) (PBI). The chemical structures of PBI and PMBI are shown in Fig. 2.1. PBI has wide applications due to its excellent chemical and thermal stability and is commercially available under the trade name Celazole®. Thomas *et al.* reported strong iodide and bromide conductivity [32], and Henkensmeier *et al.*

[1]The synthesis procedures first produce a neutral 50% df form before further functionalization is performed.

Table 2.1: Material properties of PMBI, unprotected benzimidazolium polymers.

% df	counter-ion	IEC (mmol/g)[1]	WU (%)	λ[2]	σ (mS/cm)[3]	reference
73	I^-	1.94	52%	15	5.7	[33]
82	I^-	2.50	68%	15	6.9	[33]
91	I^-	2.95	31.5%	6	4.5	[33]
~ 100	I^-	3.23[4]	12%[5]	2	3.3 ± 0.4	[32]
~ 100	Br^-	3.82[4]	14%[5]	2	3.2 ± 0.4	[32]
~ 100	Cl^-	4.59[4]	1380%[5]	167	7.6 ± 1.1	[32]
~ 100	$HCO_3{}^-$	4.10[4]	37%[5]	5	8.5 ± 0.5	[32]
82	OH^-	3.44	41	7	29.3	[33]

[1] Theoretical

[2] When fully hydrated at room temperature

[3] When immersed in water at room temperature

[4] Calculated from stoichiometry

[5] Calculated from λ via Eq. 2.1

reported strong hydroxide conductivity when fully hydrated at room temperature, despite modest water contents [33].

Selected properties of PBI-based ionenes are reprinted in Table 2.1. Surprisingly, the water content and conductivity of PMBI(I^-) does not appear to increase monotonically with degree of functionalization, and is maximal at 82% df. While these materials were unfortunately not suitable for most device applications, due to the instability of the hydroxide form and the very high water uptake in chloride form, they represented the first successful demonstrations of strong anion conductivity by ionene systems and motivated further study of benzimidazolium-based ionenes.

In 2012, an analogous material stable in OH^- form, mes-PMBI, was reported by Thomas *et al.* [35]. The stability of the cationic unit is provided by steric protection, achieved by replacing the phenyl unit with a mesitylene unit such that the polycation is shielded by four methyl groups, as shown in Fig. 1.3. This has been shown to dramatically increase the transition state energy for hydroxide attack [20]. However, these materials have much higher water uptake than the corresponding PMBI materials, and 100% df mes−PMBI(Cl^-) and mes−PMBI(OH−) are water-soluble. While the water uptake and water solubility of mes-PMBI can be significantly reduced by blending with the unfunctionalized acidic analogue, mes-PBI, which is hypothesized to provide ionic crosslinking, this blending lowers the IEC of the final material substantially by both diluting and neutralizing the alkylated monomers [35]. mes−PMBI(OH−) and each blend were reported to retain over 95% of their IEC after immersion in 2M NaOH at 60°C for thirteen days, which at the time of publishing was the highest level of hydroxide stability reported for an anion-conducting polymer. Unfortunately, the production of the blend membranes requires the use of high-boiling point organic solvents, which limits their potential applications. The chemical structures of mes-PBI and mes-PMBI are shown in Figure 2.2, and selected properties of mes-PMBI and blends are shown in Table 2.2. The mes-PMBI homopolymers show much higher water uptake than unprotected materials of comparable IEC. Despite the low IEC of 1.0, the highest ion conductivity, 13.2 ± 0.1 mS/cm, is shown by 61% mes−PMBI(OH−), due to the extremely high water uptake of blends containing more mes-PMBI. This conductivity is still significantly lower than the reported value for PMBI(OH−), 29.3 mS/cm^3. Conversely, 43% mes−PMBI(I^-) shows similar hydration and conductivity at a lower IEC than 82% df PMBI(I^-): 12, 7.37 mS/cm, and 1.41 mmol/cm^3 vs. 15, 6.9 mS/cm^3, and 2.50 mmol/cm^3 for 82% df PMBI(I^-), respectively.

In 2014, a derived methylated polybenzimidazolium-based polymer with a longer monomer unit containing additional hydrophobic material was reported as HMT−PMBI by Wright and Holdcroft [37]. While the 100% functionalized material is also water-soluble in hydroxide form, the water uptakes can be easily modulated by controlling the degree of functionalization. In 2016, a scaled-up synthesis and characterization of 89.7% df HMT−PMBI was reported as a potential benchmark material for alkaline energy conversion devices, as it possesses strong anion conductivity, good processability, and excellent chemical and mechanical stability; it is soluble in low-boiling-point solvents such as methanol and is stable in 1M KOH at 80°C and 6 M KOH at room temperature [38]. The material was also demonstrated as a fuel cell membrane and ionomer with stable performance at 60°C for at least 95 hours, and as a hydrogen electrolyser membrane for 144 hours. When completely purged of carbonates and measured under hydrolysis at 40°C and 90% RH, hydroxide ion conductivity of 103 mS/cm, comparable to high-performance hydrocarbon-based proton-exchange membranes under similar temperatures and humidities, has been demonstrated [30].

Table 2.2: Material properties of pristine and blended mes–PMBI, sterically-protected benzimidazolium polymers.

ratio [4]	counter-ion	IEC (mmol/g)[1]	WU (%)	λ[2]	σ (mS/cm)[3]	reference
100%	OH^-	4.52[6]	∞	∞	N/A	[35]
100%	Cl^-	4.18[6]	∞	∞	N/A	[36]
100%	Br^-	3.53[6]	82 ± 6	13[7]	9.9 ± 0.4	[36]
100%	I^-	3.02[6]	152 ± 8	27[7]	6.0 ± 0.3	[36]
76%	OH^-	2.5	∞	∞	N/A	[35]
70%	OH^-	2.0	162 ± 10	45	9.6 ± 0.1[5]	[35]
65%	OH^-	1.5	119 ± 6	32	10.1 ± 0.1[5]	[35]
61%	OH^-	1.0	82 ± 3	22	13.2 ± 0.1[5]	[35]
76%	I^-	1.77[6]	112 ± 8	24	N/A	[32]
70%	I^-	1.41[6]	51 ± 5	12	7.37 ± 0.06	[36]
65%	I^-	1.08[6]	44 ± 6	10	5.99 ± 0.06	[36]
61%	I^-	0.81[6]	18 ± 5	4	3.59 ± 0.09	[36]

[1] Theoretical

[2] When fully hydrated at room temperature

[3] When immersed in water at room temperature

[4] By mass, blended with mes-PBI

[5] Measured in mixed $OH^-/HCO_3{}^-/CO_3{}^{-2}$ form

[6] Calculated via stoichiometry

[7] Calculated via Eq. 2.1

Table 2.3: Material properties of HMT-PMBI, advanced sterically-protected benzimidazolium polymers. Multiple selected values are included where independent measurements exist.

% df	counter-ion	IEC (mmol/g)[1]	WU (%)	λ[6]	VE (%)	σ (mS/cm)[2]	reference
66	OH^-	1.1	29 ± 4	14	Not measured	0.10 ± 0.03[4]	[40]
73	OH^-	1.5	36 ± 3	13	Not measured	0.45 ± 0.06[4]	[40]
80	OH^-	2.0	42 ± 3	12	Not measured	1.4 ± 0.2[4]	[40]
90	OH^-	2.5	80 ± 20	18, 12[38]	78	6.1 ± 1.2[4]; 103 [30] [5]	[40]
92	OH^-	2.7	180 ± 50	37	Not measured	9.7 ± 0.6[4]	[40]
~ 100	OH^-	3.1	∞	∞	∞	N/A	[40]
90	F^-	2.54	53	12	55	6.2 ± 0.2	[40]
90	Cl^-	2.41	36	9, 22 ± 2 [39]	63	7.5 ± 0.4	[38]
90	Br^-	2.18	25	6, 10 ± 1 [39]	45	4.2 ± 0.6	[38]
90	I^-	1.98	16	4, 6 ± 1 [39]	29	0.87 ± 0.1	[38]
90	$HCO_3{}^-$	2.27	51	12, 25 ± 2 [39]	74	3.8 ± 0.4	[38]
90	$CO_3{}^{-2}$	2.44	43	20, 21 ± 1 [39]	56	2.0 ± 0.2	[38]

[1] Theoretical

[2] When fully hydrated at room temperature

[3] When immersed in water at room temperature

[4] Measured in mixed $OH^-/HCO_3{}^-/CO_3{}^{-2}$ form

[5] Measured under hydrolysis at 40°C, 90% RH

[6] Calculated from WU via Equ 2.1

The chemical structure of HMT−PMBI is shown in Fig. 2.3, and selected material properties are tabulated in Table 2.3. HMT−PMBI material properties follow expected trends, as samples with higher IEC and/or more hydrophilic anions show higher water uptakes and ion conductivities. At the few points of overlap with similar IEC—that is iodide form at IEC 2 and hydroxide/mixed carbonate form at IEC 1.5 and 2—lower ion conductivities were reported for HMT−PMBI than PMBI and mes-PMBI samples. In particular, the blended membranes showed much higher water uptake and hydroxide ion conductivity, which may be impacted by acid/base conjugation. However, at similar water contents, HMT−PMBI shows greater conductivity. Table 2.3 does highlight one major concern: water contents reported in different literature sources often do not agree. Here, values reported in Reference [38] are much lower than those reported in Reference [39] and [40].

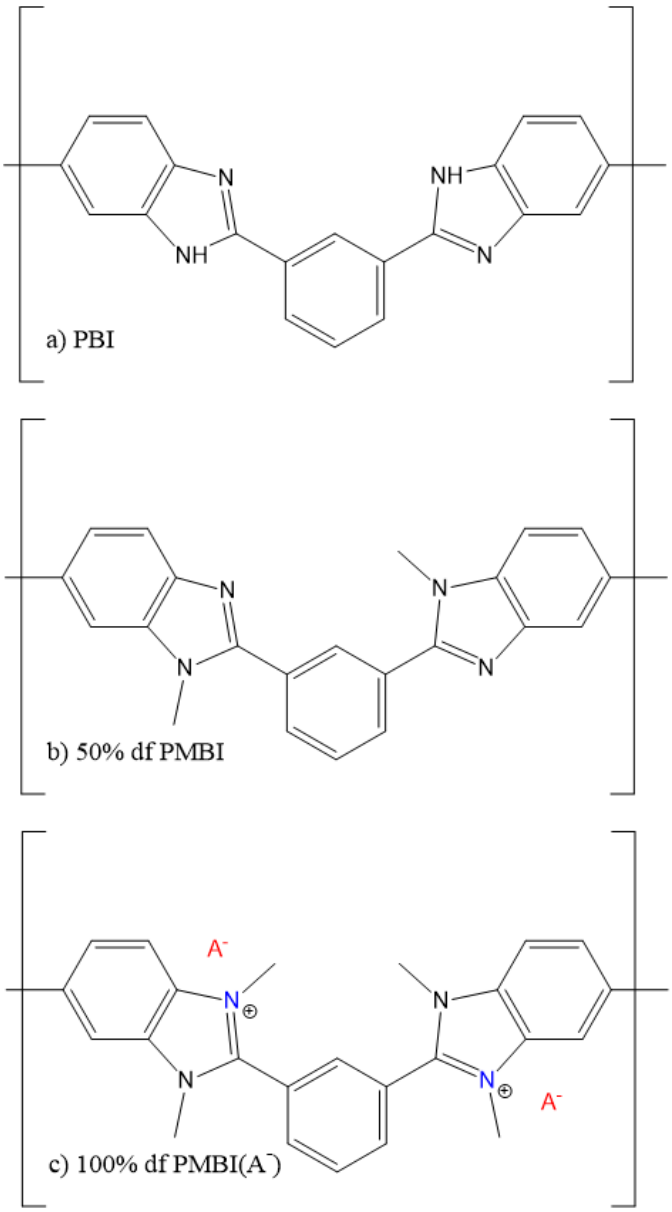

Figure 2.1: The chemical structures of a) PBI, b) 50% df PMBI, and c) 100% df PMBI(A^-). A^- is an arbitrary counter-ion.

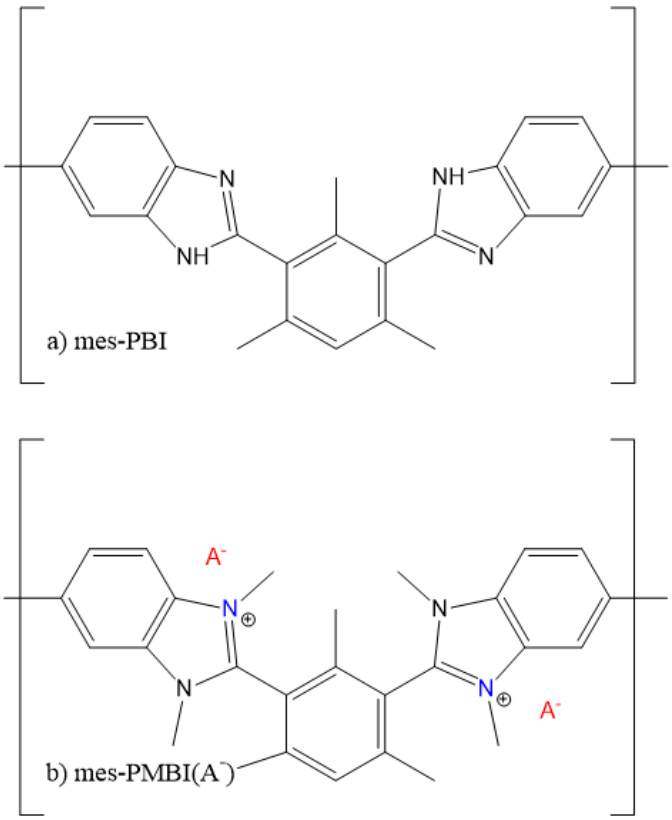

Figure 2.2: The chemical structures of a) mes−PBI and b) mes−PMBI(A^-).

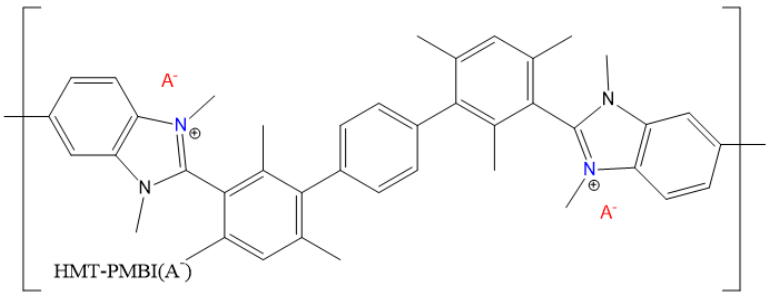

Figure 2.3: The chemical structure of fully functionalized HMT−PMBI(A^-), a protected benzimidazolium polymer.

2.3 Imidazolium-based polymers

Imidazolium-based compounds have been found to be more resistant to OH^- attack than their benzimidazolium-based counterparts [41, 42], likely because the extended conjugated structure of benzimidazoliums stabilizes ring-opening transition states. An imidazolium-based analogue to HMT-PMBI, HMT-PMPI, was reported in 2017 and was shown to be stable in 10M KOH at 100^oC for at least seven days [43]. Unfortunately, the material swells excessively and is soluble in high-temperature water in both chloride and hydroxide form when fully functionalized, limiting potential applications.

Other sterically-protected imidazoliums, TMP-PMPI and DMP-PMPI, were developed concurrently and reported in 2019 by Fan *et al.* [44], by Li [45], and by Overton *et al* [46]. The chemical structures of these materials are shown in Fig. 2.4; TMP-PMPI consists of a large, symmetric monomer containing seven total rings and a +2 nominal charge when fully functionalized, while DMP-PMPI consists of a smaller asymmetric monomer containing four rings and a +1 nominal charge. Rather than varying the degree of functionalization, these materials were functionalized with different alkylating units,[2] which modulated the water uptake with less impact on the IEC, and offered the additional benefit of increasing the hydroxide stability of the materials [44]. The nomenclature TMP-PMPI-XY and DMP-PMPI-XY is used in this thesis to indicate the alkylation units, where X and Y can be M, E, P, or B for methyl-, ethyl-, propyl-, and butyl-substituted materials, respectively.

Both series show outstanding chemical stability; $TMP-PMPI-BB(OH^-)$ was demonstrated as a fuel cell membrane and $TMP-PMPI-EE(OH-)$ and $TMP-PMPI-BB(OH-)$ were demonstrated as hydrogen electrolyser membranes [44]. Under the electrolysis method discussed above, 94% df $DMP-PMPI-MM(OH^-)$ demonstrated a hydroxide ion conductivity of 120 mS/cm^2, which is among the highest reported in the literature [31] at the time of writing.

[2]Both materials were also synthesized with several degrees of functionalization, but this was not pursued as lengthening the alkane units produced more desirable properties.

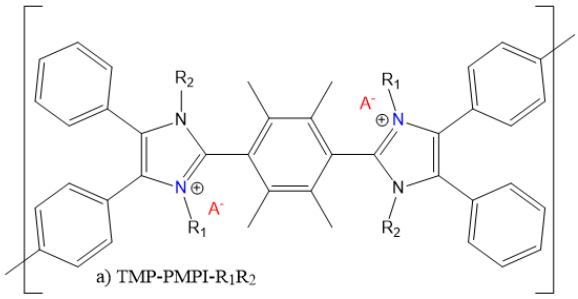

a) TMP-PMPI-R_1R_2

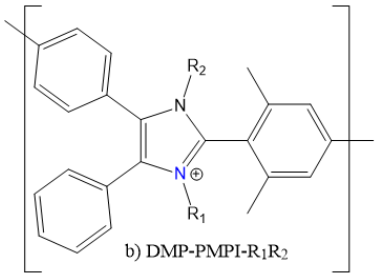

b) DMP-PMPI-R_1R_2

R_1, R_2 =			
M	E	P	B
		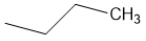	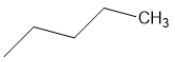

Figure 2.4: The chemical structures of TMP-PMPI and DMP-PMPI, protected imidazolium polymers.

Table 2.4: Material properties of sterically-protected imidazoliums TMP – PMPI and DMP – PMPI.

% df	material	counter-ion	IEC (mmol/g)[1]	WU (%)	λ[2]	VE (%)	σ (mS/cm)[3]	reference
~ 100	HMT – PMPI	OH^-	2.62	82 ± 5	18		14[4]	[43]
~ 100	HMT – PMPI	Cl^-	2.50				10	[43]
~ 100	TMP – PMPI – MM	Cl^-	2.86	48.2 ± 1.3	9	45 ± 2	32.7 ± 2.4	[44]
~ 100	TMP – PMPI – EE	Cl^-	2.65	28.1 ± 1.6	6	26 ± 4	21.3 ± 1.6	[44]
~ 100	TMP – PMPI – PP	Cl^-	2.46	22.3 ± 1.3	5	20 ± 2	14.8 ± 1.2	[44]
~ 100	TMP – PMPI – BB	Cl^-	2.30	12 ± 2	3	14.0 ± 1.2	8.5 ± 0.7	[44]
62	DMP – PMPI – MM	Cl^-	0.69	$2.7 \pm 1.3\%$	2		3.0 ± 0.9	[44]
72	DMP – PMPI – MM	Cl^-	1.23	$11 \pm 2\%$	5		3.9 ± 1.5	[45]
78	DMP – PMPI – MM	Cl^-	1.52	$15 \pm 2\%$	5		4.8 ± 1.5	[45]
82	DMP – PMPI – MM	Cl^-	1.72	$22 \pm 4\%$	7		8 ± 2	[45]
88	DMP – PMPI – MM	Cl^-	2.06	$28 \pm 7\%$	8		11 ± 3	[45]
95	DMP – PMPI – MM	Cl^-	2.34	$33 \pm 5\%$	8		15 ± 4	[45]
~ 100	DMP – PMPI – MM	Cl^-	2.58	32.6 ± 4.3	7	13 ± 0.8	15 ± 4	[45]
~ 100	DMP – PMPI – EE	Cl^-	2.41	26.9 ± 3.3	6	10.7 ± 0.9	9.82 ± 3.26	[45]

[1] Theoretical

[2] When fully hydrated at room temperature

[3] When immersed in water at room temperature

[4] Measured in mixed $OH^-/HCO_3{}^-/CO_3{}^{-2}$ form

2.4 Materials studied in this thesis

Due to their tunable properties, potential for device applications, and availability, HMT−PMBI, TMP−PMPI, and DMP−PMPI were chosen for study, with HMT−PMBI being the focus of in-depth analysis due to the greater availability of materials and the more in-depth existing characterization of material properties. Synthesis of HMT−PMBI, TMP−PMPI, and DMP−PMPI were performed by Dr. Andrew Wright and Mr. Binyu Chen, Dr. Jiantao Fan, and Mr. Wei Li, respectively. Each membrane was initially cast in iodide form from DMSO immediately after synthesis. Membranes were then immersed in 1 M NaCl, KBr, or KI salt solutions for at least 72 hours to exchange the counter-ions. Salt solutions were changed every eight hours. A previous investigation showed that 48-hour immersion was sufficient to exchange at least 90% of the counter-ions in HMT−PMBI; that research concluded that the remaining counter-ions were inaccessible [29]. Samples were cast from DMSO to target thicknesses of 30 μm, which were found to provide acceptable membrane strength and are comparable to commercial ion-exchange membrane thicknesses; actual thicknesses ranged from 30 μm to 55 μm. HMT−PMBI samples were then redissolved and recast from DMSO in order to eliminate membrane history; this was not found to have a significant effect on the water uptake or X-ray scattering profiles of the samples when exchanging between different halides [47]. After casting, samples were washed with deionized (DI) water and dried in vacuum for at least eight hours. TMP−PMPI and DMP−PMPI were not recast due to limited membrane availability. Preparation of HMT−PMBI and TMP−PMPI samples were performed by Binyu Chen and Jacob Stewart, and preparation of DMP−PMPI samples were performed by Wei Li. For convenience, available material properties for materials studied in this thesis are tabulated in Table 2.5.

2.4.1 Properties at controlled humidity

Measurements of hydration and conductivity at controlled humidity are of particular interest as this thesis focuses on the evolution of nanostructure with hydration;[3] X-ray scattering experiments were performed at controlled humidity, so information about the relative water content at different conditions is useful for understanding the experiments. Measurements at controlled humidity are of even greater importance for preparing and analyzing molecular dynamics simulations, as the number of water molecules in the system must be defined at the beginning of the simulation, and observable properties must be validated against experimental results when possible. While existing experimental data is limited, a selection of

[3]Fully-hydrated conductivity is not entirely representative of device conditions; in an AEMFC, water is consumed at the cathode and produced at the anode, so a significant gradient in water content is expected to develop. While fuel cells are typically operated at temperatures of at least 60°C, this thesis focused on room temperature investigations, so elevated temperature experiments are not printed here. Interested readers are directed to References [29], [38], [45] and [48] for conductivity measurements at elevated humidity.

Table 2.5: Selected properties of materials studied in this thesis in chloride form.

material	IEC (mmol/g)[1]	WU (%)	λ[2]	VE (%)	σ_{wet} (mS/cm)[3]	σ_{RH} (mS/cm)[7]	reference
85% df HMT–PMBI	2.18	35.4	9[4]	46.3	7.6 ± 0.4	3.4 [8]	[29]
TMP–PMPI–MM	2.86	48.2 ± 1.3	9	45 ± 2	32.7 ± 2.4	16.9	[44]
TMP–PMPI–EE	2.65	28.1 ± 1.6	6	26 ± 4	21.3 ± 1.6	12.9	[44]
TMP–PMPI–PP	2.46	22.3 ± 1.3	5	20 ± 2	14.8 ± 1.2	6.4	[44]
TMP–PMPI–BB	2.30	12 ± 2	3	14.0 ± 1.2	8.5 ± 0.7	2.8	[44]
DMP–PMPI–MM	2.58	32.6 ± 4.3	7	13 ± 0.8	15 ± 4	2.4[5] [46]	[45]
DMP–PMPI–EE	2.41	26.9 ± 3.3	6	10.7 ± 0.9	9.82 ± 3.26	2.0	[45]
DMP–PMPI–PP	2.26	Not measured				0.5 [6]	[46]

[1] Theoretical

[2] When fully hydrated at room temperature

[3] When immersed in water at room temperature

[4] Calculated from WU via Eq. 2.1

[5] 94% df sample

[6] 87% df sample. Fully-hydrated measurements were not performed

[7] Chloride ion conductivity at high humidity: 30° C, 95% RH unless otherwise noted

[8] Measured at 25° C, 90% RH

available results are reproduced here. Unfortunately, no experimental data beyond chloride ion conductivity at 95% RH is available for TMP–PMPI.

The results of dynamic vapour sorption experiments, in which the mass of each sample is measured at various humidities and/or temperatures and compared to a nominally dry mass at low humidity and elevated temperature, performed on 89.7% df HMT–PMBI(Cl^-) [49] and DMP–PMPI–MM(Cl^-) [45] samples are shown in Figure 2.5a. These measurements present a concerning discrepancy with the reported maximum hydration values; the HMT–PMBI(Cl^-) results show a higher water content at 95% RH than the reported maximum value in Reference [38]—$\lambda = 13$ at 95% RH and 30°C, and $\lambda = 9 \pm 2$ after full hydration at room temperature—and the measurement of DMP–PMPI–MM(Cl^-) shows much higher water content at each relative humidity condition measured than the $\lambda = 7$ at full hydration reported in Reference [45]. Other literature sources report significantly different water uptakes for 89.7% dm HMT–PMBI(Cl^-), including $\lambda = 16$ [28] and $\lambda = 10$ [39], both at ambient temperature. There are no other literature sources for fully-hydrated DMP–PMPI–MM(Cl^-) at the time of writing.

While sample-to-sample differences in molecular weight [50], as well as potential variations in casting or ion exchange procedures, may result in genuinely different water uptakes, the author suspects a large contribution may be error in reported water uptakes due to the extreme difficulty of measuring water content precisely, particularly via 'bench-top' techniques. Even DVS measurements require measuring a reference mass at low humidity and high temperature, but it is impossible to verify that this state corresponds to $\lambda = 0$; in fact, it is understood that achieving a truly dehydrated state is impossible. Even more problematic, bench-top measurement of the maximum hydration number involves measur-

ing a "dry" sample in ambient humidity—usually immediately after vacuum-drying—and measuring the "wet" sample after extended soaking, followed by removing surface water with a tissue. Both of these procedures will certainly produce inconsistent values for the dry reference mass.

Finally, ion conductivity vs. hydration number for two available samples, 90% df HMT−PMBI(Cl^-) and 94% df DMP−PMPI−MM(Cl^-), are plotted in Fig. 2.5, showing that the dependence of conductivity on hydration number is very different for different backbone architectures. Both samples show non-linear increases in σ with λ, and HMT−PMBI(Cl^-) shows much greater conductivity than DMP−PMPI−MM(Cl^-) at all values of λ, in sharp contrast to the fully-hydrated results discussed above. This further suggests that there may be inconsistency between samples and/or measurements, particularly of fully-hydrated conductivity or water content. This will be further discussed in Chapter 6.

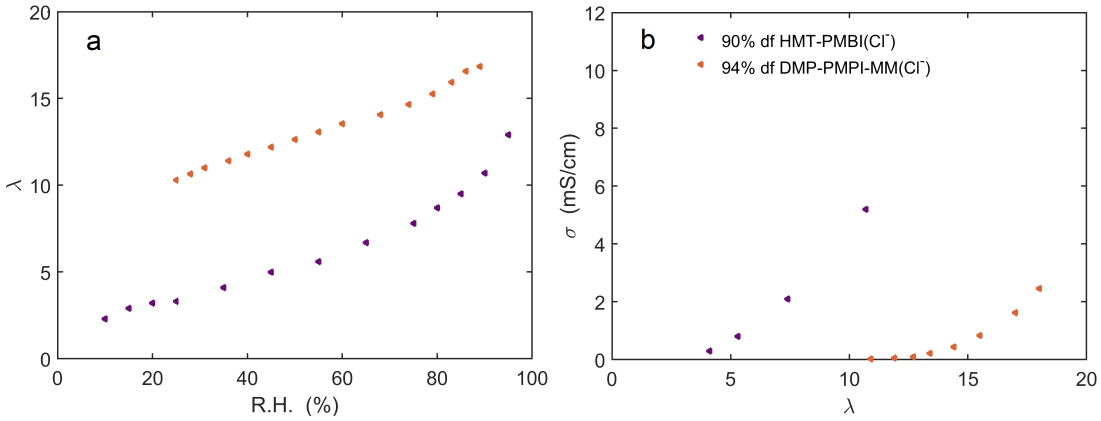

Figure 2.5: (a) Hydration numbers of 90% df HMT−PMBI(Cl-) [49] and 94% df DMP−PMPI−MM(Cl^-)[46] as a function of RH at 30 °C, and (b) Ion conductivity of 90% df HMT−PMBI(Cl^-) (25 °C [29]) and 94% df DMP−PMPI−MM(Cl^-) (30 °C [46]) as a function of hydration number. For HMT−PMBI(Cl^-), the reference dry mass was measured after drying at 0% RH, 60C° for 60 min; for DMP−PMPI−MM(Cl^-), the reference dry mass was measured after drying for 24 h at 80C° in vacuum, then equilibration with 0% RH, 100C° for 12 h.

Chapter 3

Methods

3.1 Introduction

The most common techniques for investigating the nanostructure of polymer films include microscopy, scattering, and computational methods. Microscopy directly produces a magnified, high-resolution 2D image of a sample. The most common microscopy techniques in polymer science are electron microscopy and atomic force microscopy, which both have sub-micrometer resolutions. For example, a TEM micrograph of TMP–PMPI–MM(I–), reproduced in Fig. 3.1, shows nm-scale heterogeneity, but homogeneity at larger length scales. While micrographs can easily be visualized, interpretation can be challenging and they are limited by their two-dimensional nature; atomic force microscopy can only probe surfaces, and electron microscopy is typically depth-averaged over a very thin sample exposed to vacuum, which is of limited utility for investigations of membrane materials that readily absorb and desorb water and are designed to operate in humid conditions.

In contrast, scattering techniques provide information in reciprocal space about a large illuminated sample volume—typically at least 0.1 mm^3—and can condense structural information about length scales ranging from 0.1 nm to 100 nm into a single one-dimensional plot. While this information may not be intuitive to visualize, it is more representative of bulk structure than two-dimensional micrographs.

Scattering can be performed using light, X-rays, or neutrons. X-ray and light scattering primarily differ in the wavelength of the incident radiation and correspondingly access different length scales, though the contrast can differ as well due to the wavelength dependence of material refractive index.[1] Neutron scattering is unique in that it probes the distribution of nuclei rather than electrons.

Computational methods, including atomistic and coarse-grained molecular dynamics as well as statistical techniques, have the advantage of great interpretability, but generally

[1] At optical wavelengths, refractive index primarily depends on a materials' polarizability, while at hard X-ray wavelengths, it is directly proportional to the electron density away from absorption lines.

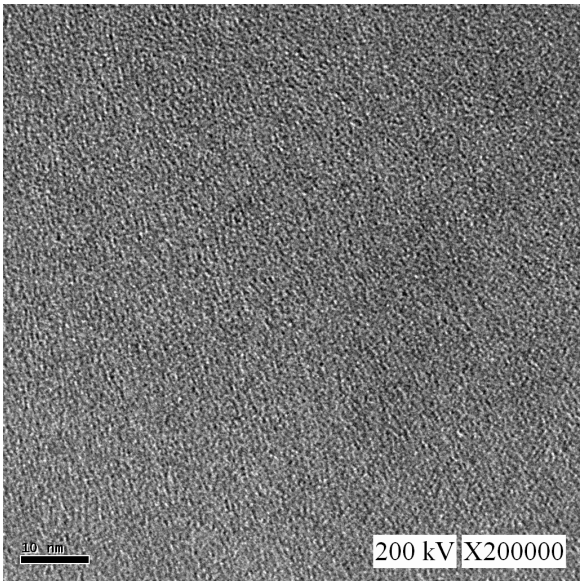

Figure 3.1: A TEM micrograph of TMP−PMPI−MM(I−). Reprinted from Reference [44] under the Creative Commons 3.0 license.

must be validated against experimental data. Molecular dynamics allows the simulation of large ensembles of molecules by abstracting intra- and inter-molecular interactions to easily-calculated functions and representing atoms, molecules, or molecular fragments as single distinct particles, and is particularly useful because it allows the calculation of both static and dynamic properties.

3.2 X-ray scattering

An X-ray scattering experiment is performed by directing a collimated beam of monochromatic X-rays onto a sample and measuring the angular dependence of the scattered radiation. This can be done in either transmission geometry, in which the beam passes directly through the sample, or in reflection geometry, in which the beam is reflected off a sample surface or interface. This thesis will focus on transmission geometry, which is much more common in the study of soft matter; reflection geometry can be used to study single crystals, interfaces, and substrate-supported thin films. X-ray scattering is an excellent tool for studying the shape of synthetic or biological macromolecules, self-assembly or aggregation of particles in solution, and phase separation in solid materials. X-ray and neutron scattering are often the primary techniques used to observe crystallinity or phase separation in polymer materials [51].

An X-ray scattering experiment is schematized in Fig. 3.2: collimated X-rays are directed to a sample, and the intensity of scattered radiation is observed as a function of the change in photon momentum, referred to as the *scattering vector* $\vec{q}$, typically by a two-dimensional detector some distance away. In unoriented samples, the intensity is integrated azimuthally to give $I(q)$, where q is the magnitude of the scattering vector. q is related to the scattering angle and the wavelength of the incident radiation,

$$|\vec{q}| = \frac{4\pi}{\lambda} \sin(\theta) \ , \tag{3.1}$$

where 2θ is the scattering angle and λ is the wavelength of the incident radiation.

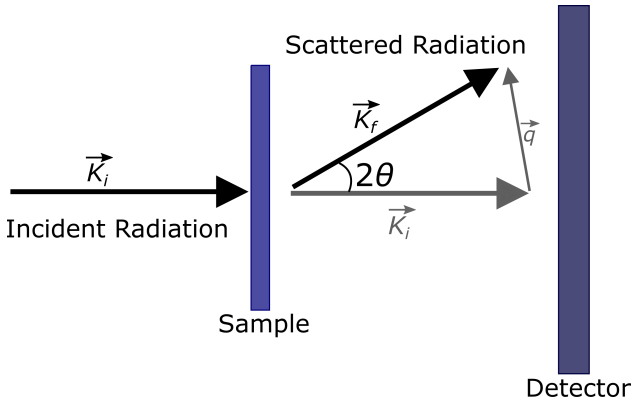

Figure 3.2: A schematic of an X-ray scattering apparatus in transmission geometry [52].

The X-rays primarily interact with the electrons in the sample via Thompson scattering, as they have energies much lower than the rest mass energy of the electron. Regions of high electron density scatter more X-rays than regions of low electron density, so the interference pattern observed at the detector provides information about the distribution of electron

density.[2] The *scattering factor* $F(\vec{q})$ represents a Fourier transform of the distribution of electron density in the illuminated sample,

$$F(\vec{q}) = \int_V \rho(\vec{r}) \exp\left(i\ \vec{q}\cdot\vec{r}\right)\ d\vec{r}\ , \tag{3.2}$$

and the observed intensity at the detector is equal to the square of the scattering factor,

$$I(\vec{q}) = F^*(\vec{q})F(\vec{q})\ . \tag{3.3}$$

3.2.1 Wide-angle X-ray scattering

X-ray scattering is conventionally divided into wide-angle (WAXS), which considers scattering angles above approximately 5° and provides information about inter-atomic lengthscales from 0.1 nm to 1.0 nm, and small-angle (SAXS), which considers smaller scattering angles and larger lengthscales from 1 nm to 100 nm or greater. While the distinction is somewhat arbitrary, it is useful for visualizing which inhomogeneities provide the contrast. In WAXS (and X-ray diffraction (XRD), which is essentially the same technique but focused only on single crystals or crystalline powder samples), atoms are generally thought of as sources of approximately spherical X-ray waves due to the concentration of electrons near the nucleus, though in fact even a single atom has a broad forward scattering maximum analogous to a single slit in the familiar 1D interferometry experiment.[3] The scattering factor of a single, discrete particle is by convention referred to as the *form factor* $F_j(\vec{q}) = \int_V \rho_j(\vec{r}) \exp\left(i\ \vec{q}\cdot\vec{r}\right)\ d\vec{r}$, while interference between scattering from different particles is referred to as the *structure factor*. The form factors of several atoms and ions are plotted in Fig. 3.3. The *scattering factor* of an ensemble of discrete particles can be described as,

$$F(\vec{q}) = \sum_{\text{particles } j} F_j(\vec{q}) \exp\left(i\ \vec{q}\cdot\vec{r}_j\right)\ , \tag{3.4}$$

giving a scattering intensity of

$$I(\vec{q}) = F^*(\vec{q})F(\vec{q}) = \sum_j \sum_k F_j(\vec{q})F_k(\vec{q}) \exp\left(i\ \vec{q}\cdot\vec{r_{jk}}\right)\ , \tag{3.5}$$

where $\vec{r_{jk}} = (\vec{r_k} - \vec{r_j})$.

WAXS is most commonly used to probe for or study crystallinity, as it can provide precise information about crystalline spacings because each observable maxima represents a

[2]The one exception is when the incident X-rays are near an absorption line of electrons in the sample. This can be utilized to highlight certain chemistries in a system via a powerful technique called resonant inelastic X-ray scattering (RIXS).

[3]Polarized X-ray sources will produce scattering primarily along the axis of polarization, but this is typically corrected for.

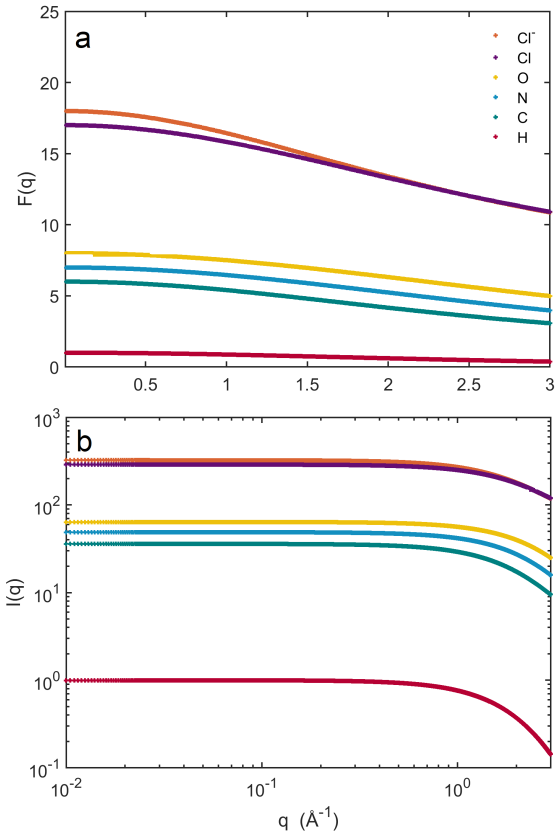

Figure 3.3: The a) form factor $F(q)$ and b) the scattered intensity $I(q)$ of several single atoms and ions. Larger particles have a narrower form factor, with amplitude at $q = 0$ proportional to the total number of electrons; for example, the amplitude of the Cl^- ion form factor is slightly greater than that of the Cl atom, but they are indistinguishable at high q. The scattered intensity, when plotted logarithmically, appears constant at low q, but drops off rapidly near 1 $Å^{-1}$.

reciprocal lattice vector and the corresponding crystallographic spacing $d = r_{jk}$. A schematic of this condition is shown in Fig. 3.4. This can be understood intuitively via Bragg's Law, which emphasizes the fact that the maxima correspond to integer differences in optical path length,

$$2d \sin\theta = n\lambda \ , \tag{3.6}$$

where d is the crystallographic spacing and n is a natural number corresponding to the order of the peak; first-order peaks are usually much more intense than higher-order peaks. Bragg's Law can also be written more simply in terms of q, as

$$d = \frac{2\pi n}{q} \ . \tag{3.7}$$

An example of scattering from a crystalline sample, silver behenate (AgBeh), recorded via a 2D detector is shown in Figure 3.5. The sample is a powder containing many small, randomly-oriented crystallites, so the superposition of the intensity maxima appear as circular rings.

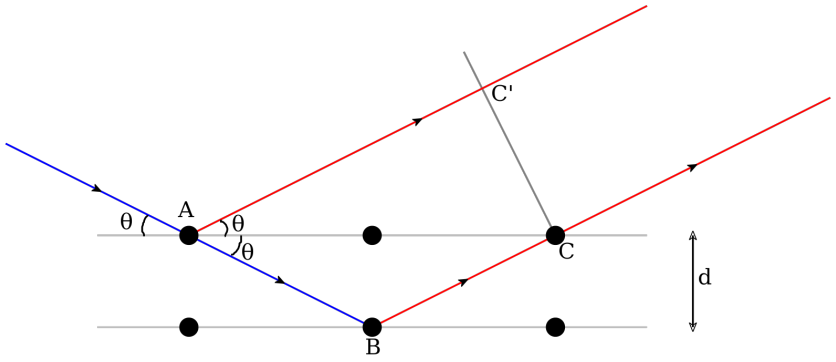

Figure 3.4: A schematic of the Bragg condition. Sharp intensity maxima will be visible at θ where |AC'| + $n\lambda$ = |AB| + |BC|.

WAXS can also provide limited information about noncrystalline material. For isotropic materials, Eq. 3.5 can be spherically averaged, resulting in the Debye scattering equation,

$$I(q) = \left\langle F(\vec{q})^2 \right\rangle = \sum_j \sum_k F_j(q) F_k(q) \frac{\sin(q\ r_{jk})}{q\ r_{jk}} \ . \tag{3.8}$$

The sinc function $\frac{\sin(q\ r_{jk})}{q\ r_{jk}}$, plotted in Fig. 3.6, shows a broad maxima at $q = 7.725/r$, just under $\frac{5\pi}{2r}$. This suggests that, although it is common in the literature to assign amorphous peaks to length scales given by the Bragg equation, $\frac{2\pi}{q_0}$, a common spacing in entirely amorphous material produces a peak of up to 23% greater q_0 than the corresponding crystalline spacing. A broad peak corresponding to spacing between amorphous polymer chains is suggested to indicate an interchain spacing of $\frac{2.44}{q_0}$ for unoriented polymers and $\frac{2.22}{q_0}$ for uniaxially oriented polymers [53, 54]. In this thesis, I report values

$$d \approx \frac{2.44\pi}{q_0} \ , \tag{3.9}$$

for spacings associated with noncrystalline WAXS peaks, with the caveat that they are approximate.

3.2.2 Small-angle X-ray scattering

Small-angle X-ray scattering (SAXS) focuses on length scales above 1 nm. For that reason, it is less helpful to consider atoms as individual sources of X-rays and better to consider

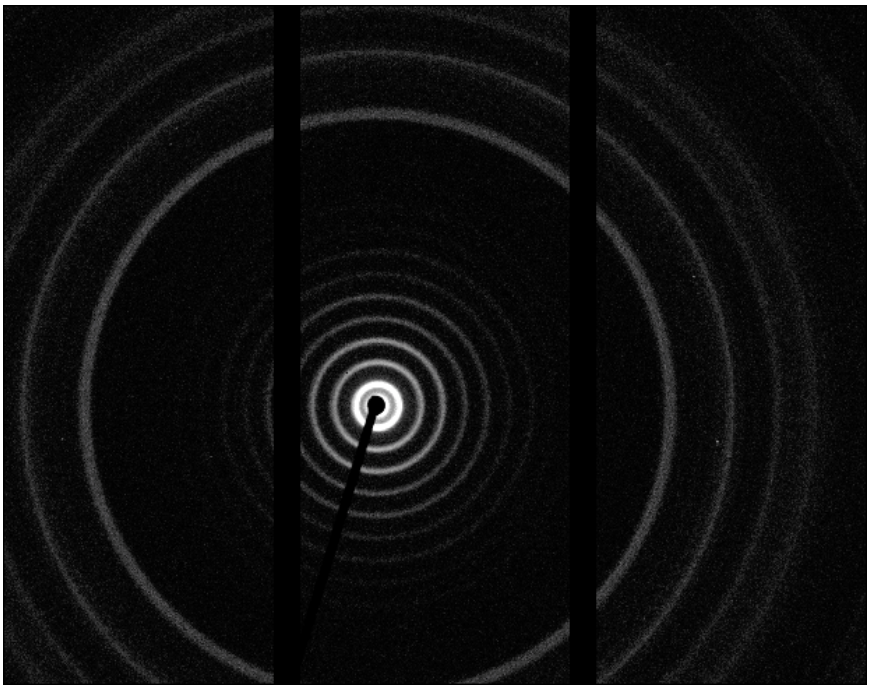

Figure 3.5: Scattering from an AgBeh sample wrapped in aluminum foil. The direct beam is blocked by a circular beam stop, and a shadow is also cast by the rectangular beamstop holder in the lower central segment. The detector consists of three individual image plates, which are offset slightly, leaving the two narrow gaps visible in the reconstructed image.

the continuous distribution of electron density throughout the illuminated sample. The difference in the electron density between different chemistries or phases of interest in a system is referred to as the *X-ray contrast*. The most intuitive application of SAXS to polymer films is block copolymers, which often phase separate in a regular fashion into spherical, lamellar, or gyroidal domains. Unfortunately, in cases where the order is not long-ranged, each of these morphologies manifest in the SAXS profile as a single broad peak. SAXS profiles can also contain information about the size and shape of disordered inhomogeneities in a sample; for example, samples of dilute polydisperse spheres show a broad shoulder at low q of width $q_0 = 4.91/R$, where q_0 is position of the first minimum and R is the mean radius. In practice, it is not always obvious whether a feature in the low-q region is a peak or a shoulder, so supplemental experiments and intuition about the sample are often needed.

SAXS profiles can generally be separated into low-q *Guinier* and high-q *Porod* regimes. In the Guinier regime, where $q < \frac{\pi}{R_G}$, the radius of gyration can be extracted from a fit of

$$I(q) = I_0 \exp(-\frac{({R_G}^2 q^2)}{3}) \tag{3.10}$$

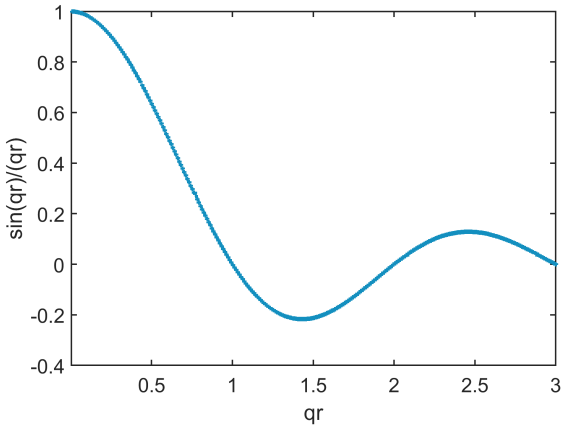

Figure 3.6: A plot of the sinc function, $\frac{\sin(qr)}{qr}$.

Table 3.1: Some common Porod exponents [55].

System	Exponent
3D object with smooth surface	4
3D object with rough surface	3-4
2D object (sheet)	2
1D object (thin rod)	1
Self-attracting polymer	2-3
Ideal polymer (i.e., in θ-solvent)	2
Self-avoiding polymer	$\frac{5}{3}$-2

to the low-q regime, or equivalently, extracted from the slope of a plot of $\log(I(q))$ vs q^2. In the high-q region, where $q > \frac{\pi}{R_G}$, the scattered intensity is proportional to q^{-n}, where n is the *Porod exponent*.[4] The Porod exponent provides information about the dimensionality of the sample: $I \sim q^{-4}$ is representative of large, smooth objects; $I \sim q^{-1}$, 1D rods. The most common Porod exponents are listed in Table 3.1.

Example plots showing the transition from the Guinier to Porod regimes for simple systems of dilute are shown in Fig. 3.7.

3.2.3 Experimental X-ray scattering procedure

X-ray scattering experiments were performed using the SAXSLab Ganesha 300XL located at 4D Labs. The instrument consists of a CuKα source, a mobile stage, and a mobile CCD detector enclosed in a large airtight chamber that is evacuated for measurements. Three adjustable slit collimators, the sample stage, and the detector are free to move independently

[4]This comes from a high-q expansion of the form factor.

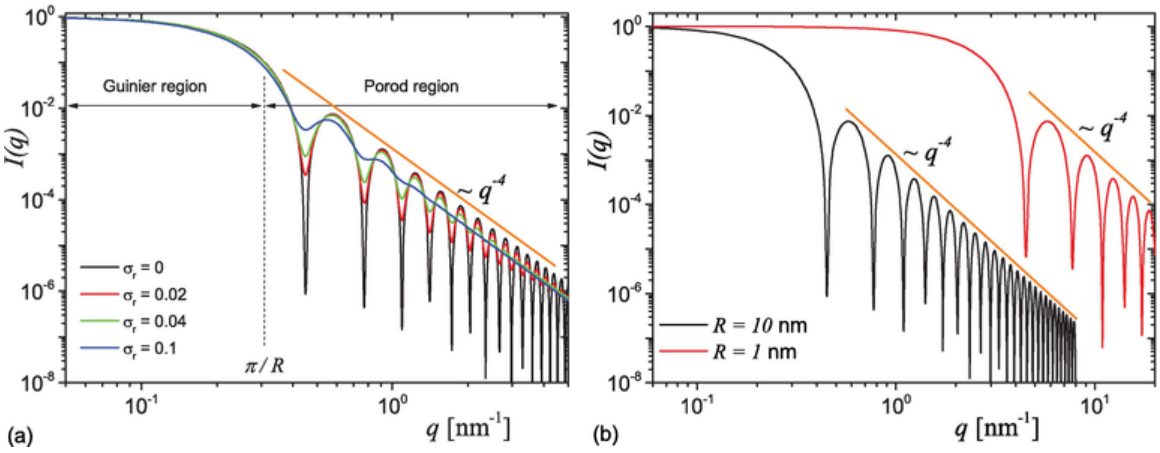

Figure 3.7: X-ray scattering profiles of dilute spheres of a) different polydispersity, and b) different radii. Polydispersity rapidly smears out the sharp features of the sphere form factor, but the critical scale and dimensional information remains. Figure reprinted from Reference [56] under the Creative Commons 4.0 license (https://creativecommons.org/licenses/by/4.0/).

and controlled from an operating computer, which offers access to a wide range of resolutions and q-ranges for measurements, including predetermined WAXS, medium-angle (MAXS,) SAXS, and extremely-small-angle (ESAXS) configurations. The instrument and supplied software automatically perform a large number of corrections and refinements to the data, including elimination of cosmic rays, detector noise, and dark current.

The Ganesha sample stage can support free-standing membranes, powders, sealed paste cells, sealed capillaries, and an environment control chamber called the XenHumGen, which allows in-situ control of temperature and relative humidity in the sample environment. This thesis includes measurements of free-standing membranes, membranes sealed in paste cells, and humidified membranes in the XenHumGen. While no additional postprocessing is necessary for free standing membranes, the Kapton® polymer windows of the XenHumGen are of comparable thickness to most membrane samples and produce a prominent background scattering pattern that must be corrected for via background subtraction. Similarly, the paste cells are sealed with mica windows, which produce both a subtle background scattering profile and intense speckles of scattering from crystalline domains, which must be manually masked out. Sample raw data is included in Appendix A.

The instrument was calibrated against a silver behenate standard powder sample (AgBeh, see Fig. 3.5) before each series of measurements using the XenHumGen or the ambient plate. Paste cell measurements relied on calibrations previously performed by instrument technicians with DABCO samples.

For *in vacuo* measurements, samples were attached to a pinholed sample holder with double-sided tape, and were allowed to equilibrate with the environment for at least one hour prior to measurement. For humidified measurements, samples were allowed to equilibrate

with each environment for two hours, and the longest measurements were performed first. Humidified samples were performed at 25°C. Fully-hydrated samples were equilibrated with bulk water for at least 24 hours, then padded dry with gauze and sealed in paste cells with mica windows and allowed to equilibrate for two hours. WAXS measurements were performed both at the beginning and the end of each experiment and compared to confirm that the cells did not leak during the experiment.

For each series of measurements, WAXS exposures were taken for 600 seconds, MAXS exposures were taken for 7200 seconds when using the XenHumGen humidity controller and 1800 seconds otherwise[5], and SAXS exposures were taken for 3600 seconds. To further increase the signal-to-background ratio, 2-3 layers of membrane were stacked together when measuring with the XenHumGen. Background measurements were performed under identical conditions and for the same exposure times when using paste cells or the XenHumGen.

3.2.4 Fitting X-ray scattering data

There are an extremely large number of physically derived and empirical models for fitting scattering data. Due to the complexity of the WAXS profiles, the simplest models that adequately fit the data were chosen to maximize fit stability. For wide-angle X-ray scattering, the model used consisted of a pseudo-Voigt function corresponding to each visible peak, a single power law to account for the Porod regime, and a constant term to account for incoherent and background scattering. The use of pseudo-Voigt peaks is based on a model proposed in Reference [57] commonly used for estimating the degree of crystallinity of polymer systems [58, 59], with the background term simplified to a single constant term to reduce the number of fit parameters [60], and a Porod term included to extend the fitting through the entire observed profile. The fit function is,

$$I(q) = a_p \cdot q^p + r + \sum_i \left\{ s_i \cdot a_i \cdot \exp\left[-(2 \cdot (q - q_i)/c_i)^2 \cdot \log(2)\right] + \frac{a_i \cdot (1 - s_i)}{[(1 + (2 \cdot ((q - q_i)/c_i)^2)]} \right\}. \tag{3.11}$$

where a_j are the amplitudes, q_j are the peak positions, c_j is the peak full-width-half-max, s_j are shape parameters representing the ratio of intensities of the Gaussian and Lorentzian peak components, p is the Porod exponent, and r is the background term. The fit parameters of primary interest are the peak positions q_i, which correspond to regular spacings in the sample, and the Porod exponent p.

[5]Background scattering from the Kapton® windows produces a large peak in the MAXS regime, so longer exposures were necessary to maximize the signal-to-noise ratio.

Low-q 'knees' were fit via the Correlation Length Model as implemented in Igor Pro by Kline and Hammouda [61, 62],

$$I(q) = a_p\ q^p + r + \frac{a_0}{1 + (q\xi)^m}\ , \tag{3.12}$$

in which p is the Porod exponent, a_j are amplitudes, and ξ is a correlation length. m is an empirical fit parameter that may be associated with polymer-solvent interfaces [63]. It can also be considered a special case of a *broad peak model* [62],

$$I(q) = a_p\ q^p + r + \frac{a_0}{1 + (|q - q_0|\xi)^m}\ , \tag{3.13}$$

with q_0 fixed at zero, corresponding to correlated domains of regular size but irregular distribution. Eq. 3.13 was fit to each low-q feature observed, but did not produce better fits than Eq. 3.12.

A model of the form of Eq. 3.12 with $m = 2$ was first derived by Zimm in 1948 as the Single Contact Approximation for semidilute polymer solutions, in which the obtained correlation length is conventionally assigned to the characteristic spacing between points of entanglement [64]. A more general model of the same form derived from the Ornstein-Zernike equation was reported by Benoit and Benmouna in 1983, which was shown to hold at arbitrary concentrations [65]. While it is common in the literature for m to vary from 2 to account for polymer-solvent interactions [61, 63], fits in this thesis fixed $m = 2$ to reduce the number of fit parameters, as this provided results that varied systematically with hydration without reducing the quality of the fits.

3.3 Classical molecular dynamics

Classical Molecular Dynamics (MD) is a technique in which atoms or multi-atom molecular fragments are simulated via classical mechanics using empirical interaction parameters. While this technique has significant limitations—most obviously, it generally cannot simulate chemical reactions—it is an extremely powerful tool and has revolutionized computational biochemistry and materials chemistry. Classical MD can be broadly divided into atomistic, where the fundamental particles are atoms and monatomic ions, and course-grained, where they are larger molecular fragments.[6] This thesis will focus on atomistic MD.

In atomistic MD, particle interactions are generally categorized as *bonds*, *angles*, *dihedrals*, *nonbonded interactions*, and potentially higher order terms, so the total energy is $E_{\text{total}} = E_{\text{bonds}} + E_{\text{angles}} + E_{\text{dihedrals}} + E_{\text{nonbonded}} + E_{\text{higherorder}}$. A set of interaction equations

[6]There is also united-atom MD, an intermediate approach in which some hydrogen atoms are integrated into larger pseudo-atoms.

and parameters is called a *force field*. There are many force fields with tables of interaction parameters available in the literature; the most popular include AMBER, CHARMM, GROMOS, OPLS, and COMPASS. In the past ten years, several toolsets have been developed for assigning force field parameters automatically from established databases, and even for partially automating the creation of new parameters via interpolation or by automatically performing the relevant quantum chemical calculations. One such tool, LigParGen, was utilized in this work [66].

3.3.1 Molecular Dynamics procedure

Molecular dynamics were performed using the OPLS-AA force field [67], which is widely used for polymerized ionic liquids. The OPLS-AA force field is described by the following equations:

$$\begin{aligned}
E_{\text{bonds } r} &= \sum_{\text{bonds}} K_r (r - r_0)^2 \ , \\
E_{\text{angles } \theta} &= \sum_{\text{angles}} K_\theta (\theta - \theta_0)^2 \ , \\
E_{\text{dihedrals } \phi} &= \sum_{\text{dihedrals}} \sum_{n=0}^{4} \frac{K_{n,\phi}}{2} \left(1 + (-1)^{n+1} \cos(n\phi)\right) \ , \\
E_{\text{nonbonded } i,j} &= \sum_{\text{nonbonded} i>j} \left(4\epsilon \left(\left(\frac{\sigma_{ij}}{r_{ij}} \right)^{12} - \left(\frac{\sigma_{ij}}{r_{ij}} \right)^{6} \right) + \frac{q_i q_j e^2}{4\pi\epsilon_0 r_{ij}} \right) \ ,
\end{aligned} \tag{3.14}$$

where r, θ, ϕ, and r_{ij} describe bond lengths, angles and dihedral angles between consecutive bonds, and nonbonded spacings, respectively. We also included an improper dihedral term, $E_{\text{improper}} = \sum_{\text{impropers } \phi} K_I \left(1 + d\cos(n\phi)\right)$ to enforce planarity in some improper dihedrals.

Parameters were first collected from the literature where available [67, 68, 69]. The LigParGen web server was used to update and fill in missing values [66]. Atomic partial charges and optimized parameters for inter-ring dihedrals were calculated using density functional theory, discussed in Section 3.4. All parameters used are tabulated in Appendix B.

Molecular dynamics simulations were performed via the LAMMPS software package [70]. Input files were generated using the Moltemplate package [71]. Constant-volume (NVT) and constant-pressure (NPT) simulations were performed using a Nosé-Hoover thermostat with a time constant of 100 fs; NPT simulations were performed using a Nosé-Hoover barostat with a time constant of 1000 fs. The molecular dynamics calculations utilized the Cedar multi-user cluster located at Simon Fraser University and maintained by Compute/Calcul Canada. Using the USER-OMP accelerator package, performances of 3 to 6 ns/day with 16 Broadwell CPU cores and 10-20 ns/day with 48 Skylake cores were achieved. As priority

access to the Compute Canada systems was not available, most simulations were performed using a single 48-core Skylake node as these nodes were less congested.

The systems studied in this thesis will not equilibrate in accessible timescales without special attention, due to the large rotational barriers, so a variation of an intensive annealing and compression protocol that is common in the literature was used [72, 73]. Simulation cells were assembled by placing 50 tetramers or octomers and the corresponding counterions and associated water molecules into a 12 x 12 x 12 nm^3 simulation cell using the Packmol package, which randomly places molecules in a cell while avoiding overlap [74].[7] This produced cells with densities of approximately 0.1-0.2 g/cm^3. The cell energies were then minimized using a conjugate-gradient descent algorithm as implemented in LAMMPS.

The cells were first annealed at constant volume at 2000 K to randomize the backbone configurations. To bring the cells to realistic density, they were then subjected to ten annealing-relaxation-compression cycles, in which the cell was annealed for 50 ps at constant volume (NVT) at 1200 K, equilibrated for 100 ps at constant volume at 300K, then compressed or relaxed at constant pressure (NPT) for 50 ps at 300K, with the constant pressure cycles being performed at 100, 1000, 10000, 5000, 1000, 500, 100, 10, and 1 atmospheric pressure respectively [76, 73]. The final NPT cycle was extended to 1 ns to ensure that the density stabilized. After these compression cycles, the cell was finally annealed at 2000 K for 2 ns at constant NVT, then cooled to 1000K in five 100 ps, 200 K steps, then to 300 K in seven 100 ps, 100 K steps. The cell was then equilibrated for 5 ns at standard temperature and pressure to allow final equilibration of the density, then an additional 10 ns at constant volume to reach steady-state dynamics. Finally, samples were taken at NVT for 30 ns, saving a frame every 5 ps. For performance reasons, direct electrostatic interactions were cut off at 0.85 nm, the recommended value for utilizing TIP4P/2005 water [77]; long-range electrostatic interactions were calculated using LAMMPS's particle-particle, particle-mesh solver with target accuracy set to 0.0001. Water and hydroxide geometries were constrained as required via the SHAKE algorithm [77, 78].

Most analysis of the simulation results was performed using the Visual Molecular Dynamics (VMD) package, which includes visualization tools and a package for calculating pair-correlation functions [79]. Cell volumes and densities were taken from LAMMPS thermodynamic reporting.

3.3.2 Calculation of X-ray scattering profiles from simulation results

Total scattering and partial structure factors were calculated from simulation data via the direct method as described by Liu and Paddison [80], which allows the structure factors to be computed efficiently without calculating a Fourier transform. Partial structure factors

[7] In recent work, increasing the number of tetramers to 200 had no significant effect on ion dynamics or short-range order [75].

are defined as the contributions to the structure factor of specific pairs of particles, typically similar or different atomic species. The total scattering, Eq. 3.5, can be written in terms of partial structure factors as

$$I(q) = \sum_{\alpha}^{n} \sum_{\beta}^{n} f_{\alpha}(\vec{q}) f_{\beta}(\vec{q}) S_{\alpha\beta}(\vec{q}) \ , \tag{3.15}$$

where f_α and f_β are the form factors of species α and β respectively, and $S_{\alpha\beta}(\vec{q})$ is the partial structure factor of species α and β,

$$S_{\alpha\beta}(\vec{q}) = \frac{1}{N} \sum_{j}^{N_\alpha} \sum_{l}^{N_\beta} \exp\left(-i \ \vec{q} \ (\vec{r_j} - \vec{r_l})\right) \ . \tag{3.16}$$

In this method, Eq. 3.16 is rewritten as

$$S_{\alpha\beta}(\vec{q}) = \frac{1}{N} \left\langle \left[\sum_{j=1}^{N_\alpha} \cos(\vec{q} \cdot \vec{r_j}) \right] \left[\sum_{l=1}^{N_\beta} \cos(\vec{q} \cdot \vec{r_l}) \right] + \left[\sum_{j=1}^{N_\alpha} \sin(\vec{q} \cdot \vec{r_j}) \right] \left[\sum_{l=1}^{N_\beta} \sin(\vec{q} \cdot \vec{r_l}) \right] \right\rangle \ , \tag{3.17}$$

making use of Euler's formula. This reduces the computational complexity from $O(N^2)$ to $O(N)$ [80] by eliminating the double summation. The partial structure factors can then be analyzed individually or summed to the total X-ray scattering profile.

It is most common for $S_{\alpha\beta}(\vec{q})$ to be calculated either using

$$S_{\alpha\beta}(\vec{q}) = \frac{1}{N} \left\langle \left[\sum_{j=1}^{N_\alpha} \sum_{l=1}^{N_\beta} \frac{\sin(q|\vec{r_j} - \vec{r_l})}{q|\vec{r_j} - \vec{r_l}|} \right] \right\rangle \ , \tag{3.18}$$

which is computationally expensive due to the double summation, or by taking the Fourier transform of the pair-correlation function, which can produce misleading results due to the finite size of the simulation cell.

Calculations of scattering profiles utilized atomic form factors taken from International Tables for Crystallography [81], and were validated against results reported by the Igor Pro package [62], and against experimental results for bulk water shown in Fig. 3.8. For each system, the $\vec{q}$-space was sampled where $\vec{q} = \frac{2\pi}{L}(n_x, n_y, n_z)$, where L is the box dimension and n are integers from 0 to 64. The program is being considered for open-sourcing after documentation and further testing is complete.

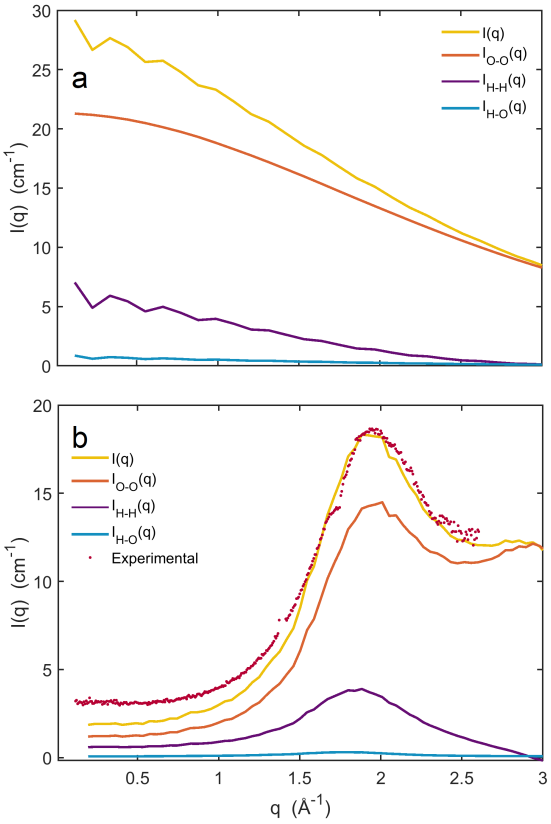

Figure 3.8: Example calculated X-ray scattering profiles of a) a single gas-phase water molecule in a 200 nm^3 cube, and b) 46 nm^3 of bulk water. In (b), the example is compared to an experimental measurement using a paste cell taken while testing the Ganesha 300XL instrument. The discontinuities in the experimental data are caused by manually masking scattering from the mica windows.

3.4 Density functional theory

Density functional theory (DFT) calculations were performed to visualize molecular geometries and identify intramolecular and polymer-anion spacings, as well as to calculate partial charges and force constants for molecular dynamics simulations. DFT is a quantum chemical technique for approximating solutions to the many-electron Schrodinger equation, which is not exactly solvable for systems of more than one electron. This technique has become ubiquitous due to rapid increases in accessible computation power, the development of user-friendly software packages, and consistent validation of predictions against experiments. The premise of the technique is that, as electrons are indistinguishable particles, the ground state energy of a system of electrons in an external potential can be uniquely determined by the electron density; that is, the energy of a system of electrons in an external potential is a unique functional of the electron density ρ, and that such a functional is minimized by the true ground state electron density [82]; these are the Hohenberg-Kohn theorems. This section will provide only a brief overview of the technique, as it is not the focus of this thesis. Interested readers are directed to Reference [82] for a more comprehensive introduction.

The ground state energy $E[\rho]$ can be separated into kinetic, external, and internal terms:

$$E[\rho] = T[\rho] + V_{\text{ext}}[\rho] + V_{\text{int}}[\rho] \ , \tag{3.19}$$

where $T[\rho]$ is the kinetic energy, $V_{\text{ext}}[\rho]$ is the external potential energy, and $V_{\text{int}}[\rho]$ is the internal potential energy. $V_{ext}[\rho]$ can simply be expressed as $V_{ext}[\rho] = \int d\vec{r}\, V_{ext}(\vec{r'})\rho(\vec{r'})$, but the remaining terms are unknown. When considering a molecular system, the electrons are assumed to relax much more rapidly than the nuclei, so electron-nuclear interactions are treated as an external potential. This assumption is the Born-Oppenheimer approximation.

As proposed by Kohn and Sham [83], a noninteracting approximation of $T[\rho]$ can be written as a functional of orbitals ϕ_i as

$$T_S[\rho] = -\frac{\hbar^2}{2m}\sum_i^N \left\langle \phi_i|\nabla^2|\phi_i \right\rangle \ , \tag{3.20}$$

the sum of the individual kinetic energies of each electron. For this system, the electron density function is described as a sum of individual basis functions:

$$\rho(\vec{r}) = \sum_i^N |\phi_i(\vec{r})|^2 \ . \tag{3.21}$$

Similarly, a classical approximation to the internal energy can be made via the Hartree energy:

$$V_H[\rho\vec{r}] = \frac{\hbar^2}{2m}\int d\vec{r_1} d\vec{r_2} \frac{\rho(\vec{r_1})\rho(\vec{r_2})}{|\vec{r_1} - \vec{r_2}|} \ . \tag{3.22}$$

This provides the energy functional in its standard form,

$$E[\rho] = T_S[\rho] + V_{ext}[\rho] + V_H\rho + E_{xc}[\rho] \ , \tag{3.23}$$

where the final term $E_{xc}[\rho] = (T[\rho] - T_S[\rho]) + (V_{int}[\rho] - V_H[\rho])$ contains all of the error introduced by approximating the kinetic and internal energies. If a reasonable approximation to $E_{xc}[\rho]$ can be selected, $E[\rho]$ can be minimized via the variational principle, yielding the ground-state energy and electron density. Many such functionals have been proposed; they are generally classified as local density approximations (LDA), which depend only on the value of ρ at $\vec{r}$, generalized gradient approximations (GGA), which depend on both ρ and $\nabla\rho$, and hybrid functionals, which also incorporate the Hartree-Fock exact exchange energy. Hybrid functionals often achieve strong performance on a wide variety of problems - the Becke 3-parameter Lee-Yang-Parr hybrid functional (B3LYP) [84, 85] is extremely widely used and greatly contributed to the acceptance of DFT by the chemistry community [86].

The ground state energy and electron density distribution can be obtained by solving the Kohn-Sham equations,

$$\left(\frac{\hbar^2}{2m}\nabla^2 + v_{eff}(\vec{r})\right)\phi_i(\vec{r}) = \epsilon_i\phi_i(\vec{r}) \ , \tag{3.24}$$

where v_{eff} is the effective local potential, given by

$$v_{eff}(\vec{r}) = v_{ext}(\vec{r}) + \int d\vec{r'}\frac{\rho(\vec{r'})}{|\vec{r} - \vec{r'}|} + v_{xc}(\vec{r}) \ , \tag{3.25}$$

and v_{xc} is the local exchange and correlation potential,

$$v_{xc}(\vec{r}) = \frac{\delta E_{xc}[\rho(\vec{r})]}{\delta\rho[\vec{r}]} \ . \tag{3.26}$$

As the effective local potentials depend on the density, these equations must be solved iteratively by alternately computing the electron density and single-electron orbitals; in practice this generally converges to a global minimum without issue [87]. In a geometry optimization problem where the relaxed atomic configuration of a molecule is desired, the ground state of the electrons is calculated, then used to calculate forces on the nuclei and update the nuclear geometry; this process is repeated until the forces on the nuclei vanish and the system is in equilibrium.

To make the problem tractable, the single-electron wavefunctions are defined as linear combinations of atomic orbitals (LCAO):

$$\phi(\vec{r}) = \sum_i^M \sum_j^N c_{ij}\chi_{ij}(\vec{r}) \ , \quad \sum_{i,j} c_{ij} = 1 \tag{3.27}$$

where each atom i has N pre-defined basis functions χ_{ij}. A set of basis functions for each atomic species is called a *basis set*. With the advent of modern hybrid functionals such as B3LYP, the size of the basis set is the limiting factor for most calculations. Atomic orbitals defined as the sum of so-called 'primitive Gaussian' functions of the form $Y_{l,m}(\theta, \phi)r^l \exp(\zeta r^2)$ are ubiquitous for molecular calculations. Such orbitals are called contracted Gaussian functions.

Basis functions are commonly divided into 'core,' 'valence,' 'polarization,' and 'diffuse' functions, with a single core function commonly describing all tightly-bound electrons, and generally two or more valence functions describing the valence shell of each atom. Polarization functions allow a basis set to describe covalent bonding and polarization, and diffuse functions, which are highly extended in space, improve the accuracy of electron densities far form the nuclei, and are often necessary to describe anions accurately and model steric effects.

DFT procedure

With the exception of the dihedral energy scans, the DFT calculations in this thesis were performed using the Gaussian 16 package [88] as deployed in the Cedar cluster, maintained by Westgrid and Compute/Calcul Canada. The B3LYP functional was used for each calculation [84, 85]. Calculations of oligomer geometry utilized the def2-TZVP basis set [89, 90], with additional diffuse functions added to the anions [91]. Optimized dihedral force parameters were calculated by optimizing the geometry of a molecular fragment and performing a relaxed dihedral scan, which is a technique in which individual dihedral force parameters in the force field are fit to a potential energy curve generated by iteratively rotating the dihedral and relaxing the remaining coordinates via density functional theory.

The dihedral scans were performed using the B3LYP/6-31++G(d,p) level of theory for consistency with previous work [92, 27, 28]. A relaxed dihedral scan of the inter-benzimidazolium bond performed using the 6-311++G(d,p) basis set produced a slightly different profile at significant computational expense; as close agreement between the MD and DFT profiles could not be achieved with either DFT-calculated profile for that dihedral, and as dihedral scans performed using 6-31G(d), 6-31++G(d,p), and 6-311++G(d,p) produced indistinguishable energy profiles for the mesitylene-benzimidazolium dihedral, target energy profiles calculated using the 6-31++G(d,p) basis sets were deemed sufficient. DFT-calculated, unoptimized, and optimized dihedral energy profiles are included in Appendix B.

The relaxed dihedral scans were performed using the Gaussian 09D [93] package. Partial charges were calculated using the CHELPG method as implemented in Gaussian 16, in which atomic partial charges are fit to a grid of electrostatic potentials calculated from the electron density [94]. Visualizations of DFT calculations were created using the Gaussview 5 package [95]. Initial geometries were produced using the Avogadro package [96].

3.5 Other calculations

Cluster analyses were conducted on molecular dynamics results to analyze the distribution of water and ions and to test for percolation. Clusters were defined as sets of counter-ions and water molecules each separated by less than 3.5 Å from their closest neighbor in the cluster. The length of 3.5Å was selected as it corresponds to the first-order peak in the iodide-water pair correlation function. (Lowering this spacing for systems with smaller anions did not affect the results.) These calculations were performed in VMD using the tool command language (TCL) console. Pore volumes were calculated from molecular dynamics simulations using the Caver package, and free volumes were calculated by subtracting the estimated volume occupied by water and cations from the pore volumes [97]. Ion volumes were estimated from conventional ionic volumes at 25° C [98], and the estimated volume of a water molecule was set to 30.0 $Å^3$, the well-known molecular volume of bulk water, which can be easily calculated by dividing the molecular mass of water, 18.0 g/N_A, by the density of water, 0.995 g/cm^3,

$$V_{\mathrm{mol}} = \frac{m_{\mathrm{mol}}}{\rho} \ . \tag{3.28}$$

Ion dynamics were analyzed using the Diffusion Coefficient Tool package [99]; mean squared displacements MSD were computed with interval steps of 100 ps. Diffusion coefficients were calculated via

$$D = \frac{1}{6}\frac{d\ MSD(\tau)}{d\tau} \ ; \tag{3.29}$$

$\frac{d\ MSD(\tau)}{d\tau}$ were obtained by fitting a straight line to the high-τ regime of $MSD(\tau)$ vs τ, defined as $\tau > 7.5$ ns.

Ion conductivities σ_i were estimated using the Nernst-Einstein equation,

$$\sigma_i = D c_i {Z_i}^2 \frac{F^2}{RT} \ , \tag{3.30}$$

where F is Faraday's constant, R is the ideal gas constant, Z is the ionic charge, and c is the counter-ion concentration. While this relationship is only thermodynamically valid in the infinitely dilute limit, the primary deviation from ideal behavior at high concentrations is reduced ion conductivity due to correlations between the motion of oppositely-charged ions, which will not occur in our systems as only the negatively-charged counter-ions are mobile.

Chapter 4

The Nanostructure of HMT-PMBI

4.1 Introduction

HMT−PMBI is a fully aromatic hydrocarbon polycation with a simple, scalable synthetic route, hydroxide ion conductivity comparable to high-performance CEM materials, and excellent mechanical and chemical stability [38, 100]. HMT−PMBI has been referred to as a potential benchmark AEM material and has been featured widely in studies of alkaline electrochemical systems [39, 49, 100, 101, 102, 103]. A corporation licensing patents related to HMT−PMBI development has received over $10 million USD in startup funding. This chapter will discuss how a comprehensive picture of HMT−PMBI nanostructure at various hydration levels was produced through a combination of X-ray scattering experiments and molecular dynamics calculations.

The majority of this section is based on References [27] and [28], which built upon preliminary work reported in Reference [52] by performing many additional measurements, including SAXS of fully-hydrated samples in paste cells and samples under controlled humidity and temperature. Improved simulations were performed, utilizing revised force field parameters, a much more sophisticated cell preparation and annealing protocol, and longer simulation durations. All work described in this chapter was performed by Eric Schibli, except where noted.

4.2 X-ray scattering experiments and interpretation

The X-ray scattering profiles of HMT−PMBI(Cl^-), (Br^-), and (I^-) at various RH are shown in Fig. 4.1. Each profile shows a strong upturn at low-q characteristic of ion-containing polymers, conventionally attributed to density inhomogeneities [104], and three distinct peaks at scattering wavevectors greater than 0.1 $Å^{-1}$: a small peak at approximately 0.4 $Å^{-1}$, a large peak at approximately 1.2 $Å^{-1}$, and a peak of variable intensity at approximately 1.8 $Å^{-1}$. In addition, a fourth peak at approximately 0.8 $Å^{-1}$ is clearly visible in

the chloride-form samples, but is not discernible in the bromide- and iodide-form samples. These will be referred to as Peaks 1 through 4 in order of increasing q.

Using Eq. 3.9, these peaks correspond to characteristic spacings of approximately 19, 9.5, 6.4, and 4.2 Å; these length scales and associated spacings will be referred to as d_1 through d_4. In all samples, Peak 4 increases in intensity with humidity, while the relative intensity of the other peaks remain approximately constant. Peak 1 appears more prominently in the bromide-form sample, which is likely due to a lower level of q-independent and low-q scattering. The noise visible near Peak 1 is caused by the subtraction of large amounts of background scattering from the environment control chamber, which has Kapton® windows, as discussed in Chapter 3.

The low- and mid-q scattering is remarkably simple and does not change with hydration, which provides no evidence of phase separation at controlled humidity; when plotted in absolute units, the profiles at RH= 30% – 100% are indistinguishable at $q < 0.1$ Å^{-1}, while the RH=0% profile shows slightly greater amplitude, likely due to free volume offering improved contrast. While Peak 1 appears at a length scale that has been assigned to short-range intermolecular order in similar materials [105], it does not shift in position or intensity with hydration as would be expected for such a feature.

Peak 4 increases in intensity with humidity in all samples and is more intense in samples with larger counter-anions, especially at lower humidity. This strongly suggests that Peak 4 reflects anion-anion, anion-water, and/or anion-polymer backbone spacing. However, it seems likely that there is also a contribution from either water-anion, water-backbone, or water-water spacing as well, as the intensity of the peak increases with hydration. While the primary oxygen-oxygen spacing in bulk water is approximately 3 Å, the most intense peak in the WAXS spectra of water is at 2 Å, consistent with Peak 4 [106].[1]

To confirm the origins of these features, a gas-phase DFT geometry optimization of an HMT–PMBI(I^-) tetramer was performed at the B3LYP/def2-TZVP level of theory. The optimal geometry is shown in Fig. 4.2, revealing a monomer length of approximately 20 Å, consistent with the spacing measured for d_1. The mean spacing between the iodide ions and the nearest non-hydrogen backbone atom is 3.8 Å, about 10% below d_4; this lower distance is not surprising considering that the DFT calculation was performed *in vacuo* at zero temperature, allowing the counter-ions to settle into the lowest potential energy position.

The X-ray scattering profiles of HMT–PMBI(Cl^-) and (I^-) at various degrees of functionalization, in ambient conditions, and after soaking in water, are shown in Fig. 4.3. In ambient conditions, Peak 4 increases in intensity significantly with degree of functionalization in both HMT–PMBI(Cl^-) and (I^-), providing further evidence that it is primarily a anion-backbone spacing. It also shows higher intensity in the fully-hydrated samples, rel-

[1] Also see Fig. 3.8 for a WAXS measurement of water highlighting the large contribution of oxygen-oxygen spacings to a peak at 2 Å^{-1}.

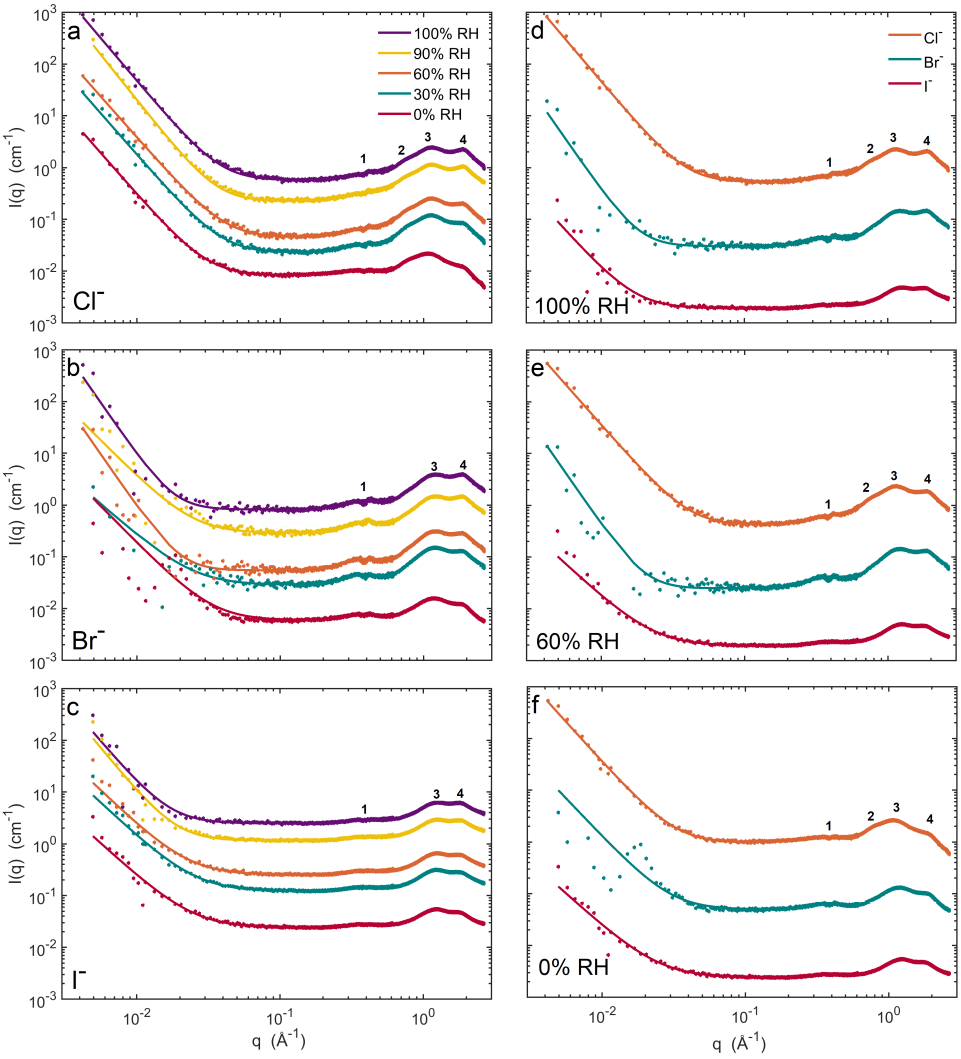

Figure 4.1: X-ray scattering profiles of 85% df HMT−PMBI at (a,b,c) various relative humidities in in a) chloride, b) bromide, and c) iodide form, and (d,e,f) with various counterions at d) 100%, e) 60%, and f) 0% RH. The profiles of the three samples are similar, except that Peak 2 is only visible in HMT−PMBI(Cl^-). As the humidity is increased, the intensity of Peak 4 increases while the intensity of Peak 1 decreases slightly in each sample [28], especially in Cl^- form. The profiles are vertically offset for clarity.

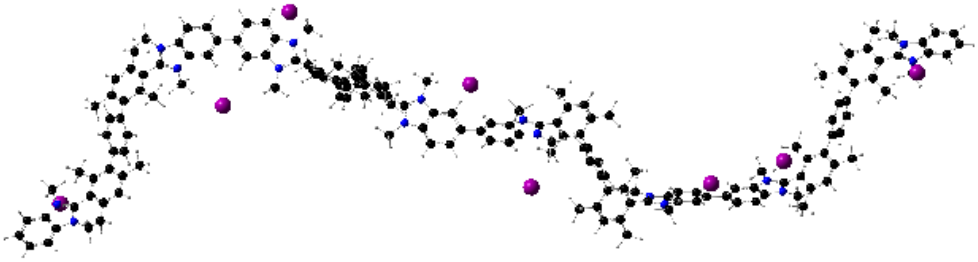

Figure 4.2: An HMT–PMBI(I^-) tetramer optimized at the B3LYP/def2-TZVP level of theory. Diffuse basis functions – basis functions with an very long 'tail' that improve the modeling accuracy of steric effects at the expense of significant computational cost, were added to the iodide ions. See Sect. 3.4 for further details.

ative to ambient conditions, similar to what is seen in Fig. 4.1, suggesting there is also a contribution from anion-water and water-water spacing.

There is also a subtle low-q shoulder visible in the fully-hydrated HMT–PMBI(Cl^-) samples. This characteristic length scale will be referred to as the correlation length ξ. Fitting Eq. 3.12 to the feature returns a correlation length of 3.9 ± 1.8 Å for 97.5% df and 4.9 ± 0.4 Å for 89.7% df HMT–PMBI(Cl^-). This feature will be discussed in more detail in Chapters 5 and 7.

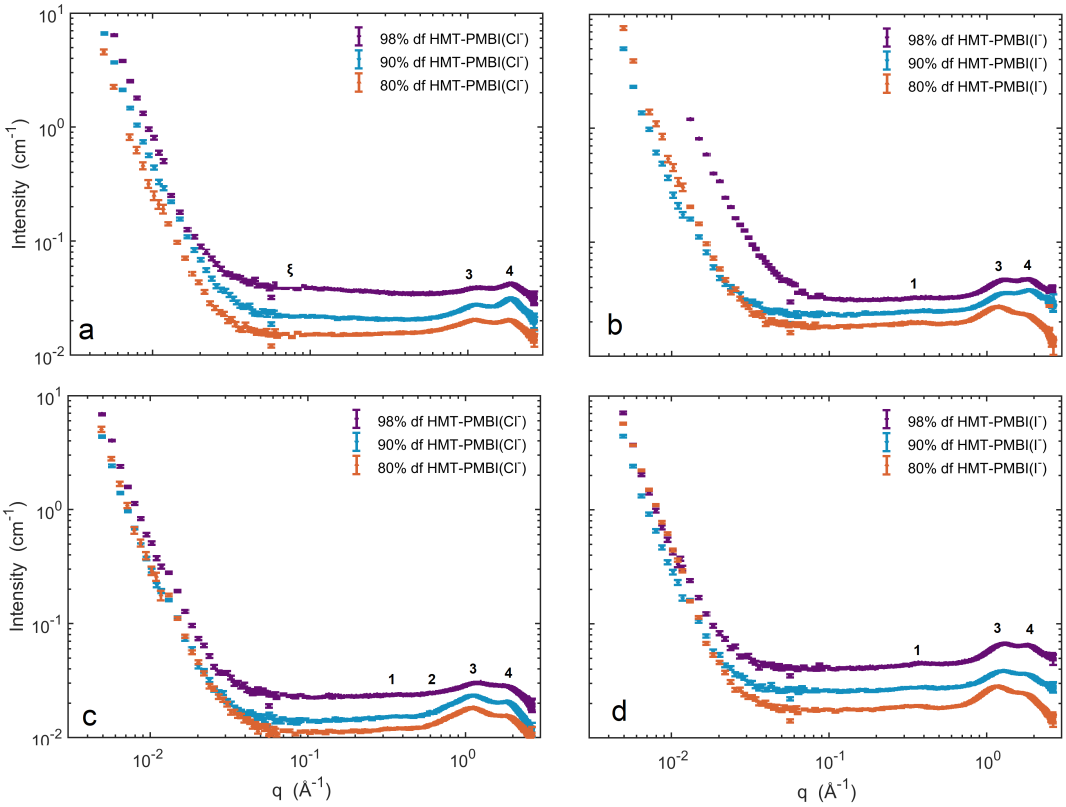

Figure 4.3: X-ray scattering profiles of HMT−PMBI in (a, c) chloride and (b, d) iodide form in (a, b) wet and (c, d) ambient humidity [27]. The profiles are vertically offset for clarity. A fit of Eq. 3.12 to the data from $q = 0.03 - -0.3$ Å^{-1} for the 98% and 90% df data is shown in (a) as a solid curve, but is difficult to distinguish from the markers.

4.3 Molecular dynamics simulation results

The combination of molecular dynamics and X-ray scattering has received significant attention in the literature recently, particularly when reporting the nanostructure of novel materials [25, 27, 107]. These techniques are highly complementary as their combination allows direct validation of the computational results by comparing experimental X-ray scattering profiles to those calculated from the simulations, and provides insight into the origin of features in the X-ray scattering profiles.

4.3.1 Chloride-form simulations at a range of hydrations

A series of molecular dynamics simulations of fifty 87.5% df HMT−PMBI tetramers, 300 chloride ions, and the corresponding water molecules were performed as described in detail in Chapter 3. In Fig. 4.4, two different direct representations of equilibrium structures taken from the sampled frames of the simulations are shown to highlight different features of the nanostructure. In Fig. 4.4a, polymer backbones are shown as estimated electron density

isosurfaces, while chloride ions are shown as spheres and water molecules, as three spheres. These images show that HMT−PMBI(Cl^-) displays a sponge-like nanostructure, with a bulky polymer matrix that does not appear to pack efficiently. At $\lambda = 2$ to $\lambda = 4$, hydration conditions of two and four water molecules per counter-ion respectively, discrete clusters of water and ions occupy the space between the polymer chains. At higher levels of hydration, $\lambda = 8$ and above, the water-rich phase is more substantial, a trend which continues as the water content is increased to $\lambda = 12$ and 16. However, the polymer backbones do not appear to aggregate and there is no clear morphological change when moving from $\lambda = 8$ to $\lambda = 16$; the polymer backbones simply appear to be forced apart as the cell swells to accommodate the additional water.

To visualize the water/anion phase in greater detail, in Fig. 4.4b, each anion and water molecule is shown as a sphere, colour-coded by connectivity.[2] The simulation cell at $\lambda = 2$ shows many discrete clusters of 1-3 chloride ions and associated water molecules. At $\lambda = 4$, most of the clusters are connected by a thin, percolating network of water molecules. At $\lambda = 8$ and higher, nearly all of the water and ions are part of a continuous, percolating phase and there are no longer distinct clusters, and as in Fig. 4.4, the water/anion phase merely grows from $\lambda = 8$ to $\lambda = 16$.

[2]Particles were defined as connected if they were within 3.5 Å. This cutoff length is based on the iodide-water pair-correlation function; reducing it slightly for simulations of smaller anions did not impact the results significantly.

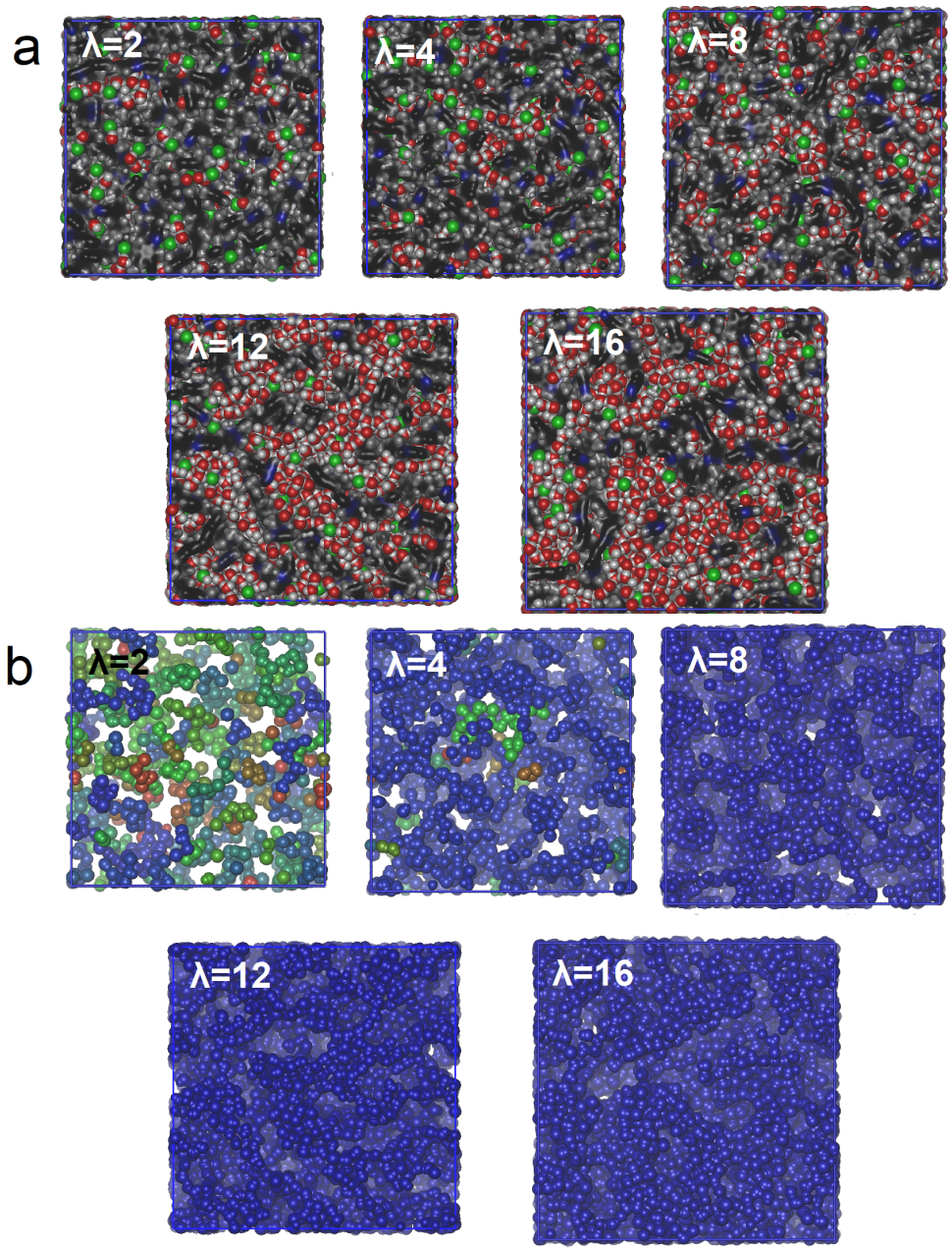

Figure 4.4: Snapshots taken from simulations of 87.5% df HMT−PMBI(Cl^-) at $\lambda = 2$ (box side length $L = 59.9$ Å), $\lambda = 4$ ($L = 61.0$ Å), $\lambda = 8$ ($L = 63.6$ Å), $\lambda = 12$ ($L = 66.2$ Å), and $\lambda = 16$ ($L = 68.8$ Å). In (a), polymer backbones are shown as isosurfaces calculated by Quicksurf, while the halides and oxygen and hydrogen in water molecules are shown as spheres. Carbon, nitrogen, oxygen, hydrogen, and chloride atoms are colored black, blue, red, grey, and green, respectively. In (b), water and chloride ions are shown as spheres, colored by cluster where a cluster is defined by particles continuously separated by fewer than 3.5 Å from each other. At $\lambda = 2$, there are many individual clusters of 1-3 ions and 2-6 waters, while $\lambda = 4$ both small clusters and a large percolating domain are present. By $\lambda = 8$, nearly all ions and water molecules are connected to the percolating domain. The images are to scale; their sizes reflect the increasing cell volume with hydration.

4.3.2 Total scattering and partial structure factors

A comparison between experimental X-ray scattering profiles and profiles calculated from simulation results via Eq. 3.5 for HMT−PMBI(Cl^-) at various hydration levels is shown in Fig. 4.5. There is excellent agreement in the peak positions and in the shape of the profiles. In both the experimentally observed and simulated profiles, Peaks 1, 2, and 3 have greater amplitude in the 0% RH and $\lambda = 2$ profiles, while the relative intensity of Peak 4 increases with hydration. Further discussion of the total X-ray scattering profiles can be found in Section 3.2.1.

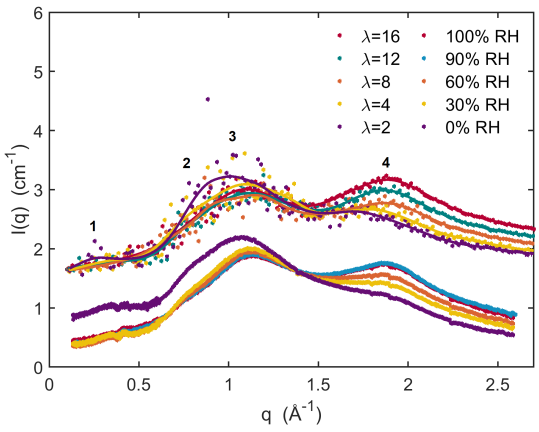

Figure 4.5: Comparisons between experimental (below) and simulated (above) X-ray scattering profiles of 85% df HMT−PMBI in chloride form. The simulated profiles have been vertically offset from the experimental profiles by a constant value for clarity. There is good agreement between the experimental and simulated X-ray scattering profiles, including quantitative agreement in the peak positions. The solid lines through the simulated profiles are multispline fits without physical meaning, and are only intended to aid the eyes. Matching colours correspond to similar states of hydration [49].

Visual inspection of the molecular dynamics results shown in Fig. 4.4 show changes in morphology with hydration at low and intermediate degrees of hydration, and changes in characteristic length scales with hydration at all levels of hydration. These are not apparent in either the experimental or simulated X-ray scattering data in Fig. 4.5. This can be explained by considering calculated partial structure factors, which are plotted in Fig. 4.6. Fig. 4.6a shows hydrophobic-hydrophobic interactions between backbones, Fig. 4.6b shows hydrophilic-hydrophilic interactions between water molecules and chloride ions, and Fig. 4.6c shows hydrophobic-hydrophilic interactions between the backbones and the water and anion particles.

Each partial structure factor shows a very prominent feature below $q = 1.0$ range, which increase in absolute intensity and move to lower q with increasing water content. This indicates that the length scales corresponding to spacings between backbones and water-rich domains increasing with hydration as seen in Fig. 4.4. However, this evolu-

tion is entirely invisible in the total scattering; the peaks hydrophobic-hydrophobic and hydrophilic-hydrophilic partial structure factors are positive, while that in the hydrophilic-hydrophobic partial structure factor is correspondingly negative, and the combination of these partial structure factors to form the total structure factor results in a complete cancellation of the terms as seen in Fig. 4.5. This is a result of the low contrast between the polymer backbones and the water-rich phase; as they have similar electron densities, they cannot be discriminated between via X-ray scattering.

4.3.3 Pair-correlation functions

Pair-correlation functions were plotted to quantify short-range particle distributions in real space. To ensure convergence, pair-correlation functions were calculated for each 5 ns of the sampling period, and were found to be indistinguishable. Correlations between water and chloride ions in simulations of HMT–PMBI(Cl^-) at various levels of hydration are shown in Fig. 4.7a; as hydration is increased, the relative intensity of the nearest-neighbor peak at 3.25 Å decreases, while a second-nearest-neighbor peak appears at 4.5 Å at $\lambda = 4$ and increases in intensity. Similarly, a third-nearest-neighbor peak appears at 7.0 Å at $\lambda = 8$, which also increases in intensity with hydration. The appearance and strengthening of these higher-order peaks reflect the formation of a second and third solvation shell about the anions. At $\lambda = 2$ and $\lambda = 4$ a small peak is visible at 6.0 Å, which corresponds to the linear strands of water connecting chloride ions visible in Fig. 4.4a and b. A similar trend is shown for correlations between water molecules in Fig. 4.7b; the nearest-neighbor peak at 3 Å decreases and the next-nearest-neighbor peak at 4.5Å increases in intensity with hydration.

Additional pair-correlation functions from simulations of HMT–PMBI(Cl^-) are shown in Fig. 4.8. Fig. 4.8a highlights correlations between the chloride ions. The first peak appears at approximately 5.4 Å at $\lambda = 2$. This peak shifts to lower r and increases in intensity with hydration, saturating at 5.1 Å at $\lambda = 8$. At low hydrations, this spacing reflects spacings between chloride ions separated by a single layer of water molecules; the shift to lower r reflects a larger number of water molecules available to connect each ion pair, drawing the ions closer together. The second peak is at 7.7 Å and increases in intensity slightly with hydration. This peak corresponds to spacing between ions connected by a layer two water molecules thick. There is also a large, broad peak at approximately 10 Å at $\lambda = 2$, which shifts to 11 Å at $\lambda = 4$ and is not present at higher levels of hydration. This peak corresponds to spacings between chloride ions associated with backbone cations; as hydration levels increase, ions are drawn away from the backbones and into the water-rich phase.

Correlations between chloride ions and backbone atoms are plotted in Fig. 4.8b. Each profile shows a doublet peak at approximately 4.0 Å and 5.0 Å, and a broader peak, which shifts continuously from approximately 6.2Å at $\lambda = 2$ to 7.6 Å at $\lambda = 16$. The doublet peak corresponds to chloride ions associated with backbone cations; the 4.0 Å and 5.0 Å peaks

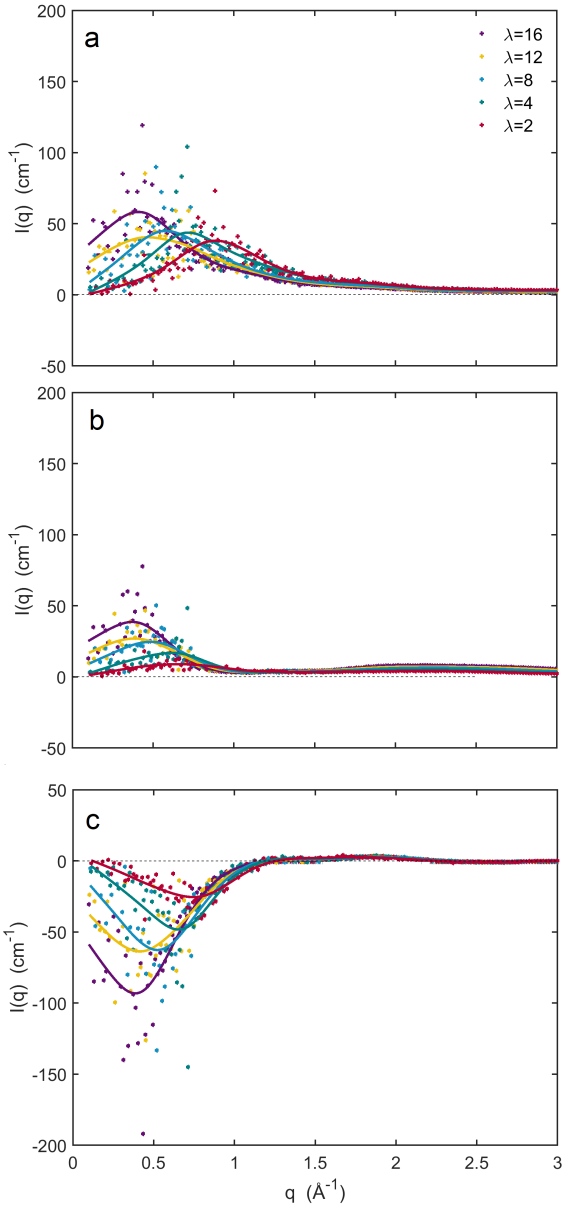

Figure 4.6: Partial scattering factors calculated from simulations of HMT−PMBI(Cl^-), considering (a) structure within the polymer phase, (b) structure within the water/anion phase, and (c) polymer-water/anion structure. The solid curves are multispline fits without physical meaning and are intended only as guides to the eyes.

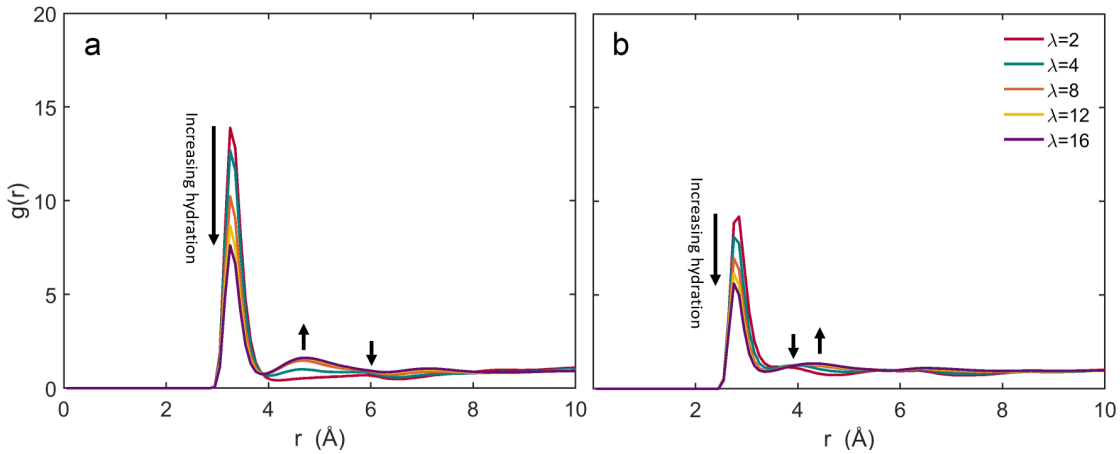

Figure 4.7: Pair-correlation functions for a) oxygen-chloride, and b) oxygen-oxygen pairs. In a), the first-order peak systematically decreases while the second-order peak systematically increases with increasing hydration, showing the formation of a larger solvation shell with hydration.

reflect spacings between the chloride ion and the sterically-protecting methyl group and closest aromatic atom respectively. The broader peak at higher r corresponds to chloride ions that are not associated with the backbone cations, and the shift to higher r reflects increasing solvation drawing ions farther from the backbone. Correlations between backbone atoms are plotted in Fig. 4.8c. Correlations between particles in the same molecule have been excluded. The profiles begin approaching 1 at 4 Å, with the rate of increase decreasing slowly with hydration.

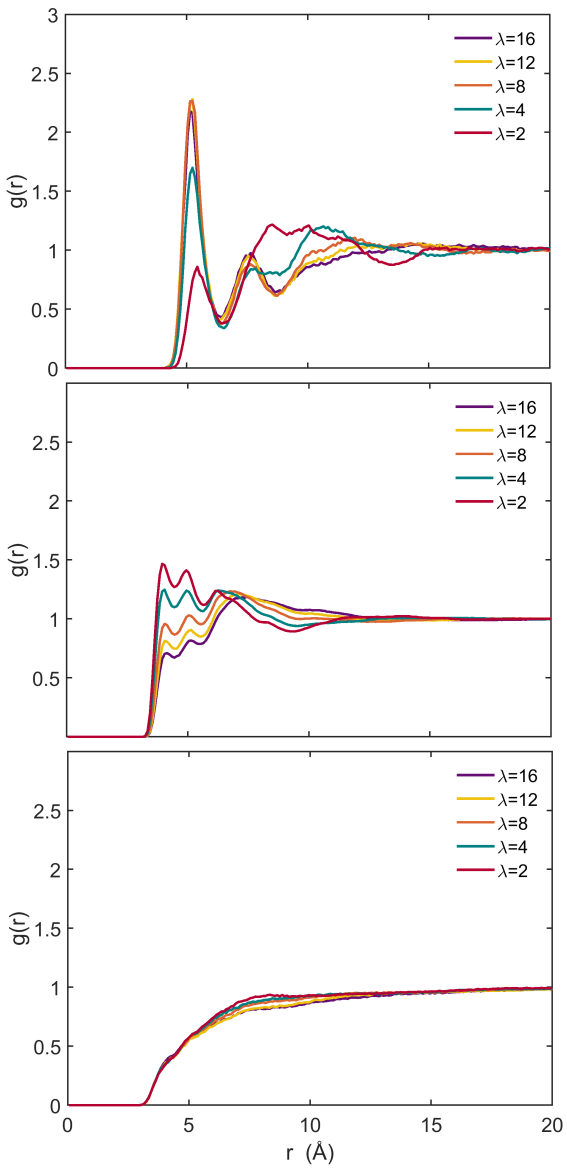

Figure 4.8: Pair-correlation functions calculated from MD simulations of HMT−PMBI(Cl^-) at various hydrations for a) chloride-chloride, b) chloride-backbone, and c) backbone-backbone pairs. "Backbone" particles include carbon and nitrogen atoms.

4.3.4 Simulations with various counter-ions

The simulations of HMT−PMBI were also performed with various counter-ions to determine their impact on the nanostructure. The counter-ions considered include iodide, bromide, chloride, fluoride, and hydroxide, in order of increasing hydrophilicity. Although HMT−PMBI(OH−) and HMT−PMBI(F−) samples were not available for experimental study, simulations in these forms were performed to observe the effects of extremely hydrophilic anions. Hydroxide-form membranes are of the greatest technological interest.

Figure 4.9 shows the distribution of water and anions in simulations performed at $\lambda = 4$ with various counter-ions. The particles are colour-coded by cluster, where each cluster is defined as a continuous group of particles, each separated by fewer than 3.5 Å. This cutoff distance was taken from the centre of the primary peak in the iodide-water pair-correlation function; increasing it to encompass the entire peak or reducing it to correspond to the peak position for each anions did not impact the results significantly. Samples containing the less hydrophilic counter-ions, iodide, bromide, and chloride, show an extensive, interconnecting water/anion phase and several smaller clusters. The fluoride and hydroxide-form simulations contain over 100 individual clusters and no percolating phase at this low level of hydration; this is a result of the very hydrophilic anions overpowering the water-water interactions. The simulation of HMT-PMBI(I^-) also shows six isolated iodide ions and seven ions associated with only a single water molecule—5% of the counter-ions in total—highlighting the weak iodide-water interaction. Figure 4.10 shows similar results for simulations performed at $\lambda = 8$; at this and higher levels of hydration, a fully-percolating phase is present and includes each counter-ion.

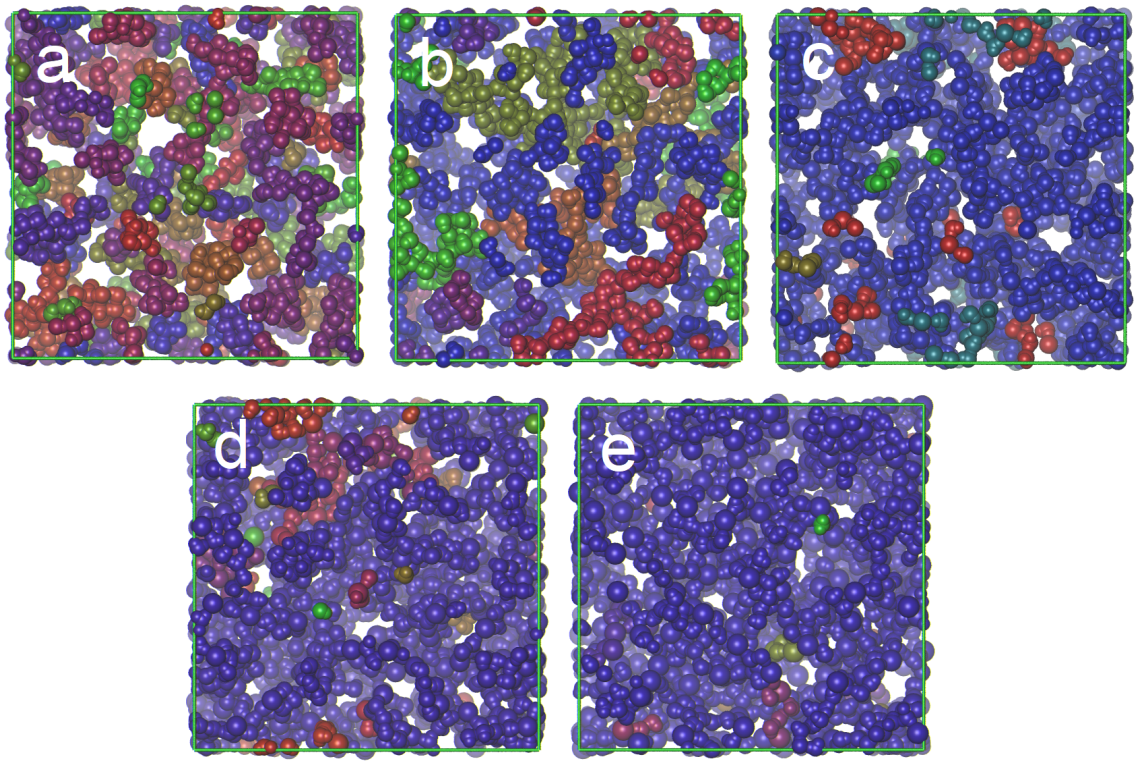

Figure 4.9: Anions and water molecules from simulations of 87.5% df HMT−PMBI at $\lambda = 4$ in the (a) hydroxide, (b) fluoride, (c) chloride, (d) bromide, and (e) iodide form. The particles are coloured by cluster as in Fig. 4.4; particles of different colors are not connected within the water-anion phase. The more hydrophilic anions, fluoride and hydroxide, draw water into discrete clusters, while the chloride, bromide, and iodide forms show both a percolating phase and several small clusters. The iodide form also shows six isolated ions and seven ions paired with only a single water molecule, representing 5% of the counter-ions in total.

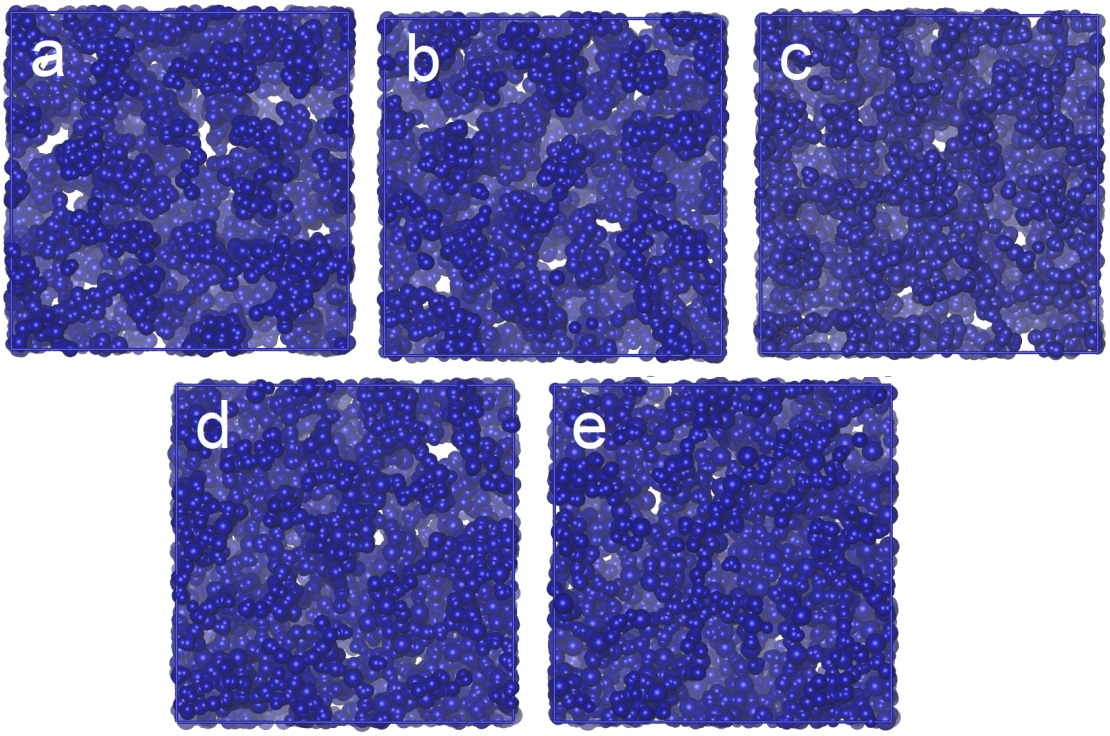

Figure 4.10: Anions and water molecules from simulations of 87.5% df HMT−PMBI at $\lambda = 8$ in the (a) hydroxide, (b) fluoride, (c) chloride, (d) bromide, and (e) iodide form at $\lambda = 8$. Each water molecule and halide ion are connected in a percolating phase.

These results are confirmed by the analysis of pair-correlation functions from the simulation results. Pair-correlation functions for anion-anion, anion-polymer, and polymer-polymer pairs are shown in Fig. 4.11. Anion-anion correlations are shown in Fig. 4.11a and d. The smaller and more hydrophilic counter-ions show a dramatically stronger first order peak. This confirms that they are very tightly clustered, as seen in Figs. 4.9 and 4.10. Anion-backbone correlations are shown in Fig. 4.11b and e; similarly, the first-order doublet peak, which corresponds to spacing between an anion and associated cation, is much weaker for F^- and OH^- at both $\lambda = 4$ and $\lambda = 8$, confirming that the stronger anion-water interactions draw the anions away from the polymer backbone. Fig. 4.11c and f, which show polymer-polymer correlations, confirms that the counter-ions do not affect the backbone spacings significantly as polymer-polymer spacings do not change significantly with anions or hydration.

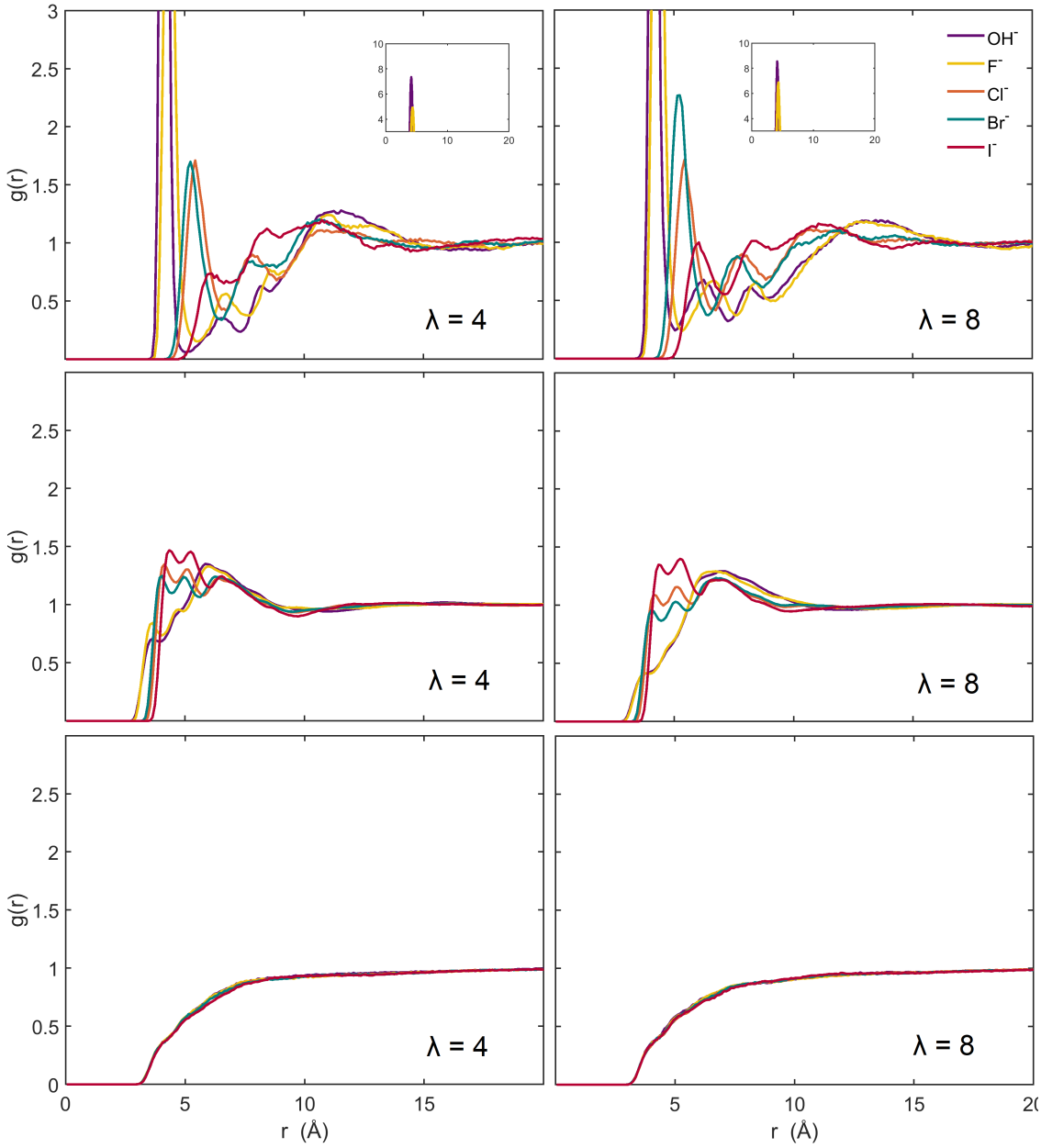

Figure 4.11: Pair-correlation functions calculated from simulations of HMT−PMBI at (a,b,c) $\lambda = 4$ and (d,e,f) $\lambda = 8$ for (a,d) anion-anion, (b,e) anion-backbone, and (c,f) backbone-backbone pairs. In a), the first-order peak decreases dramatically in intensity and shifts to higher r, from 4.5 Å to 5.5 Å, as anion size increases from OH^- to I^-. There is an additional large, broad peak at approximately 11Å, which increases in intensity and shifts to slightly higher r with decreasing anion size. The results shown in d) are similar, but the first order peaks show greater intensity, especially for larger anions, and the higher-r peak shifts to higher r more rapidly. (b) and (e) show a doublet peak at approximately 4 and 5 Å, corresponding to spacing between the anion and a methyl group and backbone carbon for anions associated with a cation. This feature decreases in intensity with decreasing anion size, especially F^- and OH^-, and is weaker at $\lambda = 8$. (c) and (f) show correlations between atoms in different polymer backbones, which smoothly approach 1 for all counter-ions and at both hydration levels.

Fig. 4.12 presents pair-correlation functions calculated for ion-water and water-water pairs from simulations performed with various counter-ions at $\lambda = 4$ and $\lambda = 8$. Correlations between anions and water molecules are shown in Figs. 4.12a and c; the first order peak shifts to higher r and decreases in intensity significantly with increasing anions size at both degrees of hydration, confirming that water molecules are more tightly bound to the smaller and more hydrophilic anions. Correlations between water molecules are shown in Fig. 4.12b and d. At $\lambda = 4$ the first-order peak weakens with decreasing anion size, showing the increasing strength of the anion-water interaction relative to the water-water interaction. This change is much less significant at $\lambda = 8$ as less of the water is tightly bound to the anions. The higher-r peaks are more prominent in Fig. 4.12c and d, showing a higher population for the second solvation shell with each counter-ion at $\lambda = 8$.

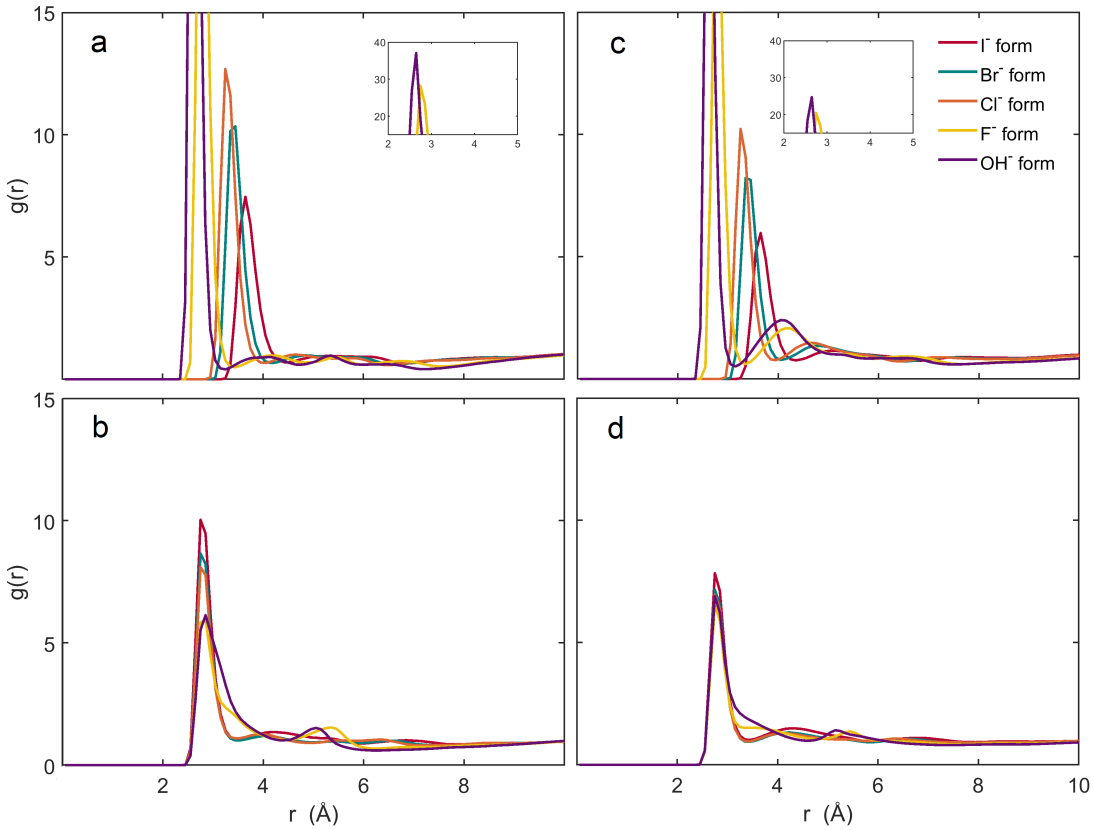

Figure 4.12: Pair-correlation functions calculated from MD simulations of HMT–PMBI with various counter-ions at (a,b) $\lambda = 4$ and (c,d) $\lambda = 8$ for (a,c) oxygen-anion and (b,d) oxygen-oxygen pairs. In (a) and (b), the first-order peak systematically decreases in intensity and moves to higher r with increasing anion size, showing the decreasing strength of the anion-water interaction. In (b) and (d), the first-order peak weakens with decreasing anion size, showing the increasing strength of the anion-water interaction relative to the water-water interaction. Higher-order peaks are significantly more prominent in (c) and (d), especially for the F^- and OH^- forms, showing the formation of a second solvation shell.

4.4 Conclusions

X-ray scattering measurements of HMT–PMBI show three peaks, which appear at approximately 0.4 $Å^{-1}$, 1.2 $Å^{-1}$, and 1.8 $Å^{-1}$ in each sample. These peaks shift in intensity with hydration and counter-ion, but do not shift in position significantly with hydration and do not provide insight into the sample morphologies. A fourth peak is present at 0.8 $Å^{-1}$ in chloride-form samples, but similarly does not evolve significantly with hydration. An additional feature, a weak knee that appears only in the wettest samples, corresponds to a correlation length of 4 to 5 Å. The WAXS peaks correspond to spacings of approximately 19, 9.5, 6.4, and 4.2 Å; the largest spacing is the monomer length, and the remainder are inter-molecular and inter-atomic spacings.

While the results of the X-ray scattering measurements are inconclusive on their own, they validate the molecular dynamics simulations, which show the morphology is simple and sponge-like. The rigid polymer backbones are unable to pack tightly and do not aggregate or crystallize. Water first occupies the available volume around these backbones, forming a percolating domain at levels of hydration as low as $\lambda = 4$, in samples with less hydrophilic anions, Cl–, Br–, and I–. More hydrophilic anions are dissociated from the cations in the polymer backbones, even at low levels of hydration, in which they trap the available water in a tightly-bound solvation shell that interferes with percolation. As the level of hydration is increased, the water/anion domain swells, forcing polymer backbones apart; at $\lambda = 8$, the morphology is similar for each anion, showing a large, interpenetrating domain connecting each anion and water molecule.

This evolution cannot be observed via X-ray scattering due to an apparent lack of contrast between the polymer and the water/anion phase; as seen in the partial scattering factors, Peaks 2 and 3 in the observable X-ray scattering profiles are only the small difference remaining after significant cancellation of the polymer-polymer and water/anion-water/anion scattering by the polymer-water/anion partial scattering factor. This surviving difference does not represent the true inter-domain spacing. This insight highlights the utility of direct comparisons between X-ray scattering results and scattering profiles calculated from simulation data, as the X-ray scattering was able to validate the molecular dynamics, while the molecular dynamics simulations were necessary to confidently interpret the X-ray scattering results.

Chapter 5

The Nanostructure of Imidazolium-Based Ionenes

5.1 Introduction

After HMT−PMBI was reported in 2014, work continued to synthesize new sterically-protected ionenes with higher anion conductivities and improved chemical stabilities. The most significant improvement was the replacement of the benzimidazolium functional groups with imidazolium functional groups, which enables significantly greater hydroxide stability due to the greater transition state energy of the ring-opening degradation pathway and the more complete steric protection enabled by the smaller cation size [41, 43]. Additionally, varying the functionalization groups – referred to as *R-groups* – rather than the degree of functionalization allows modulation of water uptakes with less significant impact on IEC and further improvements to OH^- stability; where HMT−PMBI is synthesized only with methylated benzimidazolium cations, TMP−PMPI and DMP−PMPI are synthesized with methyl-, ethyl-, propyl-, and butylated cations, with the larger aklylation groups corresponding to lower water uptakes, lower IECs, and even greater chemical stability. Selected material properties of both series were printed in Section 2.3.

This chapter will discuss the structures of TMP−PMPI and DMP−PMPI, two series of hydrocarbon ionenes incorporating both of these improvements. Chemical structures of these materials are shown in Fig. 5.1. TMP−PMPI consists of symmetric monomers containing two penta-substituted imidazolium cations bonded 'head-to-head' across a durene unit. DMP−PMPI consists of asymmetric penta-substituted imidazolium monomers. These samples were investigated in a similar manner to HMT−PMBI to determine whether the varied backbone structure impacted the nanostructure.

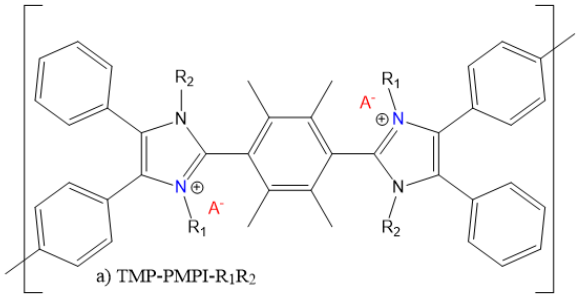

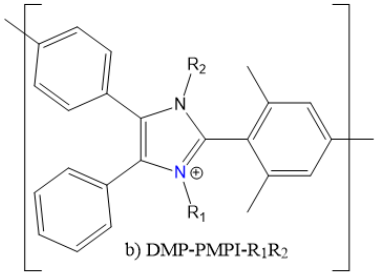

$R_1, R_2 =$

M	E	P	B
		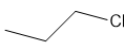	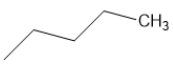

Figure 5.1: The chemical structures of (a) TMP−PMPI (b) DMP−PMPI, and (c) the four R-fragments used.

5.2 X-ray scattering results

X-ray scattering experiments were performed on TMP−PMPI(Cl^-) samples at controlled humidity to observe the swelling behavior. These measurements were conducted in collaboration with Aidan A. Wright, and are also reported in Reference [108]. The results are first are shown with linear axes in Fig. 5.3 to emphasize the WAXS regime. Figs. 5.3(a) and (b) compare TMP−PMPI−MM(Cl^-) and TMP−PMPI−BB(Cl^-) at different levels of humidity, while Figs. 5.3(c) and (d) compare each form at 100% and 0% RH. As in HMT−PMBI(Cl^-), four peaks are visible in most samples, located at approximately 0.8 $Å^{-1}$, 1.3 $Å^{-1}$, 1.5 $Å^{-1}$, and 2.2 $Å^{-1}$, which we refer to as Peaks 1 through 4, respectively. Peak 1, corresponding to a spacing of approximately 9.5 Å, likely corresponds to the common repeated spacing along the monomer, similar to Peak 1 in HMT-PMBI. The remaining peaks, 2 through 4, correspond to interatomic spacings of approximately 5.9, 5.1, and 3.5 Å respectively.

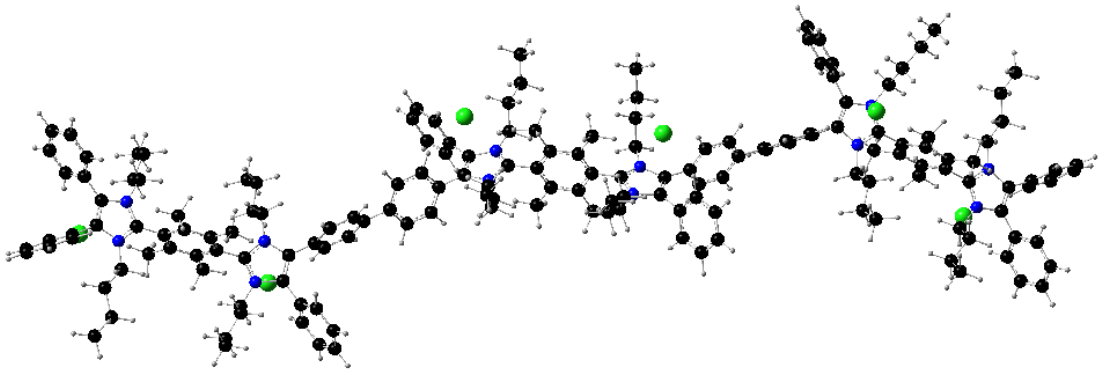

Figure 5.2: An TMP–PMPI–BB(Cl^-) trimer optimized at the B3LYP/def2-TZVP level of theory, with diffuse basis functions added to the chloride ions. The central chloride ions are separated by 10.0 Å, while the central imidazolium rings are separated by approximately 7.9 Å. The chloride ion-backbone spacings are approximately 3.4 Å.

The WAXS profiles evolve only subtly with humidity. In TMP–PMPI–MM(Cl^-) (Fig. 5.3a) Peak 2 weakens slightly and Peak 4 strengthens slightly with increased humidity; in TMP–PMPI–BB(Cl^-) (Fig. 5.3b), both Peak 1 and Peak 3 weakens with increased humidity, while Peak 4 strengthens slightly.

The entire WAXS profiles decrease in intensity significantly with increasing aklkylation unit length. By far, the most obvious change is the significant decrease in intensity of Peak 2 with increased alkylation unit length, resulting in the feature not being visible in TMP–PMPI–BB(Cl^-) profiles. The position and intensity of Peak 1 is similar in TMP-PMPI-MM, -EE, and -PP, but shifts approximately 0.1 Å lower to $q = 0.7$ Å in TMP–PMPI–BB(Cl^-). with increasing akylation unit length.

Chloride-form X-ray scattering results are also plotted in Fig. 5.4 with logarithmic axes to emphasize the low- and mid-q regimes. A mid-q shoulder is present in each sample. This feature is not visible at 0% RH, but increases in intensity with RH, growing to dominate the scattering profiles at higher relative humidities. This behavior is dramatically different from what was observed in HMT–PMBI(Cl^-), in which a similar, but much more subtle, feature was present only after soaking in water. To extract length scales, Eq. 3.12 was fit to these features. The resulting correlation lengths ξ are shown in Table 5.1.

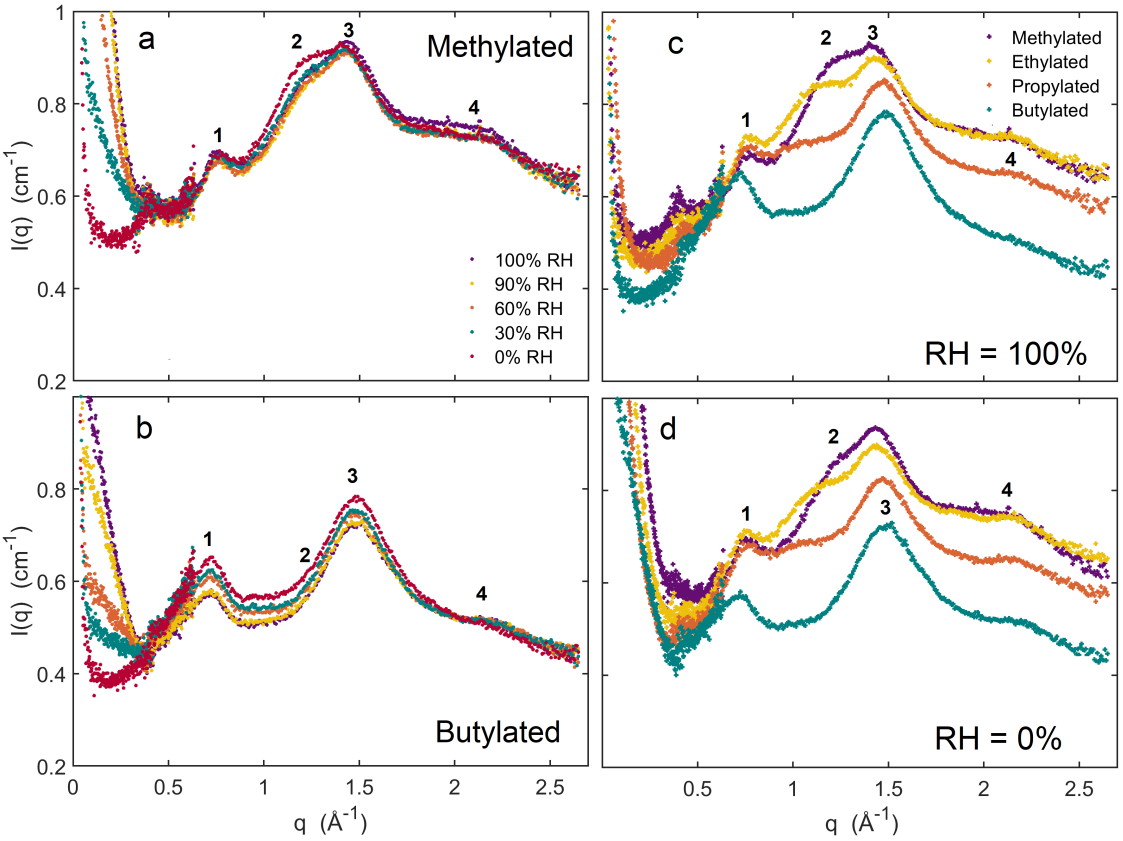

Figure 5.3: X-ray scattering profiles of TMP−PMPI(Cl^-), (a) methylalted at various RH, (b) butylated at various RH, (c) with various funcationalizations at 100% RH, and (d) with various functionalization at 0% RH, at 25° C. The intensity of Peak 2 in (a) and of Peak 1 in (b) decrease with increasing relative humidity. The intensity of the entire WAXS profiles, but especially Peak 2, decrease with increasing aklylation unit length in (c) and (d). The spikes in noise at approximately 0.4 $Å^{-1}$ are caused by the Kapton® windows of the humidity chamber. To emphasize the evolution of the WAXS profiles with hydration and aklylation group, the results are presented without vertical offsets.

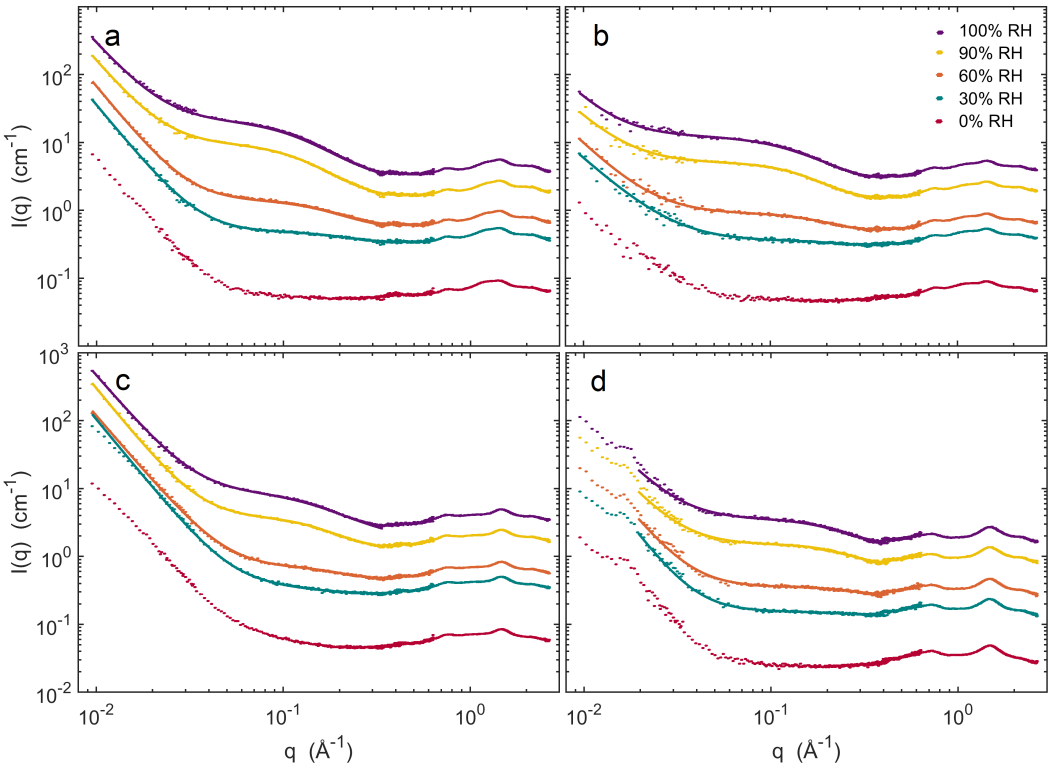

Figure 5.4: X-ray scattering profiles of TMP-PMPI a) $-$MM(Cl^-), b) $-$EE(Cl^-), c) $-$PP(Cl^-), and d) $-$BB(Cl^-) at 25° C at various RH. In each sample, a MAXS shoulder increases in intensity with increasing humidity, but the WAXS profiles do not change visibly with humidity. The low-q bump in the TMP$-$PMPI$-$BB(Cl^-) profile is not isotropic in the 2D data, and is believed to be an artifact caused by a reflection from a crack in the sample. The solid curves are fits of Eq. 3.12 to the data. Correlation lengths determined by the fits are plotted in Fig. 5.7 and tabulated in Table 5.1.

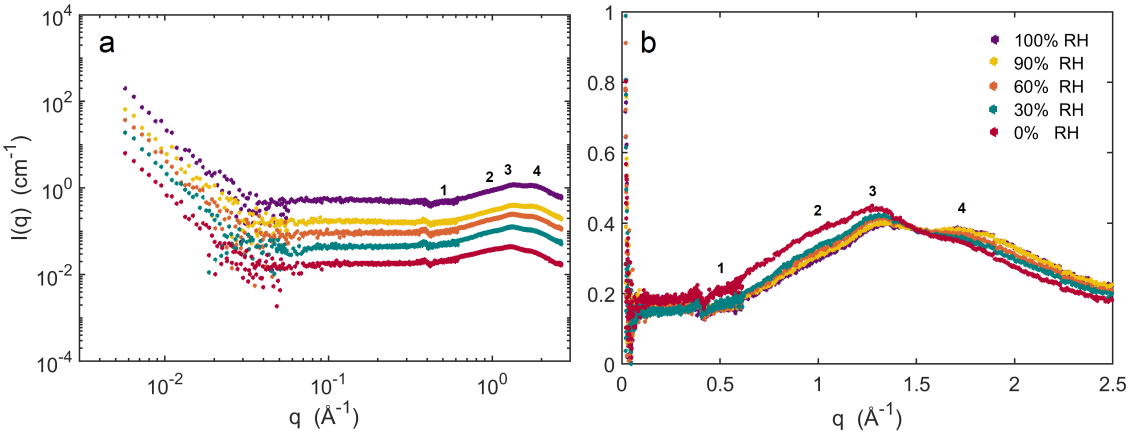

Figure 5.5: X-ray scattering profile of DMP–PMPI–MM(Cl^-) at various RH, a) logarithmic, and b) linear axis. Curves in a) have been vertically offset for clarity.

Measurements of a DMP–PMPI–MM(Cl^-) sample at controlled humidity are shown in Fig. 5.5. Changes to the profile with humidity are subtle; as with HMT–PMBI and TMP–PMPI, we refer to the three visible peaks as Peak 2, 3, and 4 due to their similar shape and location. As in HMT–PMBI(Cl^-) and TMP–PMPI–MM(Cl^-), Peaks 2 and 3 weakens in intensity with humidity, and Peak 4 strengthens in intensity with humidity. Both peaks appear to shift to slightly higher q with increasing humidity: Peak 3 shifts from 1.29 Å^{-1} at 0% RH to 1.37 Å^{-1} at 100% RH, while Peak 4 shifts from 1.60 to 1.78 Å^{-1}.

DMP–PMPI–MM(Cl^-), –EE(Cl^-), and –PP(Cl^-) were measured *in vacuo* and fully hydrated. These measurements are shown in Fig. 5.6. *In vacuo,* (Fig. 5.6a), the profiles are similar to those of DMP–PMPI–MM(Cl^-) at controlled humidity. As in the case of TMP–PMPI, Peak 3 weaken and shifts to lower q with increasing alkylation unit length. The DMP–PMPI–MM(Cl^-) profile is similar to the measurements in Fig. 5.5(a) at low humidity. The DMP–PMPI–EE(Cl^-) profile contains three clear peaks located at approximately 0.92, 1.29, and 1.67 Å^{-1}, while the DMP–PMPI–PP(Cl^-) profile contains two clear peaks at approximately 0.81 and 1.52 Å^{-1}. There are no interesting features in the MAXS regime; the mid- and low-q behavior consists entirely of a smooth transition from flat background to a $q^{-3.6}$ power law.

The WAXS profiles with full hydration (5.6b) are obscured by a very large, broad peak at 2.0Å^{-1}, characteristic of bulk water,[1] which likely desorbed from the membrane surface during the experiment. While it is unclear why this would occur only in DMP–PMPI, repeating the measurement resulted in only moderately different intensities of the 2.0 Å^{-1} peak. In contrast with TMP–PMPI, only the methylated sample shows a visible feature in the MAXS regime. Fitting Eq. 3.12 to the data indicates a correlation length of 5.4 Å.

[1]See Fig. 3.8b for an example.

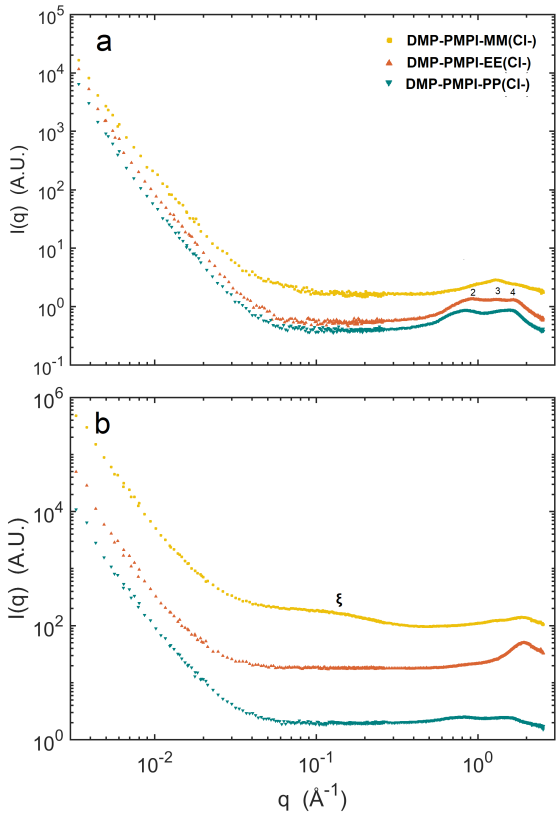

Figure 5.6: X-ray scattering profiles of DMP – PMPI(Cl^-) a) *in vacuo*, and b) fully hydrated, with different alklylation units. The data has been offset for clarity.

Table 5.1: Correlation lengths obtained by fitting Eq. 3.12 to X-ray scattering data. Values are given in Å and range from approximately 4 Å to 10 Å.

Sample	IEC (mequ/g)	WU (%)	ξ, 100% RH	ξ, Wet
97.5% dm HMT–PMBI(Cl^-)	2.96	60.4	Not present	3.9 ± 1.8
89.7% dm HMT–PMBI(Cl^-)	2.41	46.1	Not present	4.9 ± 0.4
80.3% dm HMT–PMBI(Cl^-)	1.92	29.9	Not present	Not present
TMP–PMPI–MM(Cl^-)	2.86	48.2 ± 1.3	9.86 ± 0.05	Not measured
TMP–PMPI–EE(Cl^-)	2.65	28.1 ± 1.6	7.9 ± 0.3	Not measured
TMP–PMPI–PP(Cl^-)	2.46	22.3 ± 1.3	6.5 ± 0.2	Not measured
TMP–PMPI–BB(Cl^-)	2.30	12 ± 2	3.79 ± 0.11	Not measured
DMP–PMPI–MM(Cl^-)	2.58	32.6 ± 4.3	Not present	6.49 ± 0.06
DMP–PMPI–EE(Cl^-)	2.41	26.9 ± 3.3	Not measured	Not present
DMP–PMPI–PP(Cl^-)	2.26	Not measured	Not measured	Not present

5.2.1 The mid-q feature

The HMT-PMBI, TMP-PMPI, and DMP-PMPI series of polymers each show a mid-q knee under certain wet conditions and/or high IEC, but the strength of the feature and the conditions under which it appears vary significantly. Correlation lengths ξ were extracted from measurements under 100% RH and/or fully hydrated conditions by fitting Eq. 3.12 to the data. Results are tabulated in Table 5.1 for each sample; values range from 3.79 ± 0.11 for TMP–PMPI–BB(Cl^-) to 9.86 ± 0.05 for TMP–PMPI–BB(Cl^-). In previous work, Eq. 3.12 was found to produce better fits to this feature in measurements of TMP–PMPI than peak- or fractal-based models [108].

In HMT–PMBI(Cl^-), this feature is only visible at 97.5% and 89.7% df, and only when fully hydrated. The values of ξ are equal within parameter uncertainty (3.9 ± 1.8 and 4.9 ± 0.4 Å), but the feature is more prominent at the high degree of functionalization.[2] The feature is also visible in DMP–PMPI–MM(Cl^-) with a somewhat higher length scale (6.49 ± 0.06 Å), despite the intermediate IEC value and lower reported water uptake.

However, for the TMP–PMPI samples, the feature is clearly visible for each material at each nonzero humidity, and at 100% RH, the length scales range from significantly greater than those for DMP–PMPI–MM(Cl_1^-) (9.86 ± 0.05) for TMP–PMPI–MM(Cl^-) to significantly lower than those observed for 89.7% dm HMT–PMPI(Cl^-) (3.79 ± 0.11 Å). For each series, the feature appears more intensely and with larger ξ values for higher-IEC samples, but does not seem to vary systematically with IEC between series. It is also unclear why the feature is visible at such a wide range of humidities in the TMP–PMPI samples. The values of ξ obtained from fitting the corresponding correlation lengths are plotted in

[2] See Fig. 4.3a

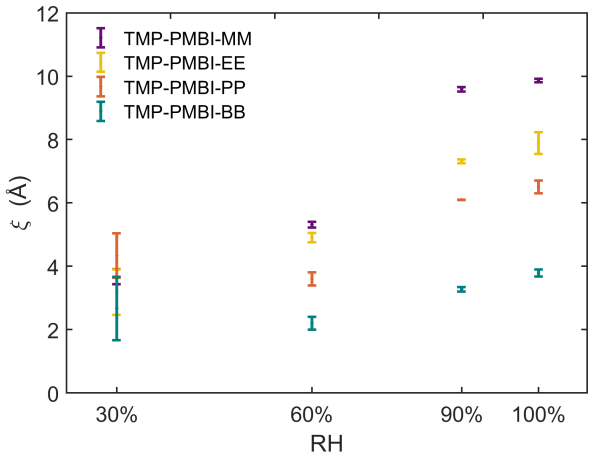

Figure 5.7: Correlation lengths obtained by fitting Eq. 3.12 to the X-ray scattering profiles of TMP – PMPI samples measured at various RH. The data and fits corresponding to these values are plotted in Fig. 5.4.

Fig. 5.7; ξ increases monotonically with relative humidity, and is larger in samples with shorter alkyl units (and correspondingly, higher IEC and WU).

5.3 Molecular dynamics results

Molecular dynamics simulations of fifty TMP–PMPI–MM(Cl^-) and TMP–PMPI–BB(Cl^-) tetramers, and fifty DMP–PMPI–MM(Cl^-) and DMP–PMPI–BB(Cl^-) octomers, including the corresponding 400 chloride ions and water molecules, were also performed as described in detail in Chapter 3. Snapshots highlighting the distribution of water and anions for each system at $\lambda = 4$ are shown in Fig. 5.8. The three methylated systems, 87.5% dm HMT–PMBI(Cl^-), TMP–PMPI–MM(Cl^-), and DMP–PMPI–MM(Cl^-), are shown as Fig. 5.8a, b, and c, respectively. TMP–PMPI–MM(Cl^-) shows the highest level of percolation, as 98.3% of the water and anions are part of the interpenetrating phase.[3] This value is closely followed by DMP–PMPI–MM(Cl^-) with 97.0%, then HMT–PMBI(Cl^-) with 91.3%, again in decreasing order of IEC. The butylated samples, TMP–PMPI–BB(Cl^-) and DMP–PMPI–BB(Cl^-), are shown in Fig. 5.8c and Fig. 5.8d. These systems are substantially different; TMP–PMPI–BB(Cl^-) shows a percolating phase containing just over half of the particles (52.6%), while DMP–PMPI–BB does not, and consists of dozens of individual clusters containing anywhere from 1 to 75 particles.

The methylated samples show a much greater degree of percolation, with over 90% of the water and ions belonging to the percolating phase. In the TMP–PMPI–BB(Cl^-) simulation, approximately half of the water and anions are part of the percolating phase, and in the DMP–PMPI–BB(Cl^-) simulation, there is no percolation. Similar snapshots of the simulations performed at $\lambda = 8$ are shown in Fig. 5.9. At this level of hydration, all waters and anions are part of the percolating phase, and each simulation appears visually similar. Snapshots of the water/ion phase at $\lambda = 12$ and $\lambda = 16$ are shown in Appendix C.

[3]As introduced in Chapter 4, water and anions are defined as part of a cluster if they are within 3.5 Å of a cluster member.

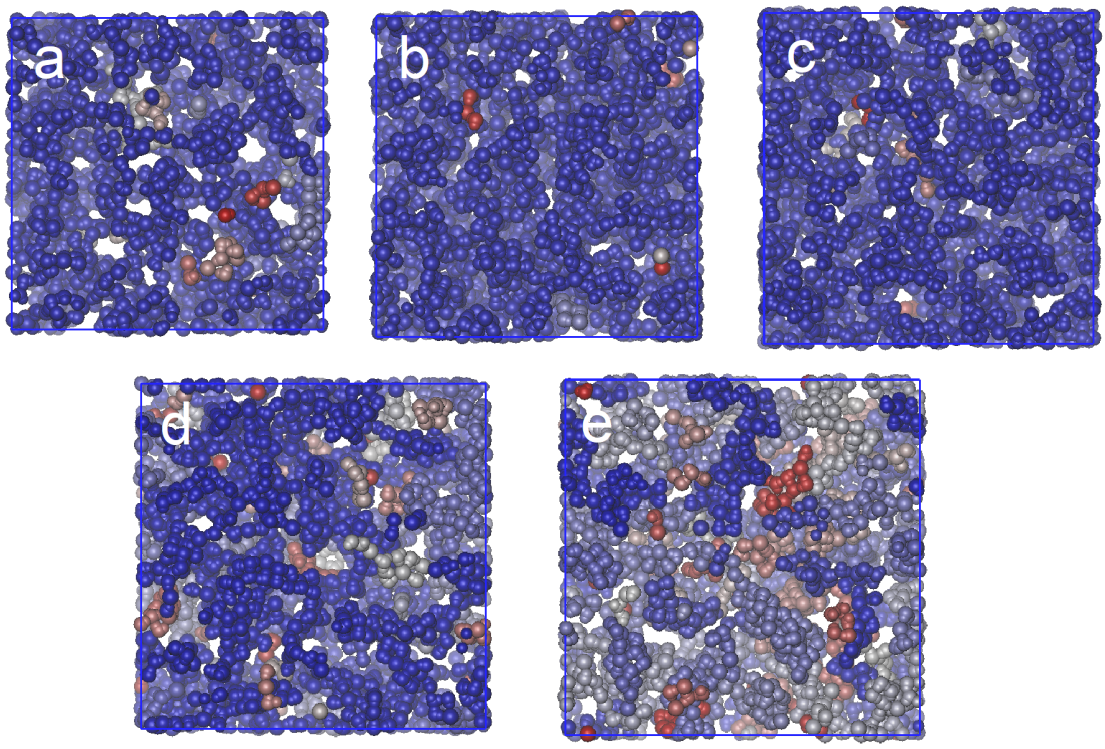

Figure 5.8: Snapshots from molecular dynamics simulations of (a) 87.5 % dm HMT–PMBI(Cl^-), (b) TMP–PMPI–MM(Cl^-),(c) DMP–PMPI–MM(Cl^-), (d) TMP–PMPI–BB(Cl^-), and (e) DMP–PMPI–BB(Cl^-) at $\lambda = 4$, color-coded by cluster. The images are to scale and accurately reflect the relative size of each system. At this low level of hydration, TMP–PMPI–MM(Cl^-) shows the highest level of percolation, with 98.3% of the particles belonging to the largest interpenetrating cluster, followed by DMP–PMPI–MM(Cl^-) (97.0%), HMT–PMBI(Cl^-) (91.3%), and TMP–PMPI–BB(Cl^-) (52.6%). DMP–PMPI–BB does not show percolation and consists of many individual clusters containing up to 75 particles. The images are too scale, and reflect the larger size of the butylated systems.

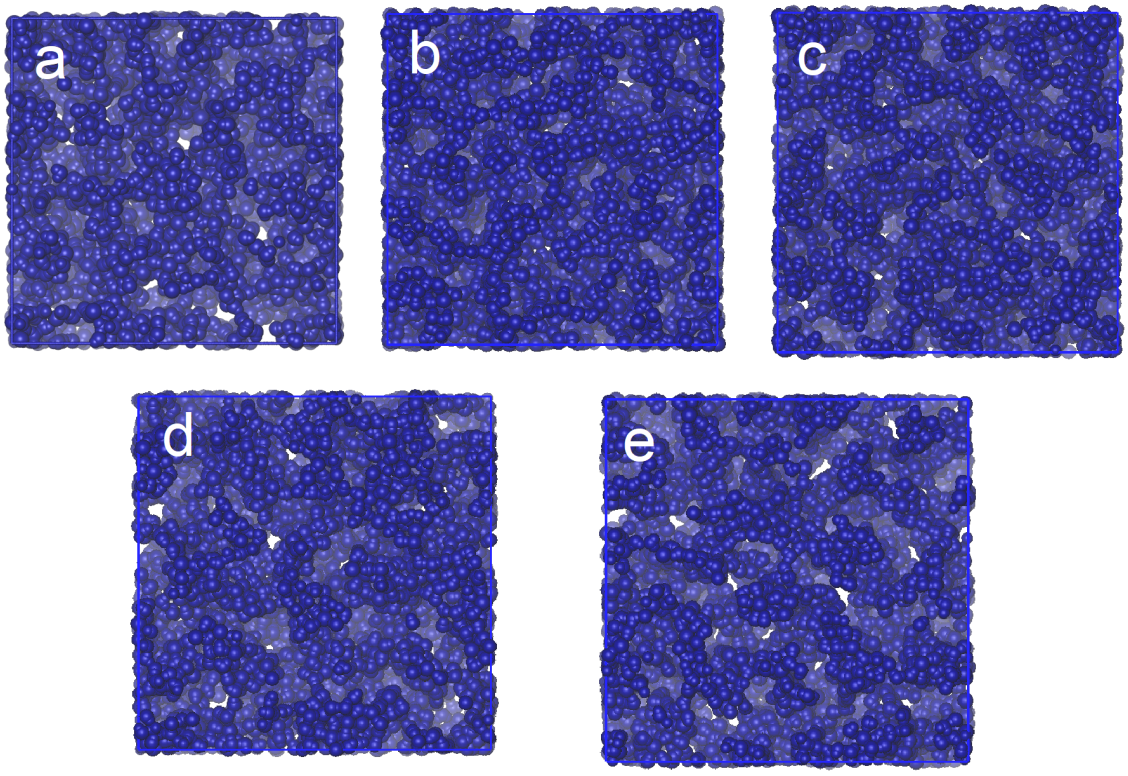

Figure 5.9: Snapshots from molecular dynamics simulations of (a) 87.5 % dm HMT−PMBI(Cl^-), (b) TMP−PMPI−MM(Cl^-),(c) DMP−PMPI−MM(Cl^-), (d) TMP−PMPI−BB(Cl^-), and (e) DMP−PMPI−BB(Cl^-) at $\lambda = 8$, color-coded by cluster. In each system, every water and anion is part of the percolating network. The images are too scale, and reflect the larger size of the butylated systems.

Total scattering and partial structure factors calculated from the simulations of HMT−PMBI(Cl^-), TMP−PMPI−MM(Cl^-), and TMP−PMPI−BB(Cl^-) at $\lambda = 8$ are plotted in Fig. 5.10. As seen in Chapter 4, strong peaks are visible for each system in the polymer-polymer (Fig. 5.10b) and water-water (Fig. 5.10c) partial structure factors at $q = 0.5\text{Å}^{-1}$, but these peaks are canceled by a corresponding negative peak in the polymer-water partial structure factor (Fig. 5.10d), confirming a lack of contrast between the polymer backbones and the water/anion domain. These peaks are much sharper in TMP−PMPI−MM(Cl^-) and TMP−PMPI−BB(Cl^-) than HMT−PMBI(Cl^-), suggesting that the water/anion phase may be slighter better separated.

Peaks 1 and 3 in the TMP−PMPI−BB(Cl^-) scattering profile are clearly defined in the polymer-polymer partial structure factor. While Peaks 2 and 3 are not clearly resolved in the total scattering for TMP−PMPI−MM(Cl^-), inspection of the partial structure factors suggest that they originate from polymer-polymer spacings, as scattering intensity in the water-water and polymer-water profiles is minimal at the relevant q-range. For each system, partial structure factors at $q >= 2$ Å^{-1} are nearly indistinguishable. Additional plots are included in Appendix C; for each system, trends with hydration are similar to those shown for HMT−PMBI(Cl^-) shown in Chapter 4.

Selected pair-correlation functions calculated from the simulations are shown in Fig. 5.11. Each profile is qualitatively similar for each system. Fig. 5.11a shows polymer-anion correlations at $\lambda = 8$, which are strongest at short range for TMP−PMPI−MM(Cl^-) and DMP−PMPI−MM(Cl^-), followed by HMT−PMBI(Cl^-), DMP−PMPI−BB(Cl^-), then TMP−PMPI−BB(Cl^-), respectively. This shows that the chloride ions are most closely associated with the polymer backbones in the methylated imidazolium systems, followed by HMT−PMBI and the butylated imidazolium systems. Fig. 5.11b shows backbone-backbone correlations, also at $\lambda = 8$. Each profile shows a similar distance of closest approach of 3.2 Å and approaches 1 at high r. However, HMT−PMBI approaches 1 the most quickly, followed by DMP-PMPI-MM, TMP-PMPI-MM, DMP-PMPI-BB, and TMP-PMPI-BB respectively, showing decreasing backbone-backbone packing length as expected from the positions of Peak 3. Finally, anion-anion correlations are plotted in Fig. 5.11c and d for $\lambda = 8$ and $\lambda = 16$ respectively. At $\lambda = 8$ hydration, TMP-PMPI-BB shows the strongest short-range correlation at 5.2 Å, followed by DMP-PMPI-BB, HMT-PMBI, then TMP-PMPI-MM and DMP-PMPI-MM, with the opposite trend at the intermediate length scale of 7.7 Å. A broad peak is visible in the higher-r region, corresponding to spacings between clusters or "channels" or anions, which is better-defined and at higher r for the DMP-PMPI-BB, corresponding to the well-defined clusters visible in Fig. 5.8e. At $\lambda = 16$, which was only performed for the methylated samples, ions show a stronger short-range correlation in HMT-PMBI, but the remaining profiles are nearly indistinguishable, with a broad peak centered at approximately 15Å.

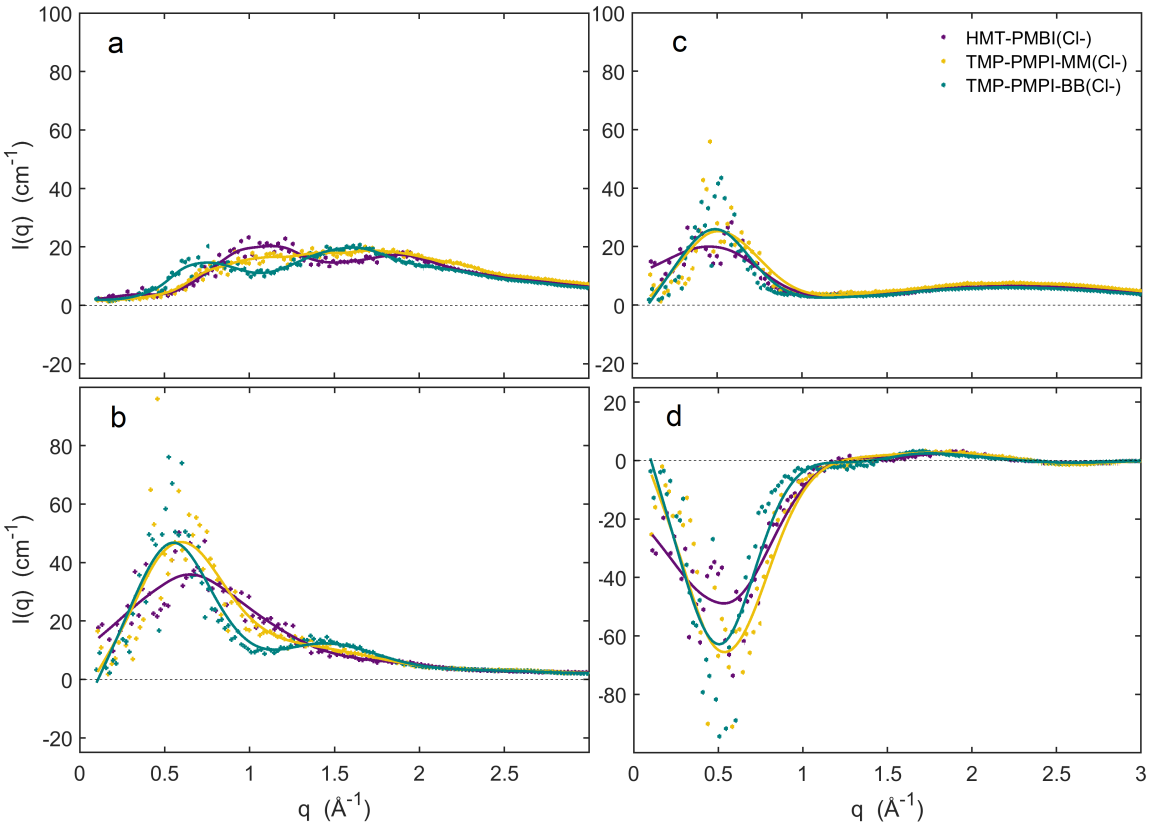

Figure 5.10: (a) Total scattering; and (b) polymer-polymer, (c) water-water, and (d) polymer-water partial structure factors for simulations of HMT−PMBI(Cl^-), TMP−PMPI−MM(Cl^-), and TMP−PMPI−BB(Cl^-) at $\lambda = 8$. DMP−PMPI profiles are very similar to TMP−PMPI, and are not shown here for readability.

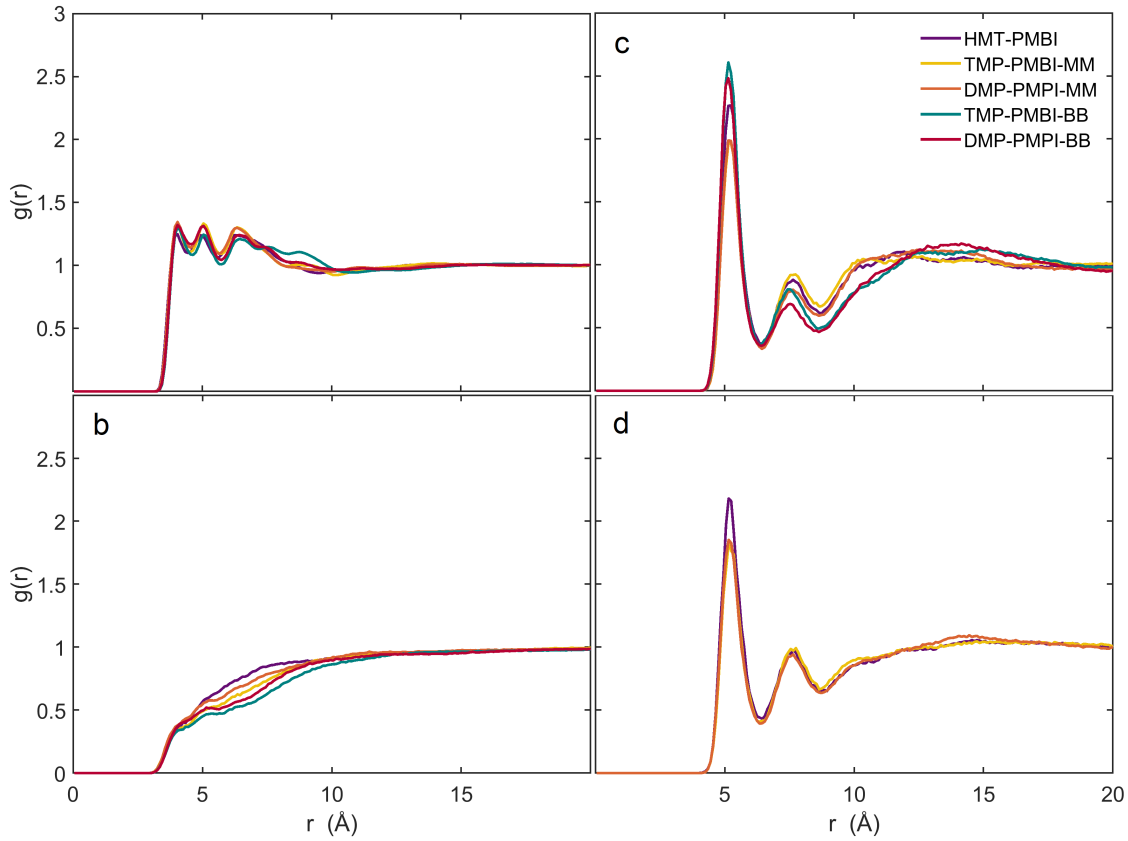

Figure 5.11: Pair-correlation functions calculated from simulations of each system; (a) polymer-anion pairs at $\lambda = 4$, (b) polymer-polymer pairs at $\lambda = 4$, (c) anion-anion pairs at $\lambda = 8$, and (d) anion-anion pairs at $\lambda = 16$.

5.4 Conclusions

Results for the three series of materials do not present dramatically different morphologies. For each system, two to three peaks appear in the WAXS regime, which do not evolve dramatically with hydration and correspond to intermolecular packing distances between polymer backbones, water molecules, and the anions, which simplify with increasing alkylation unit length as the polymers become bulkier. A mid-q peak is present in HMT−PMBI in TMP-PMPI, and corresponds to a common intramolecular spacing, which is not present in DMP-PMPI due to its asymmetric monomer. These interpretations are supported by $S(q)$ and $g(r)$ calculated from the molecular dynamics data. However, the mid-q feature ξ resists simple explanation; the most plausible interpretations – that it corresponds to the formation of anion clusters or extended water-rich domains – are not supported by the MD results in Fig. 5.11, and there is no clear reason why such a feature would form only in the TMP-PMPI samples at controlled humidity, unless those samples absorb significantly more water.

The molecular dynamics simulations also show that, unlike the methylated samples, TMP−PMPI−BB(Cl^-) and DMP−PMPI−BB(Cl^-) are not fully percolated at $\lambda = 4$, even though DMP−PMPI−MM(Cl^-) has a higher ion concentration than TMP-PMPI-BB. This shows that the bulky akylation groups may impede the formation of a percolating phase at low hydration, which may negatively impact conductivity; at $\lambda = 8$, each system showed full percolation. The impact of ion concentration will be explored further in Chapter 6.

Chapter 6

Accessible Volume, Ion Dynamics and Conductivity

In this chapter, phase volumes and anion diffusion coefficients calculated from simulation results are shown to provide intuition into the ion dynamics of these systems, focusing on chloride-form simulations due to the availability of experimental data. Calculations were performed using the 30 ns sampling periods discussed in Chapters 4 and 5. While they do not provide enough data to confidently calculate diffusion coefficients for the less hydrated samples, the available data is sufficient to estimate expected values. Ion conductivities derived from the diffusion coefficients are compared to literature experiments where measurements of both water content and ion conductivity are available, with which we found qualitative, but not quantitative, agreement.

6.1 Accessible Volume

As the nanostructures of each material appeared qualitatively similar, the relative phase volumes were investigated to determine whether these were correlated with ion mobility. The focus is on the fraction of accessible volume ϕ,[1]

$$\phi = \frac{V_{\text{acc}}}{V} \ , \tag{6.1}$$

where V is the total simulation cell volume and V_{acc} is total accessible volume, defined as the total cell volume in which a sphere of 1.4 Å radius would not overlap a backbone molecule as defined via the backbone atoms' van der Waals radii. This calculation was performed using the Caver package, as detailed in Chap. 3. For V_{acc}, the averages of seven frames each 5 ns apart were taken for each simulation. Standard errors were taken as uncertainty, and were below 1% for each simulation.

[1]This value is analogous to "porosity," which is usually defined experimentally as the maximum volume of water absorbed divided by (wet) volume.

Water/anion phase volume was also calculated, defined as the fraction of the accessible volume occupied by water molecules or anions, with each chloride ion and water molecule estimated to occupy 30 $Å^3$, corresponding to experimental values in bulk solution [109]. The free volume was then calculated as the difference between the accessible volume and the water/anion phase volume, and polymer phase volume was defined as the difference between the total volume and the accessible volume; i.e., the inaccessible volume.

The polymer phase, water/anion phase, and free volumes of HMT–PMBI(Cl^-) at different degrees of hydration are shown in Fig. 6.1a. The water/ion phase volume increases linearly with degree of hydration, as required by the definition used here. The free volume decreases steadily with hydration, while the polymer phase volume decreases slightly from $\lambda = 2$ to $\lambda = 8$ and increases slightly from $\lambda = 8$ to $\lambda = 16$; as the cells swell to accommodate more water, the polymers are not packed as tightly and are free to relax.

Results for TMP–PMPI–MM(Cl^-) and DMP–PMPI–MM(Cl^-) are very similar, with TMP–PMPI–MM(Cl^-) showing slightly less hydrocarbon phase volume and DMP–PMPI–MM(Cl^-) showing slightly more, reflecting the materials' different ion concentrations. Similarly, for TMP–PMPI–MM(Cl^-), the free volume decreases slightly faster than in HMT–PMBI(Cl^-), while in DMP–PMPI–MM(Cl^-), it decreases slightly slower; at $\lambda = 16$, the absolute free volumes are 78%, 80%, and 64% lower than at $\lambda = 2$ for HMT–PMBI(Cl^-), TMP–PMPI–MM(Cl^-), and DMP–PMPI–MM(Cl^-) respectively, highlighting that the majority of the accessible volume is occupied by water and counter-ions at that degree of hydration.

The accessible volumes for each material at each hydration are shown in Fig. 6.1a, increasing from approximately 22% at $\lambda = 2$ to approximately 55% at $\lambda = 16$. At each degree of hydration, TMP–PMPI–MM(Cl^-) shows the highest accessible volume, followed by DMP–PMPI–MM(Cl^-), HMT–PMBI(Cl^-), DMP–PMPI–BB(Cl^-), and DMP–PMPI–BB(Cl^-), respectively. This corresponds to decreasing order in terms of both ion concentration and IEC. The difference between the methylated samples increases with λ from $\lambda = 2$ to $\lambda = 8$, further reflecting the greater water content at each degree of hydration of the systems with higher IEC.

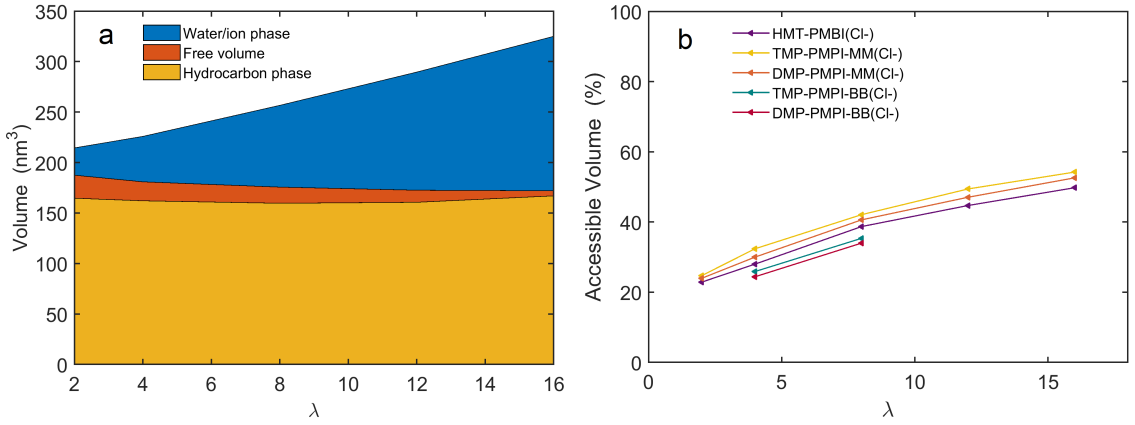

Figure 6.1: (a) Water/anion phase, free volume, and hydrocarbon phase volumes of HMT−PMBI(Cl^-) at various degrees of hydration as determined from the simulations, and (b) comparison of the accessible volume fraction of each material in chloride form, simulated at various degrees of hydration.

6.2 Ion Conductivity of HMT−PMBI

The mean-squared displacements of the anions in HMT−PMBI were plotted to visualize the motion of the anions, derive their diffusion coefficients, and estimate conductivities of HMT−PMBI for each counter-ion at different degrees of hydration. The plots reveal two regimes: a sub-diffusive regime at short time scales, and a diffusive regime at long time scales. This reflects the fact that the motion of the ions is constrained by the polymer backbones at short time scales, but is diffusive at larger time scales.

Mean-squared displacements as a function of lag time τ for each anion in HMT−PMBI are shown in Fig. 6.2. At $\lambda = 4$, shown in Fig. 6.2a, chloride and bromide, the ions of intermediate size, showed the largest mean-squared displacements and diffusion coefficients, followed by the smaller, most hydrophilic ions, fluoride and hydroxide, then by iodide, the least hydrophilic. Fluoride and hydroxide have tightly bound solvation shells and correspondingly large effective mobility, while the iodide ions, as seen in Fig. 4.9, are associated with the polymer backbones as the iodide-water interaction is not strong enough to solvate the iodide at low degrees of hydration. At $\lambda = 8$ (Fig. 6.2b), iodide showed a similar diffusion coefficient to bromide and chloride. In experiments, membranes with more hydrophilic counter-ions generally show the highest ion conductivities under constant relative humidity, but this is due to their larger water uptakes.

The experimentally-determined diffusion coefficients of iodide, bromide, and chloride in dilute solution are very similar, while the diffusion coefficient of fluoride is about 25% lower and that of hydroxide is much higher. Hydroxide ions are transported primarily via the Grotthus mechanism, a process in which hydrogen-oxygen bonds in hydroxide ions and water molecules are successively formed and broken in a manner similar to hole transport in

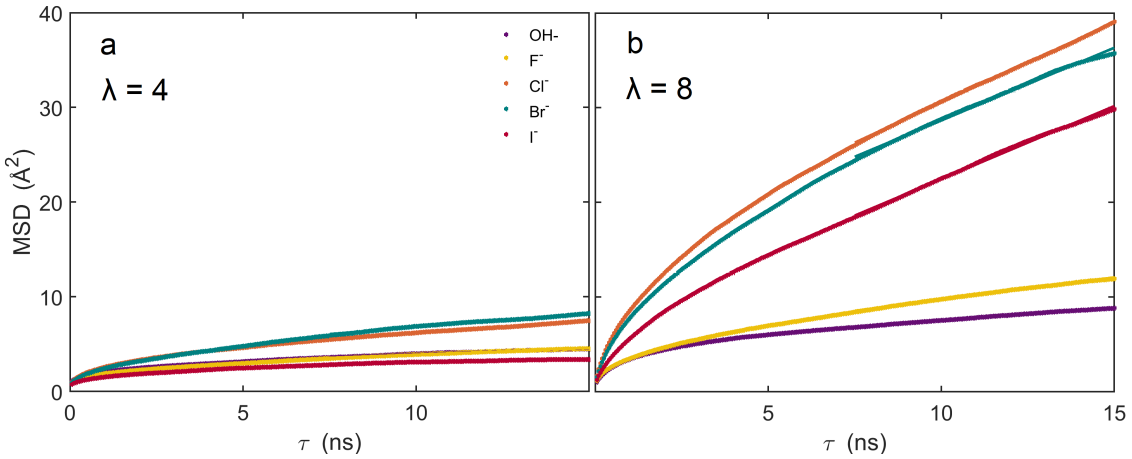

Figure 6.2: Mean-squared displacements of various anions in simulations of HMT−PMBI at (a) $\lambda = 4$, and (b) $\lambda = 8$. Linear regression fits to the data for $\tau > 7.5$ ns are shown as solid lines, which are only clearly discernible from the raw data for the chloride and bromidie ions at $\lambda = 8$.

semiconductors. As classical dynamics cannot simulate the breaking of covalent bonds, this process did not occur in the simulations. At low levels of hydration, the iodide ions were not well-solvated and were strongly associated with cationic sites on the polymer backbones, which results in lower mobility.

Table 6.1: Diffusion coefficients calculated from the fits to the data in Fig. 6.2 in units of 10^{-9} m^2/s for each ion in 87.5% dm HMT–PMBI at 297 K. Experimental values for a dilute solution of ions at the same temperature are provided for context.

Anion	D (10^{-9} m^2/s)			
	$\lambda = 4$	$\lambda = 8$	$\lambda = 16$	dilute solution (exp.) [110]
iodide	0.00012	0.00257	N/A	2.05
bromide	0.00049	0.00256	N/A	2.08
chloride	0.00042	0.00282	0.04033	2.03
fluoride	0.00023	0.00078	0.00779	1.48
hydroxide	0.00021[1]	0.00045[1]	0.00840[1]	5.27

[1] This represents vehicular diffusion only, as the simulation cannot model the Grotthus mechanism.

Diffusion coefficients were extracted from the long-τ regime according to Eq. 3.29, defined as $\tau > 7.5$ ns, via linear regression and are tabulated in Table 6.1. With the exception of bromide at $\lambda = 8$, each regression is indistinguishable from the raw data. However, as can be seen when mean-squared displacements are plotted with logarithmic axes in Fig. 6.3, these regressions are performed on less than a decade of data, which is not sufficient to confidently claim that the motion is in steady-state diffusion; these diffusion coefficients should be treated as estimates, especially those corresponding to poorly-hydrated materials.

Uncertainties are not provided for D and derived quantities due to the unavailability of uncertainties for the MSD calculations. Including a previous report using the same simulation protocol, four simulations of 87.5% dm HMT–PMBI(Cl^-) at $\lambda = 16$ with various simulation cell volumes show a mean value of $D = 3.79 \pm 0.09 \times 10^{-9}$ m^2/s. This is a relative uncertainty of 2.6%, but the error for less hydrated systems is certainly higher.

Mean-squared displacements of chloride anions are plotted with logarithmic axes in Fig. 6.3. This highlights the distinct timescales, but also that the diffusion coefficient is fit to less than a decade of data, and while the fits are not discernible from the data, it is not entirely clear that the diffusion has converged.

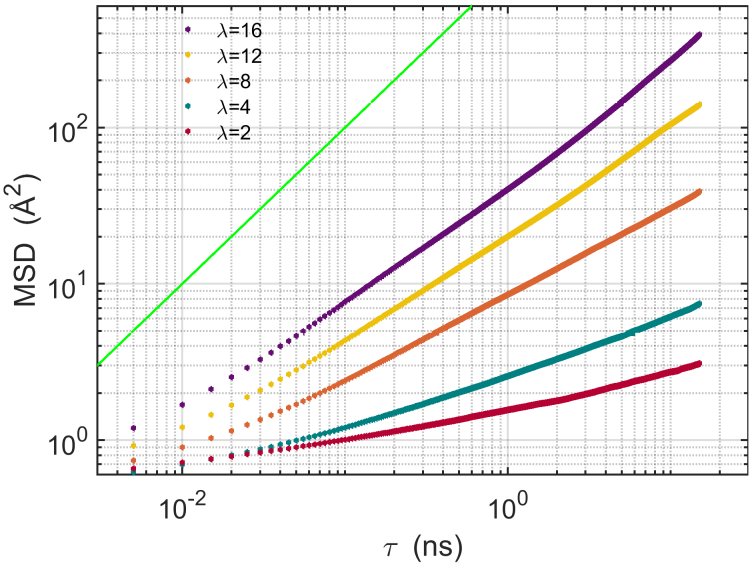

Figure 6.3: Chloride ion mean-squared displacements in simulations of HMT–PMBI(Cl^-) at various levels of hydration. Linear regressions to data for $\tau > 7.5$ ns are shown as lines, but are not easily discernible from the raw data. A slope of one is shown a solid green line.

6.3 Ion conductivity in imidazolium-based materials

Similar calculations were performed using the simulations of TMP-PMPI-MM, TMP-PMPI-BB, DMP-PMPI-MM, and DMP-PMPI-BB to determine how changing the backbone architecture and functionalization unit impacted the ion dynamics in the simulations, and compare to experimentally-determined conductivity. Mean-squared displacements calculated for chloride ions from each simulation are shown in Fig. 6.4. At all available time scales, the butylated systems, TMP–PMPI–BB and DMP–PMPI–BB, show significantly greater mean-squared displacement than the methylated samples, HMT–PMBI, TMP–PMPI–MM, and DMP–PMPI–MM, at similar degrees of hydration. HMT–PMBI shows the lowest mean-squared displacement at both levels of hydration, while the DMP samples show slightly higher mean-squared displacement at $\lambda = 4$ and slightly lower mean-squared displacement at $\lambda = 8$ than the corresponding TMP samples.

The simulation-derived chloride ion conductivites for each system are shown in Fig. 6.5a. Each system shows a rapid increase in conductivity with degree of hydration, but the trend with hydration is qualitatively similar in each system. Nonetheless, the greater conductivity of TMP–PMPI–MM(Cl^-) relative to DMP–PMPI–MM(Cl^-) and HMT–PMBI(Cl^-) at higher degrees of hydration reflect both a greater ion concentration and a higher diffusion coefficient, meaning that there are more ions per unit volume, and that those ions are more mobile.

Calculated diffusion coefficients for each system at each hydration level, as well as 1M NaCl solution, are plotted as a function of accessible volume in Fig. 6.5b. A linear regression fit to the logarithms obtained a slope of 6.2 $\pm$0.9 and explained 92.5% of the variance, confirming that accessible volume is the primary contributor to ion mobility in these systems. Diffusion through porous material is often described as $D = D_{\text{pore}} \frac{\phi}{\tau}$, where D_{pore} is the diffusion coefficient within the pore phase, often assumed to be equal to that in dilute or semidilute solution, ϕ is the pore volume fraction, analogous to χ, and τ is the *tortuosity*, a geometric parameter representing the increased effective path length through the media [111].[2] τ is equal to to approximately $\frac{1}{\sqrt{\phi}}$ for systems of packed sphere- or cylinder-like particles [113], so as τ and ϕ account for only a slope of 1.5, this shows that the diffusion coefficient within the water/anion phase scales rapidly with volume at the degrees of hydration considered, confirms that diffusion within the water/anion phase is far from bulk-like at all degrees of hydration considered, and motivates investigation of a wider range of hydrations. This further shows that, for these ionenes at least, accessible volume is the primary determiner of conductivity.

[2]In macroscopically porous materials where diffusion within the pores is bulk-like, τ is the squared ratio of the minimum path length through the pores to the actual distance [112].

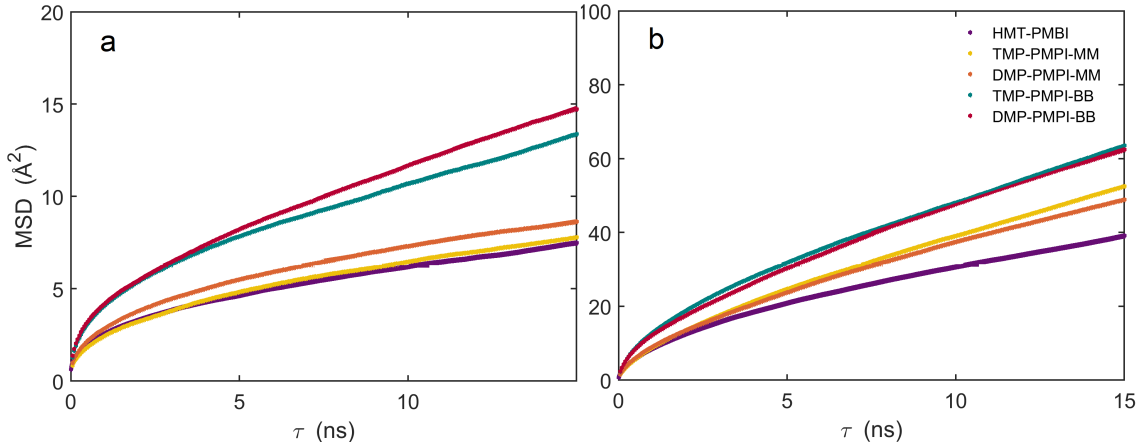

Figure 6.4: Chloride ion mean-squared displacements for each material at (a) $\lambda = 4$ and (b) $\lambda = 8$. Logistic regression fit to the $\tau > 7.5$ ns regime are shown as solid lines, and are indistinguishable from the data. TMP−PMPI−BB(Cl^-) and DMP−PMPI−BB(Cl^-) show greater mean-squared displacements at each time scale.

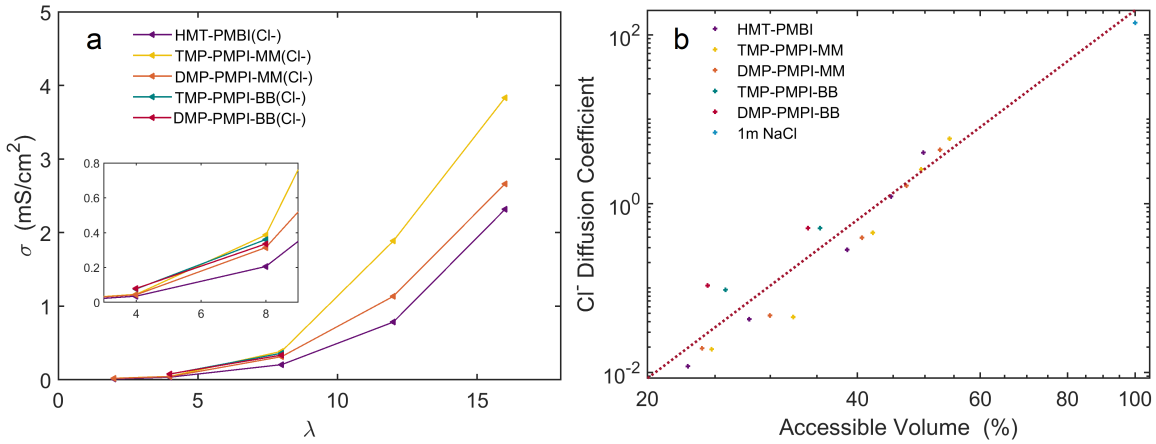

Figure 6.5: (a) Estimated ion conductivity of each material at various degrees of hydration. (b) Calculated diffusion coefficients for each simulation. The dotted line is a linear regression with slope 6.2 ± 0.9 and intercept -10.4 ± 1.8. Despite having the lowest ion concentrations, the butylated materials (green and red) show ion conductivities greater than DMP−PMPI−MM(Cl^-) and HMT−PMBI(Cl^-) at both degrees of hydration they were simulated at and above-trend ion mobility with accessible volume. The lines in (a) are a guide to the eyes with no physical meaning.

6.4 Comparison to experiment

Chloride ion conductivities taken from experiments reported in the literature and derived from the simulations from the diffusion coefficients using the Nernst-Einstein equation (Eq. 3.30) are plotted in Fig. 6.6; unfortunately, experimental data is only available for HMT−PMBI(Cl^-) and DMP−PMPI−MM(Cl^-).[3] As it is common in literature experiments to only measure membrane dimensions once under ambient conditions, the simulation-derived conductivities are additionally plotted as calculated using only the cell dimensions at $\lambda = 2$. Experimental conductivity values at full hydration are not included due to extreme uncertainty in the water content.

While the approximate shape of the experimental $\sigma - \lambda$ curves generally match the "uncorrected" simulation-derived curves, they do not quantitatively agree; while the experimental curve for HMT−PMBI(Cl^-) appears at lower hydration and/or higher conductivity, while the experimental curve for DMP−PMPI−MM(Cl^-) appears at higher hydration and/or lower conductivity. While it may seem more concerning that the maximum ion conductivities observed for TMP−PMPI−MM(Cl) and TMP−PMPI−BB(Cl) where much lower than those reported at 90% RH in Reference [44][4], water content at controlled humidity has not been measured for these samples, so direct comparison is impossible. While some degree of simulation error is certainly expected – the simulation parameters used underestimate the conductivity of semidilute solution by approximately 30% [75] – this comparison must be taken with additional caveats.

The experimentally-determined conductivity values as a function of hydration number for HMT−PMBI(Cl^-) were collected by cross-referencing two different papers utilizing different samples with slightly different degrees of functionalization, and were performed at slightly different temperatures [29, 49].[5] Furthermore, measurement of water uptake and conductivity at controlled humidity is experimentally challenging; in particular, measurement of water uptake requires obtaining a dry reference mass, and eliminating all water from a membrane is not possible.[6]

Membrane conductivity is most commonly reported in the literature by first fitting a measured electrochemical impedance spectrum to a Randles equivalent circuit [114], then

[3]Measurements of 92% df DMP−PMPI−EE(Cl^-), 78% df DMP−PMPI−PP(Cl^-), and 84% df DMP−PMPI−BB(Cl^-) conductivity as a function of hydration number are also available [46], but 84% df DMP−PMPI−BB(Cl^-) is not comparable to the simulation performed at 100% df.

[4]16.9 and 2.8 mS/cm, respectively - see Table 2.5

[5]Conductivities were measured for 85% and 90% dm HMT−PMBI(Cl^-), at 25° C, while water contents were measured for 89.7% dm HMT−PMBI at 30° C.

[6]The reference mass for HMT−PMBI(Cl^-) was obtained by equilibration at $\sim$ 0% RH, 60° C for 60 min.

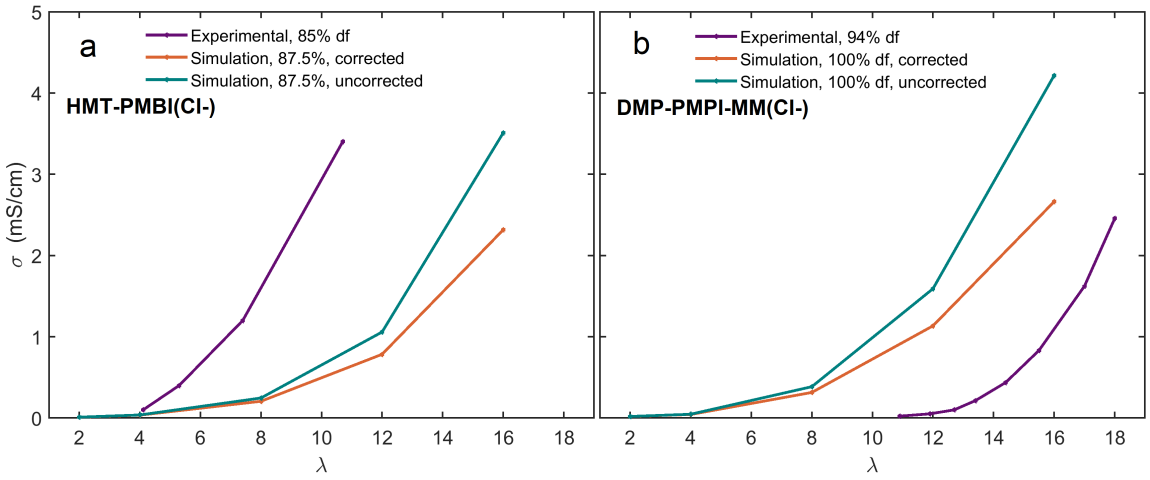

Figure 6.6: Simulation-estimated chloride ion conductivities compared to experimental values taken from the literature, for (a) HMT−PMBI(Cl^-) and (b) DMP−PMPI−MM(Cl^-). Conductivity data in (a) is taken from Reference [29], and hydration numbers are cross-referenced from measurements of an 89.7% df sample reported in Reference [49]; conductivity as a function of hydration number in (b) is taken directly from Reference [46]. The "corrected" curves from the simulation results are calculated using the cell dimensions at each degree of hydration, while the "uncorrected" curves use the cell dimensions at $\lambda = 2$.

taking the quotient of the *cell constant* and the derived steady-state resistance; i.e.,

$$\sigma = \frac{b}{R} = \frac{l}{RA} \ , \tag{6.2}$$

where σ is the conductivity, R is the steady-state resistance of the equivalent circuit determined by the fit, and b is the cell constant, defined as the membrane thickness l[7] divided by the cross-sectional membrane area A. However, it is common in the literature to measure A only once under ambient conditions [46], which would underreport conductivity in dry conditions and overreport conductivity in wet conditions. To observe an estimate of the potential scale of this discrepancy, we have included a plot of the estimated ion conductivity using the ion concentration calculated for $\lambda = 2$ to our comparisons with experimentally-observed conductivity.

[7]More precisely, the distance between the two spectrometer electrodes

6.5 Discussion

A recent report [46] noted that the experimental Cl^- conductivity of TMP–PMPI and DMP–PMPI at 95% RH appears to follow a power law with ion exchange capacity and suggested that for cationic ionenes, ion exchange capacity is the sole or primary determinant of the anion conductivity. From the definition of ion mobility, ion conductivity is proportional to both ion concentration and ion mobility,

$$\sigma = \mu F c, \tag{6.3}$$

where σ is the ion conductivity, μ is the ion mobility, c is the ion concentration, and F is Faraday's constant. (μ is proportional to D via the Nernst relation, $D = \mu RT$.) Clearly, c will be defined by both the ion exchange capacity (conventionally defined when the sample is dry) and the volumetric swelling, as ions will be diluted by additional water at higher hydrations. The ion conductivity plotted against ion concentration and accessible volume for each material is shown in Fig. 6.7, showing that at the range of hydrations considered, ion concentration decreases modestly while conductivity increases significantly; ion mobility is scales rapidly with accessible volume. For the claim that IEC defines conductivity to hold, IEC must also determine swelling behavior; this does not extend, at least, to cross-linked materials, which demonstrated higher chloride ion conductivity at lower IEC under wet conditions [29] than uncrosslinked analogues. This is consistent with the results in this chapter, which also suggest that the highest-performing materials will have high ion exchange capacities, high water content, controlled dimensional swelling, and high free volume at low humidities.

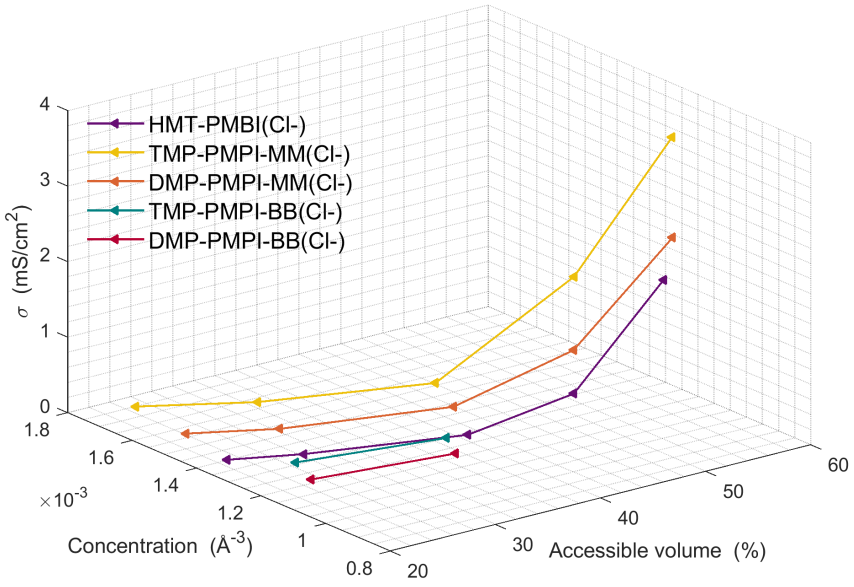

Figure 6.7: Simulation-derived ion conductivity plotted against ion concentration and accessible volume. The lines are merely a guide to the eyes. Each line represents one system at a variety of hydrations.

Chapter 7

Conclusions and Outlook

This thesis provides a comprehensive investigation into the nanostructure of sterically hindered cationic ionenes. X-ray scattering and molecular dynamics results combine to show that each of these materials shows simple morphologies with no long-range phase separation. The polymer backbones provide mechanical stability by entangling, but do not crystallize or aggregate as in PFSA-based CEM systems. While the existence of longer-range inhomogeneities cannot be ruled out with complete certainty, no evidence for such inhomogeneity was found in this work.

The molecular dynamics results were also leveraged to explore the ion mobilities and conductivities of the systems. As in the analysis of the nanostructure, fundamental differences between each system were not observed. Rather, preliminary results suggested that ion mobility in each system and at each level of hydration follows a power law with accessible volume at all levels of hydration considered.

7.1 Conclusions

X-ray scattering measurements of HMT−PMBI show three or four peaks, which evolve only modestly with hydration. Peak 4, which corresponds to short-range interatomic spacings, moderately increases in amplitude and q with relative humidity, while the remaining peaks, corresponding to intermolecular spacings of approximately $6-7$ Å and an intramolecular spacing of 2 nm, do not evolve significantly, showing only a moderate reduction in intensity when increasing humidity from 0% to 30%. At controlled humidity, no low-q features were present, and the scattering smoothly transitioned from a flat background at intermediate q to a power law in the Porod regime. However, a subtle additional feature was present in the fully-hydrated HMT−PMBI(Cl^-). This feature does not have a well-defined peak position and appears to correspond to a correlation length of approximately 5 Å in the water/anion phase.

These interpretations were supported by molecular dynamics results. Direct visualization of the molecular dynamics simulations show a sponge-like nanostructure, in which

water occupies void space between inefficiently-packed polymer backbones at low hydration levels, before permeating the available space and swelling at higher levels of humidity. Total scattering profiles calculated from the simulation results show remarkable, quantitative agreement with experimental results, and partial structure factors reveal that a lack of contrast between the polymer and water/anion phases prevented the observation of the phase separation via X-ray scattering.

WAXS results are similar for each of the three series of polymers. Each sample showed three to four peaks which changed only subtly with hydration. One peak, corresponding to spacings of approximately 6 Å, weakened in intensity with aklylation unit length and ultimately was not visible in TMP–PMPI–BB(Cl^-). The only nm-scale peak was present in the TMP-PMPI series, which corresponded to a length scale of approximately 9.5 Å, a regular spacing along the polymer backbones. Molecular dynamics also show similar nanostructures at high degrees of hydration, but reveal that unlike the methylated systems, the water/anion phases of TMP–PMPI–BB(Cl^-) and DMP–PMPI–BB(Cl^-) samples form discrete clusters of water and anions at $\lambda = 4$.

Finally, investigation of the anion dynamics in the simulations revealed two distinct timescales for each – a subdiffusive regime at short τ in which the motion of the anions were constrained by the polymer backbones, and a diffusive regime at long τ. The subdiffusive regime was significantly longer for the less hydrated samples, as poorly-hydrated anions appear to 'hop' between favourable sites, while well-hydrated anions continuously explore the available space. Plotting the chloride anion diffusion coefficients as a function of accessible volume revealed an unexpectedly strong relationship, with the diffusion coefficient appearing to follow a power law of $D \propto \chi^{6.2\pm0.9}$ across the entire range considered, from 21% for HMT–PMBI(Cl^-) at $\lambda = 2$ up to 100% for 1M NaCl solution. However, quantitative agreement with experimental conductivity values was not achieved, as the simulation reported significantly lower values at all levels of hydration. There is certainly a significant element of simulation error, as the force field and simulation protocol used here underestimates the diffusion coefficient of chloride ions in solution by 30%. The difficulty of measuring the true water content of membranes likely plays a role in this disagreement as well.

7.2 Outlook

There is poor contrast between the hydrocarbon polymer backbones and the water- and ion-rich phase, largely limiting the utility of the X-ray scattering measurements to observing short-range packing lengths between polymers, anions, and water molecules. Poor X-ray contrast between hydrocarbon polymers and water has been established in the CEM field, where it is generally addressed by the exchange of the proton counter-ions ions with

tetramethyl ammonium cations. However, contrast did not appear in this work despite varying counter-ions from chloride to iodide.

The X-ray *scattering length density* is defined as

$$SLD = \sum_i \frac{b_i(\lambda)}{V} \ , \tag{7.1}$$

where

$$b_i = r_e f_i(\lambda) \ , \tag{7.2}$$

where V is the phase volume, $b_i(\lambda)$ is atomic scattering length, $f_i(\lambda)$ is the real component of the atomic scattering factor, and r_e is the classical electron radius.[1] While $f_i(\lambda)$ nominally depends on the wavelength of incident radiation, in practice it is proportional to the number of electrons, except near absorption lines, and as such, the SLD is proportional to the electron density.

Based on conventional ionic volumes in water, chloride, bromide, and iodide ions contribute approximately 0.60, 0.88, and 0.90 electrons/Å^3, respectively [98], while water molecules contribute 0.33/Å^3. Utilizing the estimate of volume occupied by the polymer backbone in HMT–PMBI(Cl^-) at $\lambda = 4$ of 71.8%, the electron density of the polymer backbone is 0.41 electrons/Å^3, below that of the ions, but above that of water.

Scattering length densities of the water and polymer phases for HMT–PMBI(Cl^-), (Br^-), and (I^-) were calculated via the NIST SLD calculation tool [115], utilizing phase densities taken from the simulations, and are shown in Table 7.1, utilizing data taken Reference [115]. This confirms that the SLD of the water/anion phase is slightly higher than the polymer phase at low hydration, and slightly lower than the polymer phase at high hydration.

Nonetheless, a shoulder that appears to correspond to disorganized inhomogeneity is present in TMP–PMPI(Cl^-) samples at high humidity, and in some HMT–PMBI(Cl^-) and DMP–PMPI(Cl^-) samples when fully hydrated. The source of contrast for this feature is not clear; the most plausible explanation identified is that it represents the formation of clusters of anions. However, such behavior was not observed in the molecular dynamics simulations, and it is unclear why this would only occur in certain samples.

It may be possible to enhance the contrast between the hydrocarbon and solvent/anion phases by increasing the electron density of the latter, by dissolving additional ions or blending with more electron-dense solvent such as glycerol or dimethyl sulfoxide [116]. This would only be effective at high solvent content due to the extreme concentration of counter-ions at low hydration, and would potentially impact material structure and water uptake

[1] r_e is approximately 2.818×10^{-15}m, equal to $\frac{e^2}{4\pi\epsilon_0 m_e c^2}$, where e is the fundamental charge, ϵ_0 is the vacuum permittivity, m_e is the electron mass, and c is the vacuum speed of light.

Table 7.1: The scattering length densities of the polymer and water/anion phase of HMT–PMBI(Cl^-), (Br^-), and (I^-) systems at various degrees of hydration.

System	Polymer phase SLD ($\times 10^{-6}$ Å^{-2})	Water/anion phase SLD ($\times 10^{-6}$ Å^{-2})	Difference ($\times 10^{-6}$ Å^{-2})
HMT–PMBI(Cl^-), $\lambda = 2$	11.000	11.654	-0.650
HMT–PMBI(Cl^-), $\lambda = 4$	11.182	10.762	0.420
HMT–PMBI(Cl^-), $\lambda = 8$	11.637	10.170	1.467
HMT–PMBI(Cl^-), $\lambda = 12$	11.273	9.942	1.331
HMT–PMBI(Cl^-), $\lambda = 16$	10.882	9.822	1.060
HMT–PMBI(Br^-), $\lambda = 4$	11.172	13.043	-1.871
HMT–PMBI(Br^-), $\lambda = 8$	11.377	11.499	-0.122
HMT–PMBI(I^-), $\lambda = 4$	11.330	13.305	-1.975
HMT–PMBI(I^-), $\lambda = 8$	11.252	11.720	-0.468
TMP–PMPI–MM(Cl^-), $\lambda = 2$	10.912	11.650	-0.738
TMP–PMPI–MM(Cl^-), $\lambda = 4$	11.253	10.762	0.491
TMP–PMPI–MM(Cl^-), $\lambda = 8$	11.230	10.170	1.060
TMP–PMPI–MM(Cl^-), $\lambda = 12$	11.079	9.942	1.137
TMP–PMPI–MM(Cl^-), $\lambda = 16$	10.727	9.822	0.905
TMP–PMPI–BB(Cl^-), $\lambda = 4$	10.458	10.762	-0.304
TMP–PMPI–BB(Cl^-), $\lambda = 8$	10.503	10.170	0.333
DMP–PMPI–MM(Cl^-), $\lambda = 2$	10.896	11.650	-0.754
DMP–PMPI–MM(Cl^-), $\lambda = 4$	11.117	10.762	0.355
DMP–PMPI–MM(Cl^-), $\lambda = 8$	11.387	10.170	1.217
DMP–PMPI–MM(Cl^-), $\lambda = 12$	11.150	9.942	1.208
DMP–PMPI–MM(Cl^-), $\lambda = 16$	11.031	9.822	1.209
DMP–PMPI–BB(Cl^-), $\lambda = 4$	10.435	10.762	-0.327
DMP–PMPI–BB(Cl^-), $\lambda = 8$	10.588	10.170	0.418

properties [117]. Small-angle neutron scattering (SANS) has been successfully utilized to show phase separation in materials where X-ray contrast is poor, including hydrocarbon ionomers [24, 26]. These materials showed phase separation at somewhat larger length scales than those observed in this work, consistent with partial structure factors calculated from simulations of similar materials [25]. The MacSANS small-angle neutron scattering instrument currently under construction at McMaster University, estimated to be available late 2021, will provide access to SANS for Canadian researchers. Both SANS and contrast-enhanced SAXS measurements of the hydrocarbon ionenes are the subject of planned future work.

Dynamics and Ion Conductivity

The strength of the relationship between chloride ion mobility and accessible volume – a power law which appears to hold for each material at each analyzed degree of hydration, from approximately 20% accessible volume (ie, HMT−PMBI(Cl^-) at $\lambda = 2$) to approximately 100% accessible volume (ie, ions in semi-dilute solution) – was surprising. Confidence in this relationship must be established by extending simulation durations to provide at least a decade of linear MSD behavior in order to provide confident estimates of ion mobility, and by verifying via experiment where possible. Further simulations should likely be performed using water and anion models with better ion dynamics performance. Quantitative agreement was not obtained with the limited existing experimental data, and in particular, the superior ion conductivity of TMP-PMPI materials was not observed. Dynamic vapour sorption measurements of TMP-PMPI samples are necessary to confirm the water contents these high conductivities are achieved at.

While accessible volume as defined in this thesis is not an experimentally accessible property, the related values of *water volume fraction* χ_v or *porosity* ϵ are common and can be estimated from either volumetric swelling VE or water uptake by mass WU, and should be very similar, especially at high levels of hydration. Authors including Kim and Pivovar have advocated for focus on such volume-based parameters over IEC, noting in 2010 that χ_v was a much better predictor of ion conductivity than either IEC or WU for a large set of CEM polymers under full hydration [118]. A plot of the proton conductivities of many CEM materials under full hydration is shown in Fig. 7.1; while a similar power law appears to be exhibited at low χ_v, proton conductivity begins to plateau at approximately $\chi_v = 50\%$. This is because at high water content, additional water reduces the ion concentration more rapidly than the accessible volume is increased. This relationship was found to break down when materials at low hydration were considered, likely due to poor percolation. A percolation threshold effect was not observed in the materials studied here; even though not all water and anions were directly connected at very low degrees of hydration.

Atomistic molecular dynamics generally, and the force field parameters used here specifically, do not produce quantitatively accurate diffusion coefficients, even for the case of

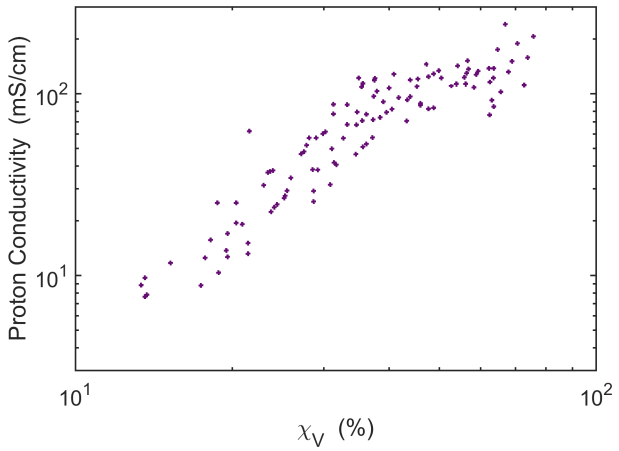

Figure 7.1: Experimentally-determined proton conductivity for a wide range of fully-hydrated CEM polymers. This data was taken from Reference [118].

semi-dilute solution [119]. Nonetheless, the molecular dynamics simulations did not reproduce the high conductivities expected from experimental results for HMT−PMBI(Cl^-) and DMP−PMPI−MM(Cl^-), which draw the conclusions from the simulations into question. There is the additional concern with reported ion conductivity and water uptake values, which vary significantly between reports. As conductivity is greatly impacted by water content, the precise hydration numbers of experimental samples must be known in order to meaningfully compare experimental and simulation results.

It has been reported recently that macroscopic ion conductivity is defined solely ion exchange capacities in ionene materials such as those studied in this thesis, due to their amorphous nature and the lack of long-range phase separation discussed here [46]. This claim was supported by the apparent power law relationship of approximately $\sigma_{Cl} \propto (IEC)^7$ between chloride ion conductivity at 95% RH over eight samples of TMP-PMPI and DMP-PMPI, at both 30° C and 80° C. However, it must be noted that this does not simply represent an increase in the ion concentration, which as shown in Equ. 6.3 is directly proportional to σ – it must also represent a power law increase in μ with IEC, driven by an increase in water uptake and accessible volume.

Final Notes

As the hydroxide forms of AEMs are unstable in air, this thesis focuses on the structure and dynamics of materials in halide forms. However, while experimentally-determined chloride ion conductivities for these samples vary significantly, the reported 'true' OH^- conductivities of HMT−PMBI(OH−) and DMP−PMPI−MM(OH−) are quite similar, 103 mS/cm for HMT−PMBI(OH−) [30] and 120 mS/cm for DMP−PMPI−MM(OH−) [46]; these values are among the highest reported OH^- ion conductivities for any AEM material un-

der similar conditions [31]. The higher performance of DMP−PMPI−MM(OH−) under these circumstances suggests that hydroxide ion conductivity via the Grotthus mechanism may be less dependent on accessible volume than vehicular diffusion is. This should also be investigated in future work.

Bibliography

[1] J. Krol, M Wessling, and H Strathmann. "Concentration polarization with monopolar ion exchange membranes: current–voltage curves and water dissociation". *Journal of Membrane Science* 162.1 (1999), pp. 145–154.

[2] J. R. Varcoe et al. "Anion-exchange membranes in electrochemical energy systems". *Energy & Environmental Science* 7.10 (2014), pp. 3135–3191.

[3] K. Emmanuel et al. "Imidazolium functionalized anion exchange membrane blended with PVA for acid recovery via diffusion dialysis process". *Journal of Membrane Science* 497 (2016), pp. 209–215.

[4] I. Vincent and D. Bessarabov. "Low cost hydrogen production by anion exchange membrane electrolysis: A review". *Renewable and Sustainable Energy Reviews* 81 (2018), pp. 1690–1704.

[5] K.-D. Kreuer. "Ion conducting membranes for fuel cells and other electrochemical devices". *Chemistry of Materials* 26.1 (2013), pp. 361–380.

[6] G. Offer et al. "Comparative analysis of battery electric, hydrogen fuel cell and hybrid vehicles in a future sustainable road transport system". *Energy Policy* 38.1 (2010), pp. 24–29.

[7] N Sulaiman et al. "A review on energy management system for fuel cell hybrid electric vehicle: Issues and challenges". *Renewable and Sustainable Energy Reviews* 52 (2015), pp. 802–814.

[8] E. Eriksson and E. M. Gray. "Optimization and integration of hybrid renewable energy hydrogen fuel cell energy systems–A critical review". *Applied Energy* 202 (2017), pp. 348–364.

[9] S. T. Thompson et al. "Direct hydrogen fuel cell electric vehicle cost analysis: System and high-volume manufacturing description, validation, and outlook". *Journal of Power Sources* 399 (2018), pp. 304–313.

[10] S. T. Thompson et al. "Perspective—the next decade of AEMFCs: near-term targets to accelerate applied R&D". *Journal of The Electrochemical Society* 167.8 (2020), p. 084514.

[11] M. Houde et al. "Monitoring of perfluorinated compounds in aquatic biota: an updated review: PFCs in aquatic biota". *Environmental science & technology* 45.19 (2011), pp. 7962–7973.

[12] D. R. Dekel. "Review of cell performance in anion exchange membrane fuel cells". *Journal of Power Sources* 375 (2018), pp. 158–169.

[13] M. Miotti et al. “Personal vehicles evaluated against climate change mitigation targets”. *Environmental Science and Technology* 50.20 (2016), pp. 10795–10804.

[14] U. Krewer et al. “Impact of carbonation processes in anion exchange membrane fuel cells”. *Electrochimica Acta* 263 (2018), pp. 433–446.

[15] N. Ziv, W. E. Mustain, and D. R. Dekel. “The Effect of Ambient Carbon Dioxide on Anion-Exchange Membrane Fuel Cells”. *ChemSusChem* 11.7 (2018), pp. 1136–1150.

[16] E. M. Tsang et al. “Nanostructure, morphology, and properties of fluorous copolymers bearing ionic grafts”. *Macromolecules* 42.24 (2009), pp. 9467–9480.

[17] T. Weissbach et al. “Structural effects on the nano-scale morphology and conductivity of ionomer blends”. *Journal of Materials Chemistry* 22.46 (2012), pp. 24348–24355.

[18] A. Eftekhari. *Polymerized Ionic Liquids*. Smart Materials. Burlington House, Piccadilly, Mayfair, London: Royal Society of Chemistry, 2017.

[19] W. Xiao, Q. Yang, and S. Zhu. “Comparing ion transport in ionic liquids and polymerized ionic liquids”. *Scientific Reports* 10.1 (2020), pp. 1–12.

[20] A. G. Wright, T. Weissbach, and S. Holdcroft. “Poly (phenylene) and m-Terphenyl as Powerful Protecting Groups for the Preparation of Stable Organic Hydroxides”. *Angewandte Chemie International Edition* 55.15 (2016), pp. 4818–4821.

[21] S. Holdcroft and J. Fan. “Sterically-encumbered ionenes as hydroxide ion-conducting polymer membranes”. *Current Opinion in Electrochemistry* 18 (2019), pp. 99–105.

[22] J. A. Elliott et al. “A unified morphological description of Nafion membranes from SAXS and mesoscale simulations”. *Soft Matter* 7.15 (2011), pp. 6820–6827.

[23] H.-L. Lin et al. “Morphology study of Nafion membranes prepared by solutions casting”. *Journal of Polymer Science Part B: Polymer Physics* 43.21 (2005), pp. 3044–3057.

[24] L. He et al. “From solutions to membranes: structure studies of sulfonated polyphenylene ionomers”. *Macromolecules* 42.18 (2009), pp. 7084–7090.

[25] E. G. Sorte et al. “Impact of hydration and sulfonation on the morphology and ionic conductivity of sulfonated poly (phenylene) proton exchange membranes”. *Macromolecules* 52.3 (2019), pp. 857–876.

[26] T. J. Skalski et al. “Sulfophenylated Terphenylene Copolymer Membranes and Ionomers”. *ChemSusChem* 11.23 (2018), pp. 4033–4043.

[27] E. M. Schibli et al. “Morphology of anion-conducting ionenes investigated by X-ray scattering and simulation”. *Journal of Physical Chemistry B* 122.5 (2018), pp. 1730–1737.

[28] E. M. Schibli et al. “The Nanostructure of HMT-PMBI, a Sterically Hindered Ionene”. *Macromolecules* 53.12 (2020), pp. 4908–4916.

[29] T. Weissbach et al. “Simultaneous, synergistic control of ion exchange capacity and cross-linking of sterically-protected poly (benzimidazolium)s”. *Chemistry of Materials* 28.21 (2016), pp. 8060–8070.

[30] N. Ziv and D. R. Dekel. “A practical method for measuring the true hydroxide conductivity of anion exchange membranes”. *Electrochemistry Communications* 88 (2018), pp. 109–113.

[31] A. Zhegur-Khais et al. “Measuring the true hydroxide conductivity of anion exchange membranes”. *Journal of Membrane Science* 612 (2020), p. 118461.

[32] O. D. Thomas et al. “Anion conducting poly (dialkyl benzimidazolium) salts”. *Polymer Chemistry* 2.8 (2011), pp. 1641–1643.

[33] D. Henkensmeier et al. “Polybenzimidazolium-Based Solid Electrolytes”. *Macromolecular Materials and Engineering* 296.10 (2011), pp. 899–908.

[34] M. Hu, E. M. Pearce, and T. Kwei. “Modification of polybenzimidazole: Synthesis and thermal stability of poly (N1-methylbenzimidazole) and poly (N1, N3-dimethylbenzimidazolium) salt”. *Journal of Polymer Science Part A: Polymer Chemistry* 31.2 (1993), pp. 553–561.

[35] O. D. Thomas et al. “A stable hydroxide-conducting polymer”. *Journal of the American Chemical Society* (2012), pp. 10753–10756.

[36] K. J. W. Y. Soo. “An Investigation into Polybenzimidazoles as Anion Exchange Membranes”. Master’s thesis. 2013.

[37] A. G. Wright and S. Holdcroft. “Hydroxide-stable ionenes”. *ACS Macro Letters* 3.5 (2014), pp. 444–447.

[38] A. G. Wright et al. “Hexamethyl-p-terphenyl poly (benzimidazolium): a universal hydroxide-conducting polymer for energy conversion devices”. *Energy & Environmental Science* 9.6 (2016), pp. 2130–2142.

[39] X. Luo et al. “Water permeation through anion exchange membranes”. *Journal of Power Sources* 375 (2018), pp. 442–451.

[40] A. G. Wright and S. Holdcroft. “Hydroxide-Stable Ionenes”. *ACS Macro Letters* 3 (2014), pp. 444–447.

[41] H. Long and B. Pivovar. “Hydroxide degradation pathways for imidazolium cations: A DFT study”. *The Journal of Physical Chemistry C* 118.19 (2014), pp. 9880–9888.

[42] K. M. Hugar, H. A. Kostalik IV, and G. W. Coates. “Imidazolium cations with exceptional alkaline stability: a systematic study of structure–stability relationships”. *Journal of the American Chemical Society* 137.27 (2015), pp. 8730–8737.

[43] J. Fan et al. “Cationic polyelectrolytes, stable in 10 M KOH at 100 C”. *ACS Macro Letters* 6.10 (2017), pp. 1089–1093.

[44] J. Fan et al. “Poly (bis-arylimidazoliums) possessing high hydroxide ion exchange capacity and high alkaline stability”. *Nature Communications* 10.1 (2019), p. 2306.

[45] W. Li. “Poly(arylene imidazolium)s: Towards Stable Hydroxide Ion Exchange Membranes”. Master’s thesis. Simon Fraser University, 2019.

[46] P. Overton et al. “Tuning Ion Exchange Capacity in Hydroxide-Stable Poly (arylimidazolium) Ionenes: Increasing the Ionic Content Decreases the Dependence of Conductivity and Hydration on Temperature and Humidity”. *Macromolecules* 53.23 (2020), pp. 10548–10560.

[47] J. C. Stewart. “Effects of Counter-Anion Exchange on HMT-PMBI Investigated via X-ray Scattering”. Honours thesis. Simon Fraser University, 2019.

[48] N. Ziv et al. “Effect of CO2 on the properties of anion exchange membranes for fuel cell applications”. *Journal of Membrane Science* 586 (2019), pp. 140–150.

[49] Y. Zheng et al. “Water uptake study of anion exchange membranes”. *Macromolecules* 51.9 (2018), pp. 3264–3278.

[50] Y. Li et al. “Synthesis and characterization of controlled molecular weight disulfonated poly (arylene ether sulfone) copolymers and their applications to proton exchange membranes”. *Polymer* 47.11 (2006), pp. 4210–4217.

[51] R. Roe and P. Roe. *Methods of X-ray and Neutron Scattering in Polymer Science*. Topics in polymer science : a series of advanced textbooks and monographs. Great Clarendon St, Oxford, United Kingdom: Oxford University Press, 2000.

[52] E. M. Schibli. “Analysis of novel ionenes via X-ray and neutron scattering”. Master’s thesis. Simon Fraser University, 2016.

[53] L. Alexander. *X-ray Diffraction Methods in Polymer Science*. Krieger, 1979. ISBN: 9780882758015.

[54] H. Klug and L. Alexander. *X-ray Diffraction Procedures for Polycrystalline and Amorphous Materials*. J. Wiley, 1964.

[55] B. Hammouda. *Probing Nanoscale Structures – The SANS Toolbox*. Gaithersburg, Md. 20899-6102: National Institute of Standards and Technology, 2016.

[56] R. Lopez-Ruiz and E. M. Anitas. “Complexity in Biological and Physical Systems - Bifurcations, Solitons and Fractals”. 5 Princes Gate Court, London, UK: IntechOpen, Ltd., 2017. Chap. Small-Angle Scattering from Mass and Surface Fractals.

[57] A. Hindeleh and D. Johnson. “The resolution of multipeak data in fibre science”. *Journal of Physics D: Applied Physics* 4.2 (1971), p. 259.

[58] S. Rabiej. “A comparison of two X-ray diffraction procedures for crystallinity determination”. *European Polymer Journal* 27.9 (1991), pp. 947–954.

[59] S. Rabiej. “Determination of the crystallinity of polymer blends by an X-ray diffraction method”. *European Polymer Journal* 29.4 (1993), pp. 625–633.

[60] A. Szymczyk. “Structure and properties of new polyester elastomers composed of poly (trimethylene terephthalate) and poly (ethylene oxide)”. *European Polymer Journal* 45.9 (2009), pp. 2653–2664.

[61] B. Hammouda, D. L. Ho, and S. Kline. “Insight into clustering in poly (ethylene oxide) solutions”. *Macromolecules* 37.18 (2004), pp. 6932–6937.

[62] S. R. Kline. “Reduction and analysis of SANS and USANS data using IGOR Pro”. *Journal of Applied Crystallography* 39.6 (2006), pp. 895–900.

[63] E. M. Saffer et al. “SANS study of highly resilient poly (ethylene glycol) hydrogels”. *Soft Matter* 10.12 (2014), pp. 1905–1916.

[64] P. De Gennes. “Dynamics of entangled polymer solutions. I. The Rouse model”. *Macromolecules* 9.4 (1976), pp. 587–593.

[65] H Benoit and M Benmouna. “Scattering from a polymer solution at an arbitrary concentration”. *Polymer* 25.8 (1984), pp. 1059–1067.

[66] L. S. Dodda et al. “LigParGen web server: an automatic OPLS-AA parameter generator for organic ligands”. *Nucleic Acids Research* 45.W1 (2017), W331–W336.

[67] W. L. Jorgensen, D. S. Maxwell, and J. Tirado-Rives. "Development and testing of the OPLS all-atom force field on conformational energetics and properties of organic liquids". *Journal of the American Chemical Society* 118.45 (1996), pp. 11225–11236.

[68] S. V. Sambasivarao and O. Acevedo. "Development of OPLS-AA force field parameters for 68 unique ionic liquids". *Journal of Chemical Theory & Computation* 5.4 (2009), pp. 1038–1050.

[69] M. K. Dahlgren et al. "Characterization of biaryl torsional energetics and its treatment in OPLS all-atom force fields". *Journal of Chemical Information and Modeling* 53.5 (2013), pp. 1191–1199.

[70] S. Plimpton. "Fast parallel algorithms for short-range molecular dynamics". *Journal of Computational Physics* 117.1 (1995), pp. 1–19.

[71] A. I. Jewett, Z. Zhuang, and J.-E. Shea. "Moltemplate: a coarse-grained model assembly tool". *Biophysical Journal* 104.2 (2013), 169a.

[72] D. Hofmann et al. "Detailed-atomistic molecular modeling of small molecule diffusion and solution processes in polymeric membrane materials". *Macromolecular Theory and Simulations* 9.6 (2000), pp. 293–327.

[73] L. J. Abbott, K. E. Hart, and C. M. Colina. "Polymatic: a generalized simulated polymerization algorithm for amorphous polymers". *Theoretical Chemistry Accounts* 132.3 (2013), p. 1334.

[74] L. Martínez et al. "Packmol: A package for building initial configurations for molecular dynamics simulations". *Journal of Computational Chemistry* 30.13 (2009), pp. 2157–2164.

[75] C. Lohn. "System-size dependence of diffusion coefficients and radialdistribution functions from aqueous molecular dynamics simulations of NaCl and HMT-PMBI(Cl-)". Co-op report. Simon Fraser University, 2020.

[76] L. J. Abbott and A. L. Frischknecht. "Nanoscale structure and morphology of sulfonated polyphenylenes via atomistic simulations". *Macromolecules* 50.3 (2017), pp. 1184–1192.

[77] J. L. Abascal and C. Vega. "A general purpose model for the condensed phases of water: TIP4P/2005". *Journal of Chemical Physics* 123.23 (2005), p. 234505.

[78] J.-P. Ryckaert, G. Ciccotti, and H. J. Berendsen. "Numerical integration of the Cartesian equations of motion of a system with constraints: molecular dynamics of n-alkanes". *Journal of Computational Physics* 23.3 (1977), pp. 327–341.

[79] W. Humphrey, A. Dalke, and K. Schulten. "VMD: visual molecular dynamics". *J. Mol. Graph.* 14.1 (1996), pp. 33–38.

[80] H. Liu and S. J. Paddison. "Direct calculation of the X-ray structure factor of ionic liquids". *Physical Chemistry Chemical Physics* 18.16 (2016), pp. 11000–11007.

[81] P. J. Brown et al. "Intensity of diffracted intensities". *International Tables for Crystallography Volume C: Mathematical, Physical and Chemical Tables*. Ed. by E. Prince. Dordrecht: Springer Netherlands, 2004, pp. 554–595.

[82] K. Capelle. "A bird's-eye view of density-functional theory". *Brazilian journal of physics* 36.4A (2006), pp. 1318–1343.

[83] W. Kohn and L. J. Sham. "Self-consistent equations including exchange and correlation effects". *Physical Review* 140.4A (1965), A1133.

[84] A. D. Becke. "A new mixing of Hartree–Fock and local density-functional theories". *Journal of Chemical Physics* 98.2 (1993), pp. 1372–1377.

[85] A. D. Becke. "Density-functional thermochemistry. III. The role of exact exchange". *Journal of Chemical Physics* 98.7 (1993), pp. 5648–5652.

[86] A. P. Scott and L. Radom. "Harmonic vibrational frequencies: an evaluation of Hartree-Fock, Møller-Plesset, quadratic configuration interaction, density functional theory, and semiempirical scale factors". *Journal of Physical Chemistry* 100.41 (1996), pp. 16502–16513.

[87] J. P. Perdew and M. Levy. "Extrema of the density functional for the energy: Excited states from the ground-state theory". *Physical Review B* 31.10 (1985), p. 6264.

[88] M. Frisch et al. *Gaussian 16*. 2016.

[89] K. A. Peterson et al. "Systematically convergent basis sets with relativistic pseudopotentials. II. Small-core pseudopotentials and correlation consistent basis sets for the post-d group 16-18 elements". *Journal of Chemical Physics* 119 (2003), pp. 11113–11123. DOI: 10.1063/1.1622924.

[90] F. Weigend and R. Ahlrichs. "Balanced basis sets of split valence, triple zeta valence and quadruple zeta valence quality for H to Rn: Design and assessment of accuracy". *Physical Chemistry Chemical Physics* 7 (2005), p. 3297. DOI: 10.1039/b508541a.

[91] D. Rappoport and F. Furche. "Property-optimized Gaussian basis sets for molecular response calculations". *Journal of Chemical Physics* 133 (2010), p. 134105. DOI: 10.1063/1.3484283.

[92] S. Zhu et al. "Molecular dynamics simulation of microscopic structure and hydrogen bond network of the pristine and phosphoric acid doped polybenzimidazole". *Polymer* 52.3 (2011), pp. 881–892.

[93] M. J. Frisch and et al. *Gaussian 09, Revision D*. Wallingford, CT: Gaussian, Inc, 2009.

[94] C. M. Breneman and K. B. Wiberg. "Determining atom-centered monopoles from molecular electrostatic potentials. The need for high sampling density in formamide conformational analysis". *Journal of Computational Chemistry* 11.3 (1990), pp. 361–373.

[95] R. Dennington, T. Keith, J. Millam, et al. "GaussView, version 5" (2009).

[96] M. D. Hanwell et al. "Avogadro: An advanced semantic chemical editor, visualization, and analysis platform." *Journal of Cheminformatics* 4.1 (2012), p. 17.

[97] A. Jurcik et al. "CAVER Analyst 2.0: analysis and visualization of channels and tunnels in protein structures and molecular dynamics trajectories". *Bioinformatics* 34.20 (2018), pp. 3586–3588.

[98] Y. Marcus. "The standard partial molar volumes of ions in solution. Part 4. Ionic volumes in water at 0-100 C". *The Journal of Physical Chemistry B* 113.30 (2009), pp. 10285–10291.

[99] T. Giorgino. "Computing diffusion coefficients in macromolecular simulations: the Diffusion Coefficient Tool for VMD". *Journal of Open Source Software* 4.41 (2019), p. 1698.

[100] N. Ziv and D. R. Dekel. "A practical method for measuring the true hydroxide conductivity of anion exchange membranes". *Electrochemical Communications* 88 (2018), pp. 109–113.

[101] D. Novitski et al. "Electrochemical reduction of dissolved oxygen in alkaline, solid polymer electrolyte films". *Journal of the American Chemical Society* 138.47 (2016), pp. 15465–15472.

[102] R. Bock et al. "Measuring the thermal conductivity of membrane and porous transport layer in proton and anion exchange membrane water electrolyzers for temperature distribution modeling". *International Journal of Hydrogen Energy* 45 (2019), pp. 1236–1254.

[103] B. Shanahan et al. "30 μm thin hexamethyl-p-terphenyl poly (benzimidazolium) anion exchange membrane for vanadium redox flow batteries". *Electrochemical Communications* 102 (2019), pp. 37–40.

[104] Y. Li, D. G. Peiffer, and B. Chu. "Long-range inhomogeneities in sulfonated polystyrene ionomers". *Macromolecules* 26.15 (1993), pp. 4006–4012.

[105] W. Germer et al. "Phase Separated Methylated Polybenzimidazole (O-PBI) Based Anion Exchange Membranes". *Macromolecular Materials and Engineering* 300.5 (2015), pp. 497–509.

[106] G. N. Clark et al. "Small-angle scattering and the structure of ambient liquid water". *Proceedings of the National Academy of Sciences* 107.32 (2010), pp. 14003–14007.

[107] H. Liu and S. J. Paddison. "Direct comparison of atomistic molecular dynamics simulations and X-ray scattering of polymerized ionic liquids". *ACS Macro Letters* 5.4 (2016), pp. 537–543.

[108] A. A. Wight. *Small-Angle X-Ray Characterization of an Anion-Exchange Membrane*. Tech. rep. Co-Op Report. Simon Fraser University, 2020.

[109] Y. Marcus. "The standard partial molar volumes of ions in solution. Part 4. Ionic volumes in water at 0- 100 C". *The Journal of Physical Chemistry B* 113.30 (2009), pp. 10285–10291.

[110] D. R. Lide, ed. *CRC Handbook of Chemistry and Physics*. 83rd ed. CRC Press, 2005.

[111] D. M. Tartakovsky and M. Dentz. "Diffusion in porous media: phenomena and mechanisms". *Transport in Porous Media* 130.1 (2019), pp. 105–127.

[112] P. Adler. *Porous Media: Geometry and Transports*. Butterworth-Heinemann series in chemical engineering. Butterworth-Heinemann, 1992.

[113] D.-W. Chung et al. "Validity of the Bruggeman relation for porous electrodes". *Modelling and Simulation in Materials Science and Engineering* 21.7 (2013), p. 074009.

[114] J. E. B. Randles. "Kinetics of rapid electrode reactions". *Discussions of the faraday society* 1 (1947), pp. 11–19.

[115] B. L. Henke, E. M. Gullikson, and J. C. Davis. "X-ray interactions: photoabsorption, scattering, transmission, and reflection at E=50-30,000 eV, Z=1-92". *Atomic Data and Nuclear Data Tables* 54.2 (1993), pp. 181–342.

[116] F. Gabel et al. “Medical contrast media as possible tools for SAXS contrast variation”. *International Union of Crystallography Journal* 6.4 (2019), pp. 521–525.

[117] R. M. Fernandez et al. “Influence of salt on the structure of DMPG studied by SAXS and optical microscopy”. *Biochimica et Biophysica Acta (BBA)-Biomembranes* 1778.4 (2008), pp. 907–916.

[118] Y. S. Kim and B. S. Pivovar. “Moving beyond mass-based parameters for conductivity analysis of sulfonated polymers”. *Annual review of chemical and biomolecular engineering* 1 (2010), pp. 123–148.

[119] I. S. Joung and T. E. Cheatham III. “Molecular dynamics simulations of the dynamic and energetic properties of alkali and halide ions using water-model-specific ion parameters”. *The Journal of Physical Chemistry B* 113.40 (2009), pp. 13279–13290.

[120] K. P. Jensen and W. L. Jorgensen. “Halide, ammonium, and alkali metal ion parameters for modeling aqueous solutions”. *Journal of Chemical Theory and Computation* 2.6 (2006), pp. 1499–1509.

Appendix A

Raw SAXS Data Examples

A.1 Background scattering from the XenHumGen environment chamber

Raw X-ray scattering data from a measurement of 85% df HMT-PMBI(Cl) at controlled humidity, before background sub-traction or splicing of the data from different detector positions, as well as a background measurement, is shown in Fig. A.1. Scattering from the empty XenHumGen sample chamber is shown in Fig. S1d. The scattering is dominated by the two Kapton windows of the environment control chamber.

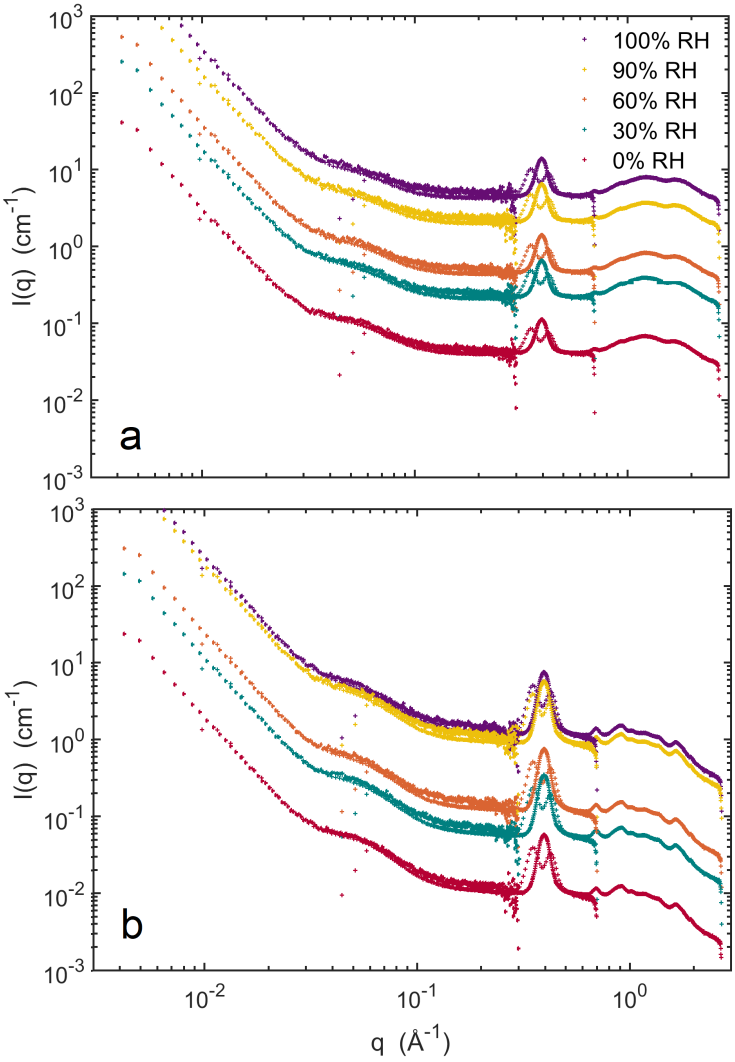

Figure A.1: Azimuthally-averaged raw X-ray scattering measurements of (a) 85% df HMT−PMBI(Cl−), and (b) the empty XenHumGen sample holder at controlled humidity. This is the raw data used to produce Fig. 4.1a.

A.2 Crystalline speckles from the mica windows

Raw 2D X-ray scattering data from the measurement of soaked DMP−PMPI−MM(Cl−) is shown in Fig. A.2. It was necessary to manually mask out bright speckles scattered from crystalline domains of the mica windows of the sample holder before azimuthal averaging.

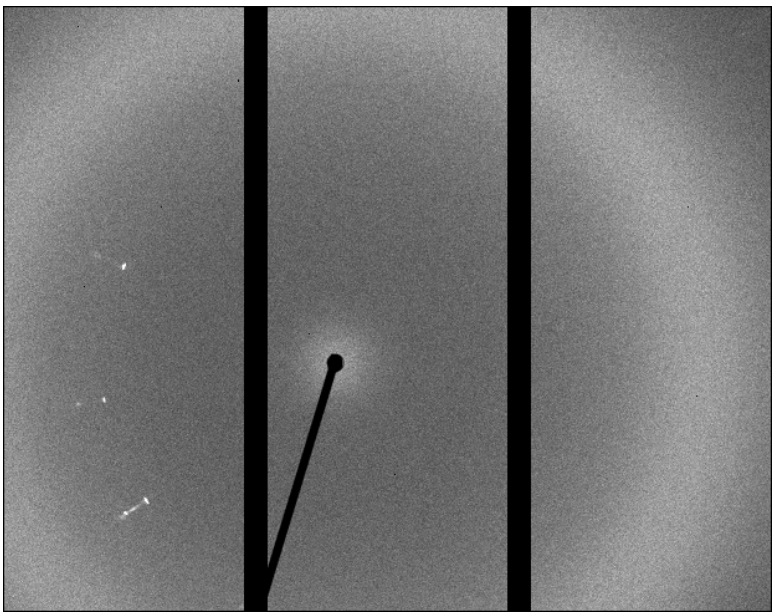

Figure A.2: Raw 2D X-ray scattering data from the measurement of soaked DMP−PMPI−MM(Cl−). The bright speckles in the left segment are produced by reflections from crystalline domains of the mica paste cell windows. This is the raw data used to produce Fig. 5.6a.

Appendix B

Simulation Parameters

This appendix contains the force field used to perform the molecular dynamics simulations.

B.1 Parameters

The molecular dynamics parameters used in the simulation are shown in Tables 1-4. Atom types CAi and C!m were added to allow the definition of custom dihedral energy profiles.

Table B.1: Van der Waals parameters for $E_{\text{non-bonded}}$

Atom	Description	ϵ	σ	Source
NS	Substituted nitrogen	0.170	3.25	Jorgensen[67]
NB	Basic nitrogen	0.170	3.25	Jorgensen[67]
CA	Aromatic carbon	0.070	3.55	Jorgensen[67]
CAi	Aromatic carbon in benzimidazole fusion	0.08	3.50	LigParGen[66]
C!	Aromatic carbon w/ inter-ring bond	0.070	3.55	Jorgensen[67]
C!m	Aromatic carbon in mesitylene w/ inter-ring bond	0.070	3.55	Jorgensen[67]
CT	Methyl carbon	0.066	3.5	Jorgensen[67]
HC	Methyl hydrogen	0.030	2.50	Jorgensen[67]
HA	Aromatic hydrogen	0.066	2.42	Jorgensen[67]
CT	Methyl carbon	0.066	3.5	Jorgensen[67]
I	Iodide	0.71	4.81	Jensen[120]
Br	Bromide	0.71	4.28	Jensen[120]
Cl	Chloride	0.71	4.02	Jensen[120]
F	Fluoride	0.71	3.05	Jensen[120]
OH	Water and hydroxide O	0.1852	3.1589	TIP4P[77]
HO	Water and hydroxide H	0.0000	0.0000	TIP4P[77]

Table B.2: Bond parameters for E_{bonds}

Atom 1	Atom 2	Description	K_r	r_0	Source
CAi	CAi	Benzimidazole fusion	520	1.37	LigParGen[66]
CA	CA	Aromatic carbon bond	469	1.40	Sambasivarao [68]
CA	CT	Methyl-aromatic carbon bond	317	1.51	LigParGen[66]
CT	NS	Methyl-aromatic nitrogen bond	337	1.475	Sambasivarao[68]
C!	NS	Aromatic bond to substituted nitrogen	477	1.343	Sambasivarao[68]
CAi	NS	Aromatic bond to substituted nitrogen (fusion)	436	1.374	LigParGen[66]
C!	NB	Aromatic bond to basic nitrogen	488	1.335	LigParGen[66]
CAi	NB	Aromatic bond to basic nitrogen (fusion)	410	1.394	LigParGen[66]
C!, C!m	C!, C!m	Inter-ring bond	385	1.460	Sambasivarao[68]
CA	HA	Aromatic hydrogen bond	367	1.08	Sambasivarao[68]
CT	HC	Methyl hydrogen bond	340	1.09	Sambasivarao[68]

Table B.3: Angle parameters for E_{angles}

Atom 1	Atom 2	Atom 3	Description	K_θ	θ_0	Source
CA , C!, C!m, CAi	CA	CA, C!, C!m, CAi	Intra-aromatic carbon angle	63	120	Sambasivarao[68]
CAi	CAi	CA	Benzimidazole fusion carbon angle	85	109.8	LigParGen[66]
CAi	NS, NB	C!	Imidazole internal angle	70	109.8	Sambasivarao[68]
CT	CA	CA, C!m	Methyl-mesitylene angle	70	120	LigParGen[66]
CT	NS	C!	Methyl-nitrogen-C2 angle	63	112.4	LigParGen[66]
CT	NS	CAi	Methyl-nitrogen-imidazole angle	70	125.8	LigParGen[66]
CT	NS	C!	Methyl-nitrogen-C2 angle	63	112.4	LigParGen[66]
NB, NS	C!	NB, NS	Nitrogen-carbon-nitrogen angle	70	120	Sambasivarao[68]
NB, NS	C!	C!m	Inter-ring nitrogen-carbon-carbon angle	70	130	LigParGen[66]
NS, NB	CAi	CA	Benzimidazole fusion "external" angle	70	108.7	LigParGen[66]
NS, NB	CAi	CAi	Benzimidazole fusion "internal" angle	70	106.2	LigParGen[66]
C!	NB, NS	C!	Imidazole C-N-C angle	70	109.8	LigParGen[66]
C!	CAi	NB, NS	Imidazole C-C-N angle	70	121.6	LigParGen[66]
HA	CA	CA, CAi, C!	Aromatic hydrogen angle	35	120	Sambasivarao[68]
HC	CT	NS, CA	Hydrogen-carbon-aromatic angle	35	109.5	Sambasivarao[68]
HC	CT	HC	Methyl-nitrogen-C2 angle	33	107.8	Sambasivarao[68]
NS	CT	CT	nitrogen-aklyl angle	51.65	110.58	LigParGen[66]
CT	CT	CT	C-C-C aklyl angle	58.35	112.7	LigParGen[66]

Table B.4: Dihedral angle parameters for $E_{\text{dihedrals}}$

Atom 1	Atom 2	Atom 3	Atom 4	Description	$K_{1,\phi}$	$K_{2,\phi}$	$K_{3,\phi}$	$K_{4,\phi}$	Source
any	CA, CAi, NS, NB	CA, CAi, NS, NB, C!, C!m	any	Aromatic carbon dihedral	0.000	7.250	0	0	Sambasivarao[68]
any	CA	CA	any	Planar aromatic dihedral	0.000	7.000	0.000	0.000	Sambasivarao[68]
any	NS, NB	any	NS, NB	Imidazole dihedral	0.000	10.000	0.000	0.000	LigParGen[66]
HC	any	any	any	Methyl dihedral	0.000	0.000	0.000	0.000	LigParGen[66]
C!m	C!	NS, NB	any	Methyl dihedral	0.000	0.000	0.000	0.000	LigParGen[66]
CAi	CAi	C!	CA	Imidazolium-Phenyl	0.000	1.085	0.000	0.000	LigParGen[66]
CT	CT	CT	CT	Butyl	1.300	-0.200	0.200	0.000	LigParGen[66]
NS	CT	CT	CT	Nitrogen-Alkyl	1.392	0.674	0.525	0.000	LigParGen[66]
C!m, C!	NS	CT	CT	Carbon-nitrogen-alkyl	-1.000	-0.35	0.000	0.000	LigParGen[66]
NS	C!	C!m	CA	Mesitylene-Methylated benzene	0.000	5.500	0.000	0.550	Schibli[28]
NB	C!	C!m	CA	Mesitylene-unmethylated benzene	0.000	3.000	0.000	0.350	Schibli[28]
CA	C!	C!m	CA	Mesitylene-phenylene	0.000	3.300	0.000	0.600	Schibli[28]
CA	C!	C!	CA	Benzene-benzene	0.35	1.200	0.000	0.000	Schibli[28]
NS	CAi	C!	CA	Imidazolium-phenylene	0	1.280	0	0.35	This work

Table B.5: Improper dihedral terms for E_{improper}

Atom	Description	K_I	d	n	Source
CA, C!, C!m	Carbon improper	2.5	-1	2	LigParGen[66]
NS	Nitrogen improper	2.0	-1	2	LigParGen[66]

B.2 Molecular topologies and partial charges

This section contains the molecular fragment topologies and partial charges used in the simulations.

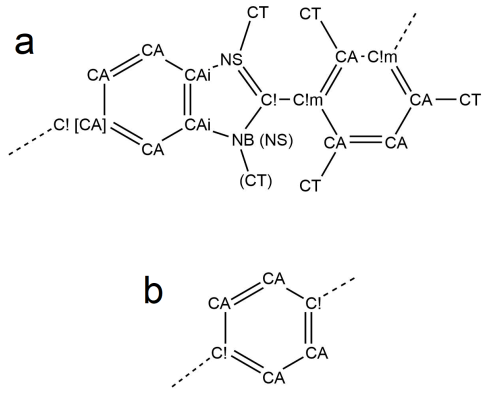

Figure B.1: Molecular topology of (a) the benzimidazole-mesytylene subunit, and (b) the phenylene subunit used in the molecular dynamics simulations of HMT–PMBI. In (a), the atoms in (brackets) are for the doubly methylated, cationic subunits, and the atoms in [brackets] are for the terminal subunits. Each CT atom is also bonded to three HC atoms, and some CA atoms are bonded to an additional HA atom as required.

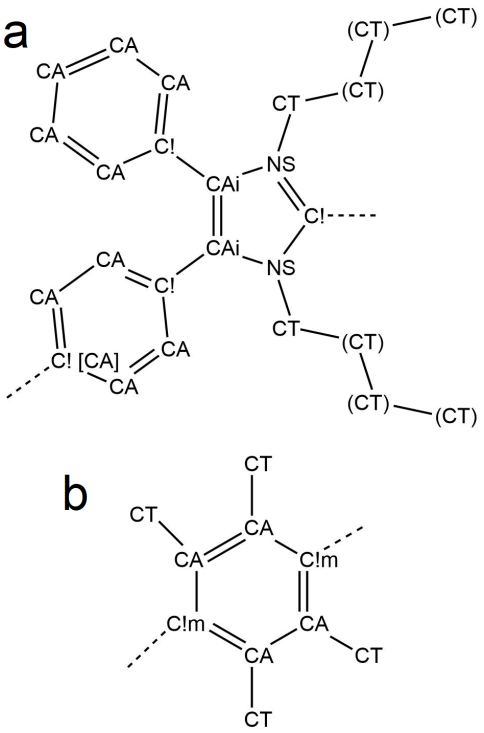

Figure B.2: Molecular topology of (a) the bis-imidazolium subunit and (b) the durene subunit used in the molecular dynamics simulations of TMP−PMPI. In (a), the atoms in (brackets) are for the butylated subunits, and the atom in [brackets] is for the terminal subunits. Each CT atom is also bonded to three HC atoms, and some CA atoms are bonded to an additional H atom as required.

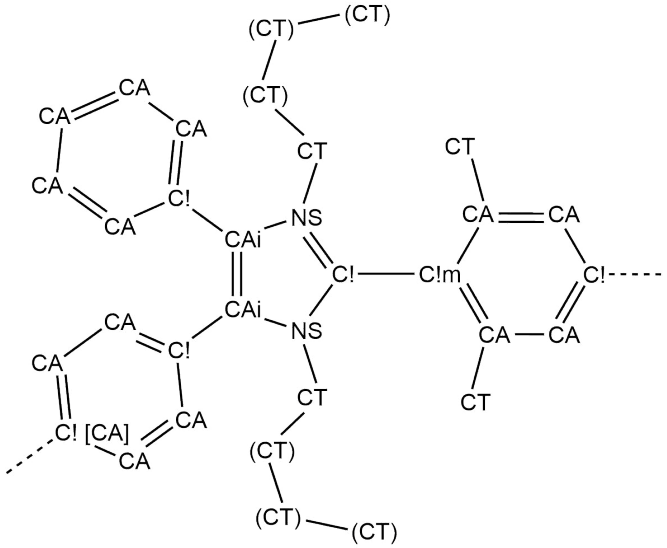

Figure B.3: Molecular topology of DMP-PMPI monomer. The atoms in (brackets) are included in the butylated monomers, and the atom in [brackets] is for the terminal subunits. Each CT atom is also bonded to three HC atoms, and some CA atoms are bonded to an additional HA atom as required.

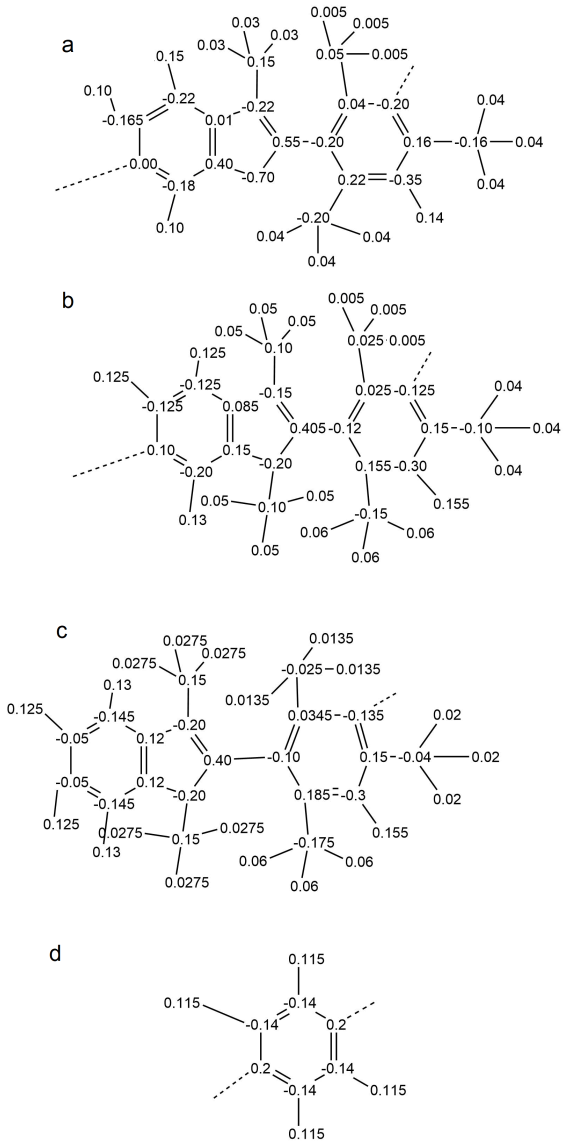

Figure B.4: The partial charges used for the (a) neutral benzimidazole-mesitylene, (b) the cation benzimidazole-mesitylene, (c) terminal benzimidazole, and (d) phenylene molecular subunits.

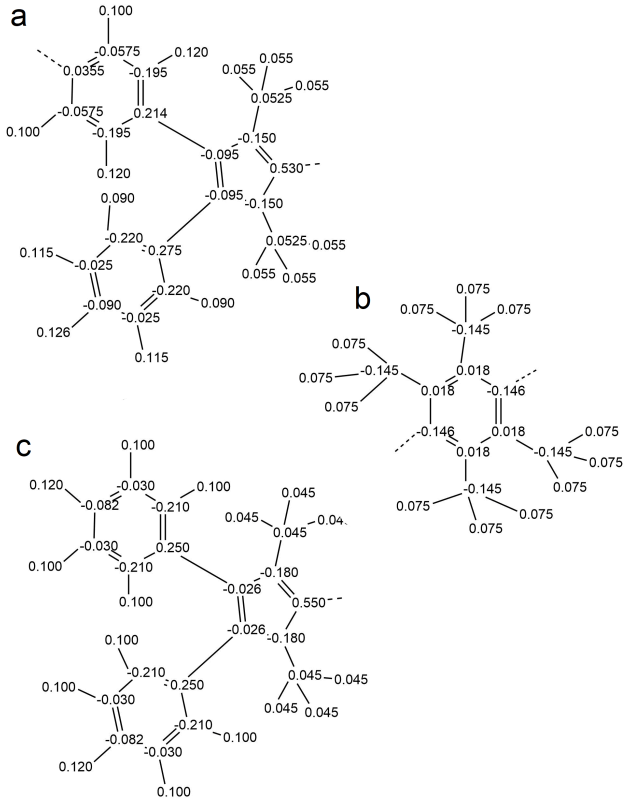

Figure B.5: The partial charges used for the (a) methylated bis-imidazolium, (b) durene, (c) terminal methylated bis-imidazolium molecular subunits.

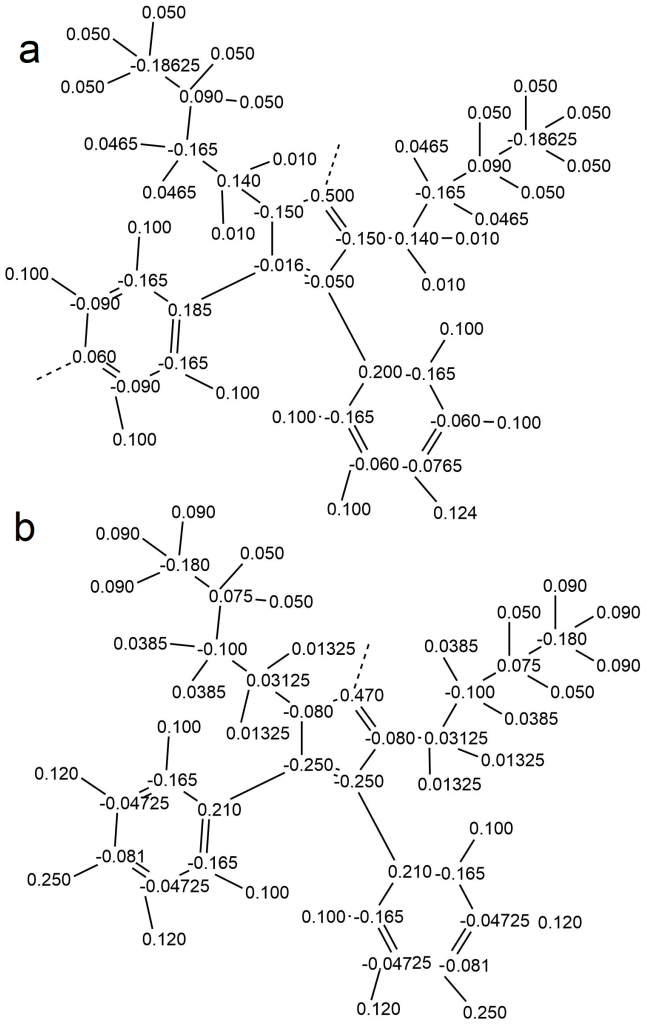

Figure B.6: The partial charges used for the (a) backbone, and (b) terminal butylated bis-imidazolium molecular subunits.

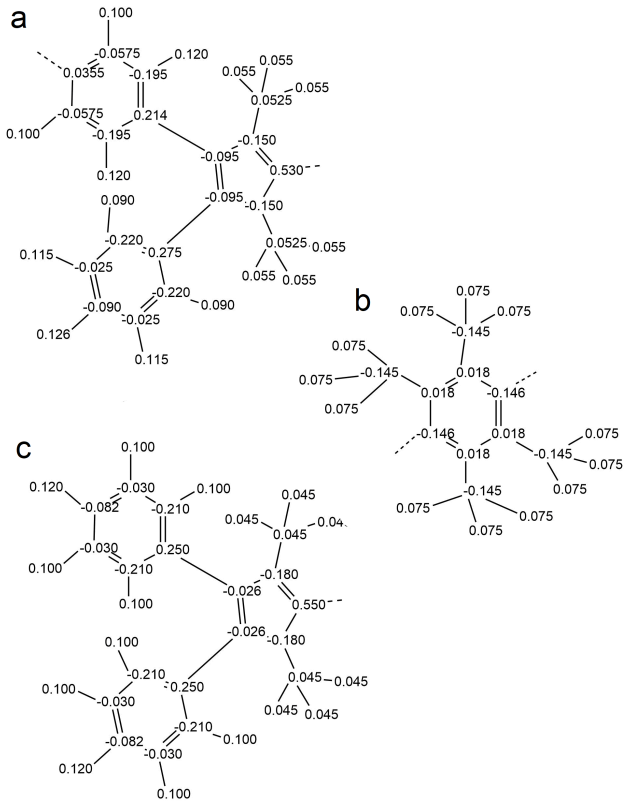

Figure B.7: The partial charges used for the (a) backbone. and (b,c) terminal DMP−PMPI−MM monomers.

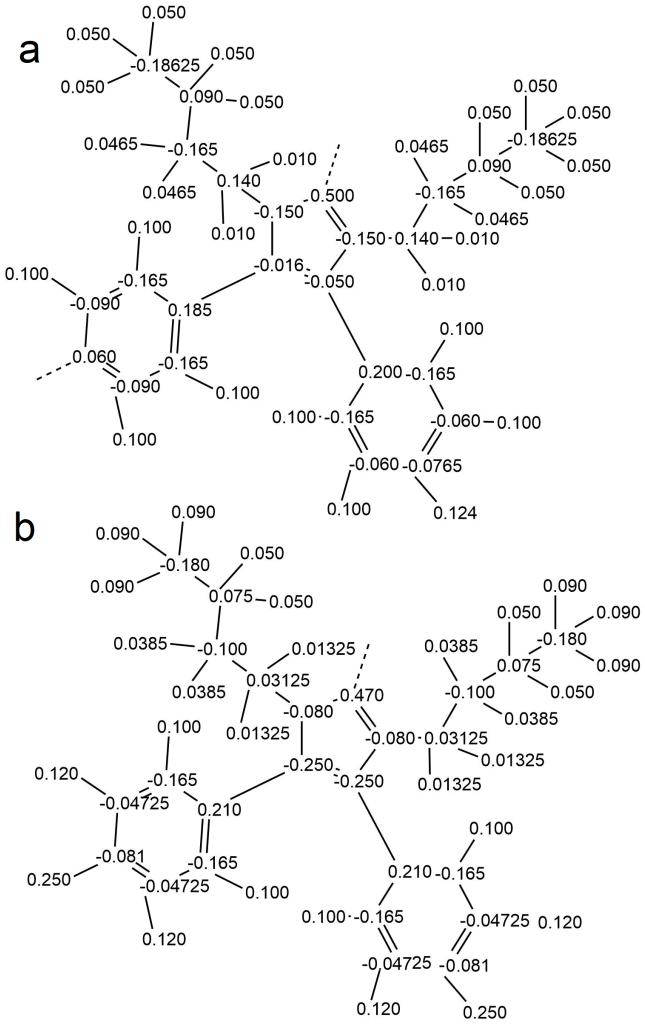

Figure B.8: The partial charges used for the (a) backbone, and (b,c) terminal DMP – PMPI – BB monomers.

B.3 Parameter optimization

This section contains potential energy curves calculated while optimizing dihedral parameters.

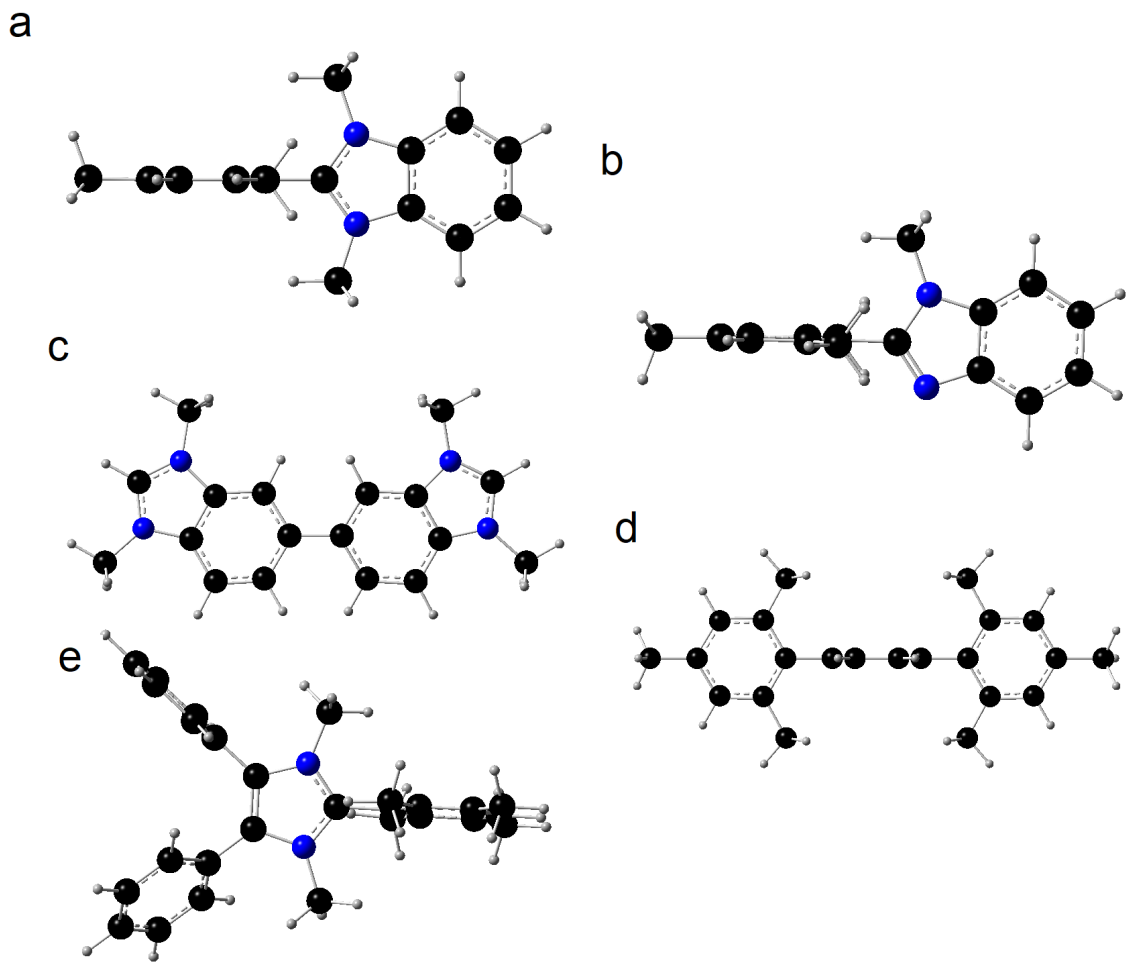

Figure B.9: Model compounds used to calculate target dihedral energy profiles for(a) mesitylene-dimethylated benzimidazole, (b) mesitylene-methylated benzimidazole, (c) benzimidazole-benzimidazole, (d) phenylene-mesitylene, and (e) imidazole-phenylene rotations.

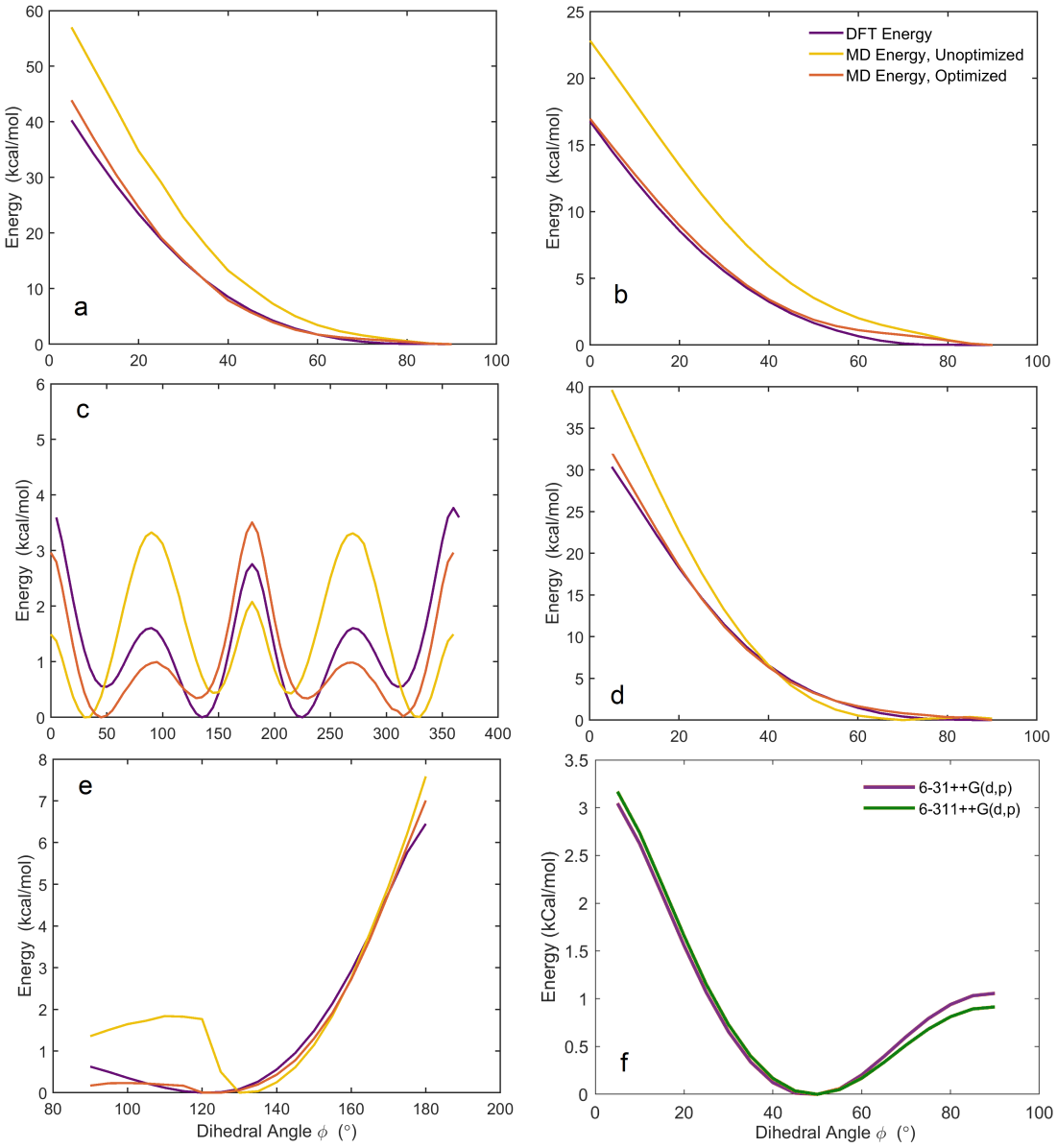

Figure B.10: Target (purple), original (yellow), and optimized (orange) dihedral energy profiles for the model compounds shown in Fig. B.9: (a) mesitylene-dimethylated benzimidazole, (b) mesitylene-methylated benzimidazole, (c) benzimidazole-benzimidazole, (d) phenylene-mesitylene, and (e) imidazole-phenylene rotations, and (f) comparison between target energy profiles for benzimidazolium-benzimidazolium dihedral rotations calculated at the B3LYP/6-31++G(d,p) and 6-311++G(d,p) levels of theory. Note that the energy scales of each plot differ significantly. Plots (a-d) were originally reported in Reference [28] and are reproduced with permission of the publisher.

Appendix C

Supplemental MD Results

Snapshots of the water/anion phases taken from simulations of TMP–PMPI–MM(Cl–) and DMP–PMPI–MM(Cl–) at $\lambda = 12$ and $\lambda = 16$ are shown in Fig. C.1.

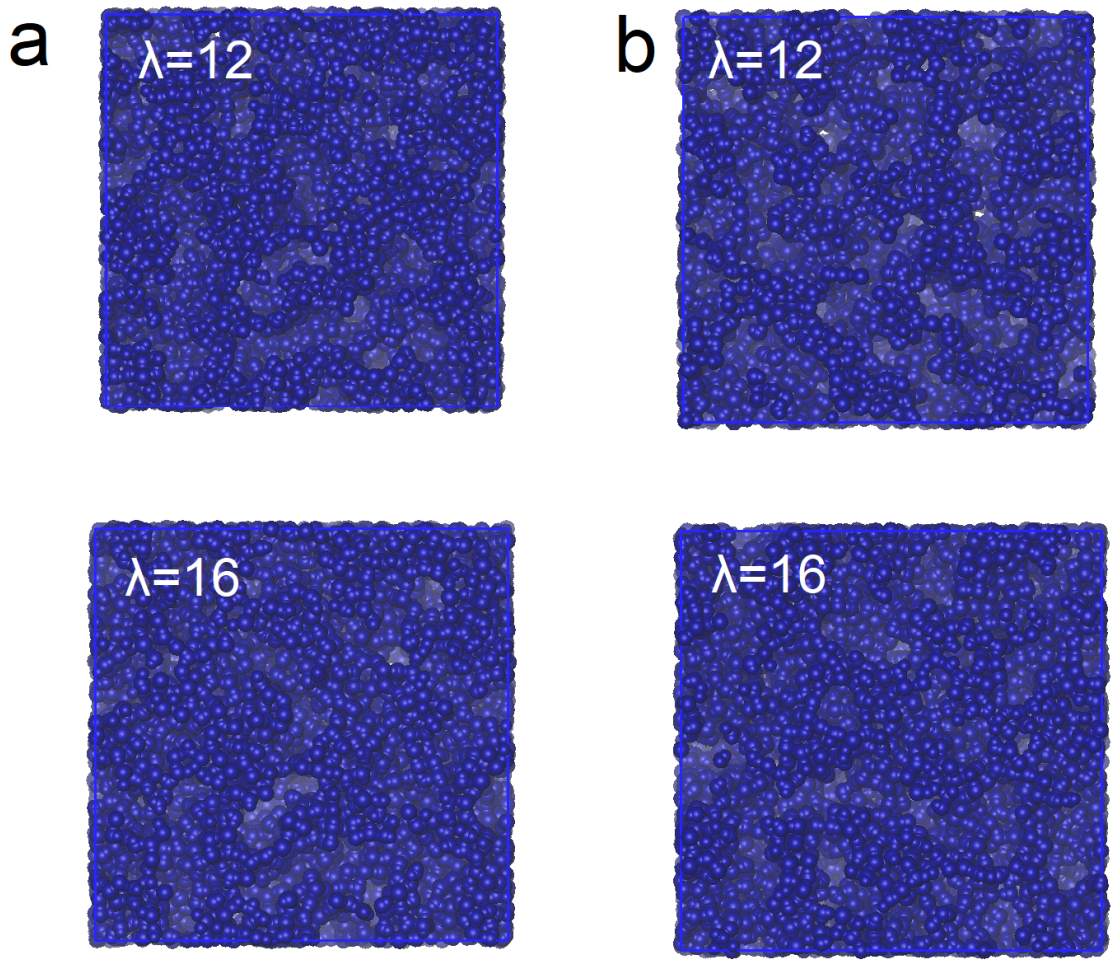

Figure C.1: Snapshots of the water/anion domains of (a) TMP−PMPI−MM(Cl−), and (b) DMP−PMPI−MM(Cl−) simulations at $\lambda = 12$ and 16. The images are to scale and reflect the relative size of each system. In each system, every water and anion is part of the percolating network.

C.1 Structure factors at various hydrations

Total scattering and partial structure factors taken from simulations of TMP–PMPI–MM(Cl–) and DMP–PMPI–MM(Cl–) at $\lambda = 12$ and $\lambda = 16$ are shown in Fig. C.1.

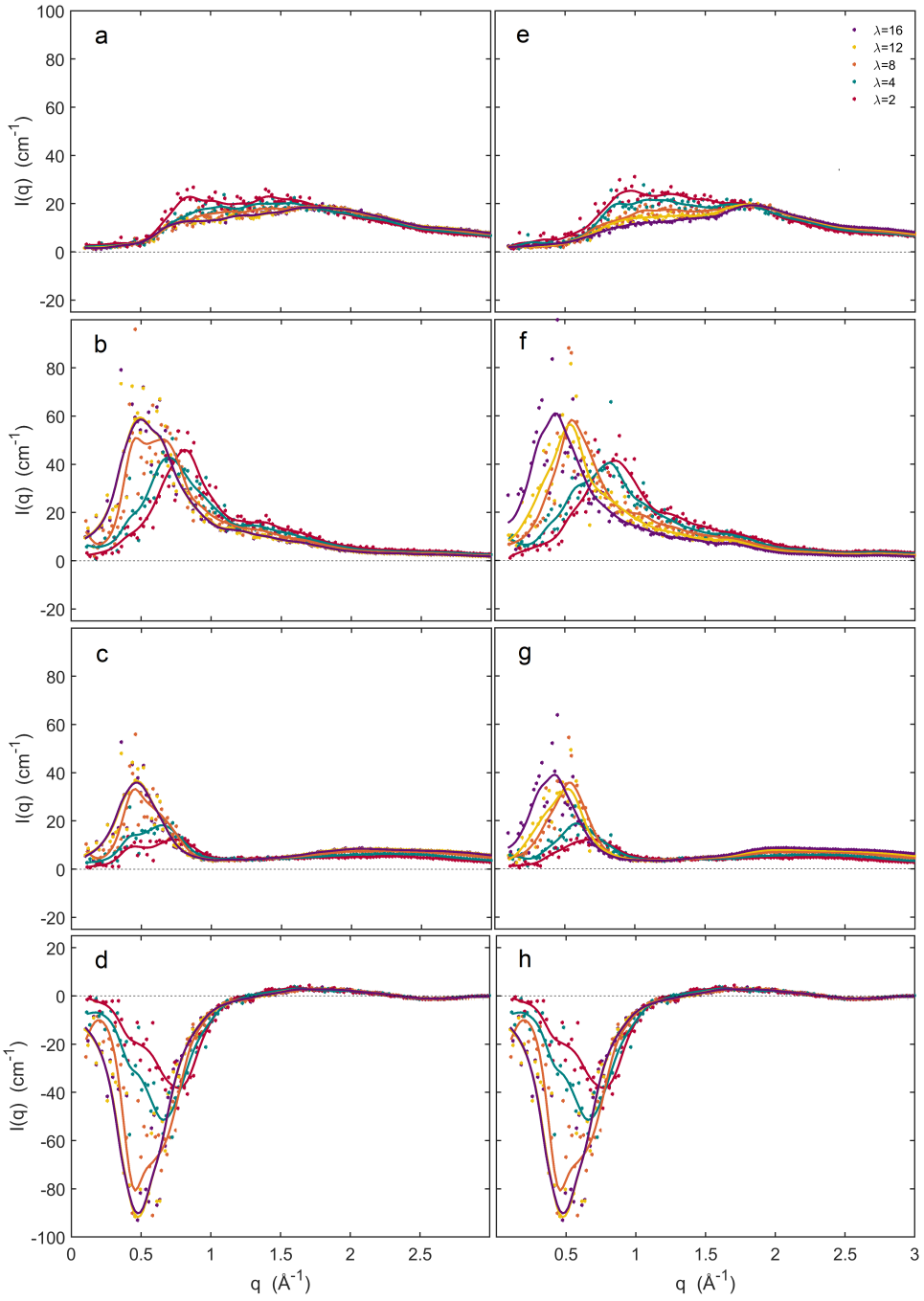

Figure C.2: Structure factors calculated from simulations of (a-d) TMP–PMPI–PMBI–MM(Cl–) and (e-h) DMP–PMPI–PMBI–MM(Cl–), at various levels of hydration, considering (a,e) total scattering, (b,f) structure within the polymer phase, (c,g) structure within the water/anion phase, and (d,h) polymer-water/anion structure. The solid curves are multispline fits without physical meaning and are intended only as guides to the eyes.

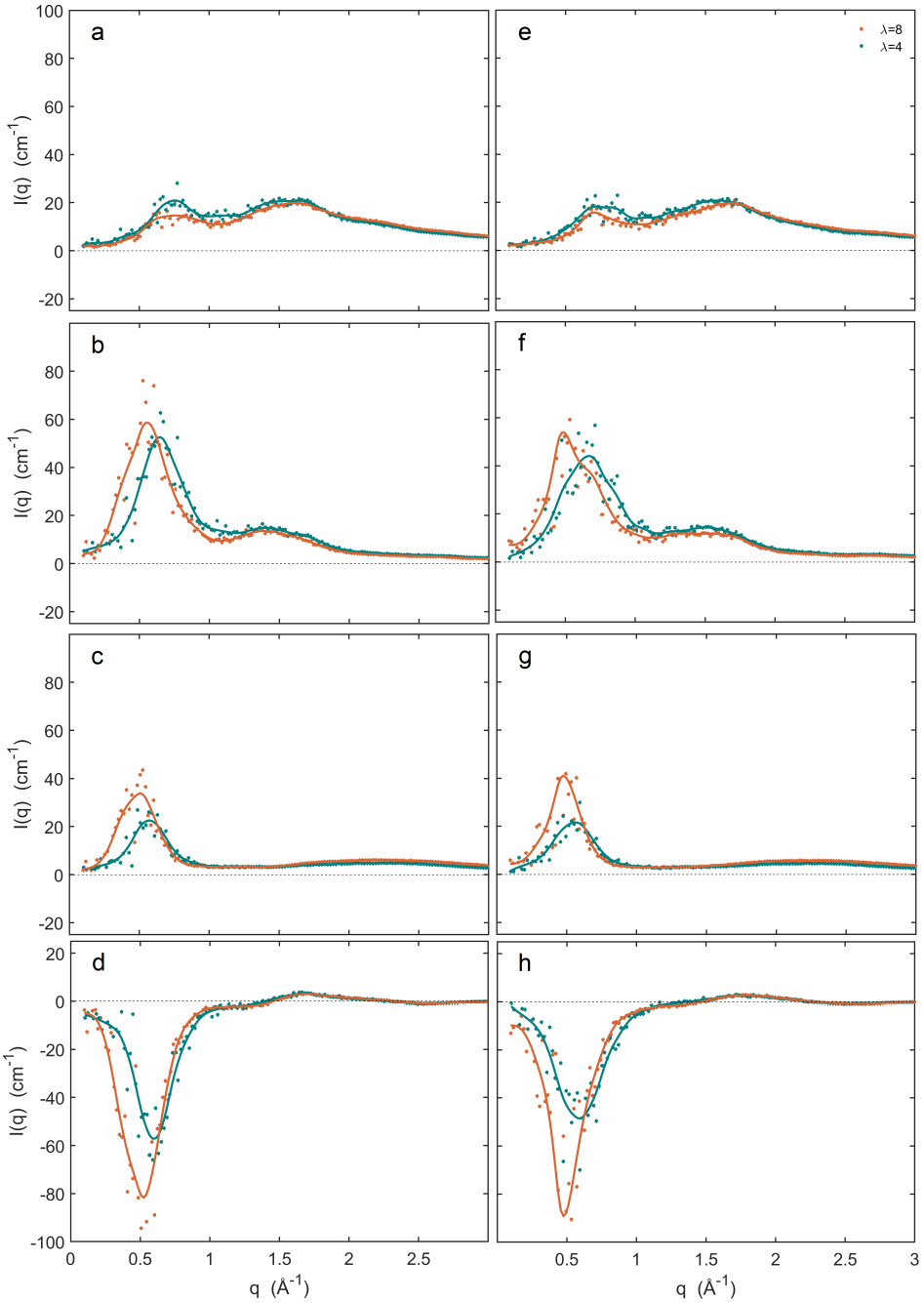

Figure C.3: Structure factors calculated from simulations of (a-d) TMP–PMPI–PMBI–BB(Cl–) and (e-h) DMP–PMPI–PMBI–BB(Cl–), at various levels of hydration, considering (a,e) total scattering, (b,f) structure within the polymer phase, (c,g) structure within the water/anion phase, and (d,h) polymer-water/anion structure. The solid curves are multispline fits without physical meaning and are intended only as guides to the eyes.